TECH LIBRARY KAFB, NM
0060654

NASA CONTRACTOR REPORT

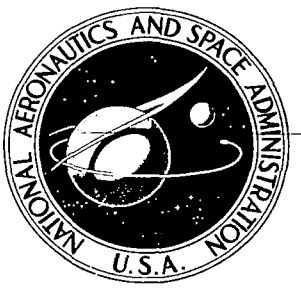

NASA CR-1462
c. 1

NASA CR-1462

LOAN COPY: RETURN TO
AFWL (WLOL)
KIRTLAND AFB, N MEX

STAGNATION POINT HEAT TRANSFER DURING HYPERVELOCITY ATMOSPHERIC ENTRY

by W. S. Rigdon, R. B. Dirling, Jr., and M. Thomas

Prepared by
McDONNELL DOUGLAS CORPORATION
Santa Monica, Calif.
for Langley Research Center

NATIONAL AERONAUTICS AND SPACE ADMINISTRATION • WASHINGTON, D. C. • FEBRUARY 1970

NASA CR-1462
TECH LIBRARY KAFB, NM
0060654

STAGNATION POINT HEAT TRANSFER DURING HYPERVELOCITY ATMOSPHERIC ENTRY

By W. S. Rigdon, R. B. Dirling, Jr., and M. Thomas

Distribution of this report is provided in the interest of information exchange. Responsibility for the contents resides in the author or organization that prepared it.

Issued by Originator as Report No. DAC-63243

Prepared under Contract No. NAS 1-7757 by
McDONNELL DOUGLAS ASTRONAUTICS COMPANY - WESTERN DIVISION
Santa Monica, Calif.

for Langley Research Center

NATIONAL AERONAUTICS AND SPACE ADMINISTRATION

For sale by the Clearinghouse for Federal Scientific and Technical Information
Springfield, Virginia 22151 – Price $3.00

SUMMARY

Stagnation point heat transfer solutions have been generated for selected conditions of altitude, velocity, nose radius, and mass injection at the wall. For these solutions the radiative transfer has been computed considering the detailed spectral radiative properties of both air and ablation products including atomic line transitions. The effects of the thermodynamic and transport properties of ablation products on the heat flux at the wall have been investigated, and radiative preheating of the ambient air has been considered. The results have shown that ablation products are less effective in reducing the radiative flux to the wall than previously predicted. The investigation of an approximate semi-local formulation for the net radiant emission has revealed the unsuitability of this technique for analyzing high temperature shock layers. Comparison of the detailed solutions with other less exact methods, e.g., line grouping, for calculating the radiative transfer in ablating body shock layers has shown the necessity for retaining full spectral detail in the description of the radiative properties.

NOMENCLATURE

A'	$(2\pi\, m/h^2)^{3/2}$
a'	$16\pi^2\, e^6/(3ch\sqrt{3})$
Bu	Reference optical depth (Bouguer number)
B^o_ω	Spectral intensity of black body
b	Line half-width
C_A	Mass fraction of ablator
c_p	Specific heat
c	Speed of light
$\mathscr{D}_{12}$	Binary diffusion coefficient for "ablator" diffusing into "air"
$\mathscr{D}_{A-B}$	Binary diffusion coefficient for species A diffusing into species B
E	Energy level
E_m	Ionization potential for m-ion
E_R	Rydberg energy
F	Radiative flux
f_e	Electronic oscillator strength
g_o	Ground state degeneracy
g	Degeneracy
h	Planck constant; static enthalpy; or altitude
I	Intensity of radiation
K	Total thermal conductivity
k	Boltzmann constant
k_ω	Linear spectral absorption coefficient

k_ω^{ref}	Table input for k_ω at $N = 10^{17}$ cm^{-3}.
$\bar{k}_c$	Continuum mean absorption coefficient
$\bar{k}_P$	Planck mean absorption coefficient
m	Electron mass; also degree of ionization
$\bar{m}$	Mean degree of ionization in gas mixture
$\dot{m}$	Blowing rate, $(\rho v)_w/(\rho v)_\infty$
N	Species concentration, number density
n	Principal quantum number of active electrons
p	Pressure
q^C	Convective heat flux
q^R	Radiative heat flux
$q_{v''v'}$	Franck-Condon factor
R_N	Nose radius
r	Radial distance from axis of symmetry
s	Line of sight path length
T	Temperature
u	Velocity parallel to body
V_∞	Free-stream velocity
v	Velocity normal to body
x	Distance parallel to body
y	Distance normal to body
y^*	Value of y where $\rho v = 0$
β_e', β_e''	Rotational constants for upper and lower electronic states, respectively
$\Delta\beta$	Absolute value of $\beta_e' - \beta_e''$
δ	Shock layer thickness
δ_o	Adiabatic shock layer thickness

θ	Angle between y unit vector and line of sight path
μ	Viscosity
ρ	Density
σ	Stefan-Boltzmann constant
τ	Optical depth
υ', υ''	Vibrational quantum number for upper and lower electronic states, respectively
ω	Wave number
ω_c	Wave number of line center
ω_e''	Vibrational fundamental frequency for lower electronic state
ω_o	Center of photodissociation band; also critical wave number (lines)
ω_o'	Critical wave number (continuum)
$\Delta\omega$	Approximate half-width of photodissociation band, chosen from empirical fit to data

Subscripts

c	Critical value; or Continuum
L	Line
o	Total
P	Planck
s	Value immediately downstream of shock
w	Wall
ω	Spectral
∞	Free stream

Superscripts

+	In positive y-direction; toward shock
-	In negative y-direction; toward wall
o	Black body

STAGNATION POINT HEAT TRANSFER DURING HYPERVELOCITY ATMOSPHERIC ENTRY

By W. S. Rigdon, R. B. Dirling, Jr., and M. Thomas
McDonnell Douglas Astronautics Company--Western Division

INTRODUCTION

Radiant energy transport through the high-temperature shock layer surrounding the stagnation point of a blunt re-entry vehicle has been the subject of intensive investigation. Analysis techniques for predicting the radiative and convective heat transfer rates experienced by a vehicle entering a planetary atmosphere have progressed from simple computations in which the flow field and radiant energy transport were uncoupled (Reference 1) to complex coupled solutions where an attempt is made to account for all radiative transport phenomena (References 2 and 3). In addition, because the full radiative gas dynamic problem is described by complex integro-differential equations, many approximate techniques (References 4, 5, 6, and 7) have been developed. In general, the accuracy of the various solutions is unknown because no flight experiments have been made above 36, 000 fps (NASA Project FIRE) where coupling is rather weak. While shock tube measurements can verify theoretical models for the gross spectral emittance of atmospheric gases, measurements of heat transfer rates have been limited to models of small physical size for which the total optical thickness is much smaller than one except at strong line centers. In lieu of applicable experimental data for the regime of interest, "exact" calculations of radiant energy transport are desirable.

The present study is an extension of a previous analysis (Reference 2) which considered the effect of air blowing on radiative and convective heat transfer rates retaining complete spectral detail of the radiant energy transport. The restriction of no foreign species is removed and injection of carbon phenolic ablation products is considered. Energy transport by atomic lines is included. Each line is treated individually, therefore, no ambiguities due to varying elemental mass fractions are encountered as is the case when the line grouping technique is used (Reference 3). The effect of absorption of forward traveling radiation by the free-stream air ahead of the shock layer is also considered.

VISCOUS, HEAT CONDUCTING, RADIATING FLOW FIELDS

For steady-state, axisymmetric flow the thin shock layer conservation equations are

Continuity

$$\frac{\partial(\rho r u)}{\partial x} + \frac{\partial(\rho r v)}{\partial y} = 0 \tag{1}$$

Momentum

$$\rho u \frac{\partial u}{\partial x} + \rho v \frac{\partial u}{\partial y} = - \frac{\partial p}{\partial x} + \frac{1}{r} \frac{\partial}{\partial y} \left(r \mu \frac{\partial u}{\partial y} \right) \tag{2}$$

$$\frac{\partial p}{\partial y} = 0 \tag{3}$$

Energy

$$\rho v c_p \frac{\partial T}{\partial y} = u \frac{\partial p}{\partial x} + \mu \left(\frac{\partial u}{\partial y} \right)^2 + \frac{1}{r} \frac{\partial}{\partial y} \left(r K \frac{\partial T}{\partial y} \right) - \nabla \cdot \vec{F} \tag{4}$$

Stagnation Point Limit

For problems involving radiative transfer, for which integrals over distance must be evaluated, it is desirable to retain the physical length coordinates in the basic equations rather than apply similarity-type transformations. Fortunately, at the stagnation point, the conservation equations can be reduced to ordinary differential equations without resorting to such coordinate transformations. Near the stagnation streamline, i.e., for $x/R_N << 1$, the principal flow variables may be expanded in power series as follows:

$$\rho = \tilde{\rho}(y) + \rho_1(y) x^2 + \ldots .$$

$$u = \tilde{u}(y) x + u_1(y) x^2 + \ldots .$$

$$v = \tilde{v}(y) + v_1(y)\, x^2 + \ldots.$$

$$T = \tilde{T}(y) + T_1(y)\, x^2 + \ldots.$$

The choice of expansion follows from the symmetry or anti-symmetry in x of each variable.

Substituting the series expansions for ρ, u, and v into the continuity equation, noting that near the stagnation point $r \approx x$, yields

$$\tilde{\rho}\tilde{u} = -\frac{1}{2}\frac{\partial}{\partial y}(\tilde{\rho}\tilde{v}) + \text{higher order terms in x.}$$

In the limit of $x = 0$ the continuity equation is

$$\tilde{\rho}\tilde{u} = -\frac{1}{2}\frac{\partial}{\partial y}(\tilde{\rho}\tilde{v}) \tag{5}$$

Assuming a concentric shock and noting from Equation (3) that p is a function only of x, the pressure can be shown to be given by the relation

$$p(x) = p_\infty + \rho_\infty V_\infty^2 \left(1 - \frac{\rho_\infty}{\rho_s}\right)\left(1 - \frac{x^2}{R_N^2} + \text{higher order terms in x}\right).$$

Hence

$$-\frac{dp}{dx} = \rho_\infty V_\infty^2 \left(1 - \frac{\rho_\infty}{\rho_s}\right)\frac{2x}{R_N^2} + \text{higher order terms in x.} \tag{6}$$

Substituting Equation (6) and the expansions for ρ, u, and v into Equation (2) yields

$$\tilde{\rho}\tilde{u}^2 x + \tilde{\rho}\tilde{v}\frac{d\tilde{u}}{dy}x + \text{higher order terms in x}$$

$$= \rho_\infty V_\infty^2 \left(1 - \frac{\rho_\infty}{\rho_s}\right)\frac{2x}{R_N^2} + x\frac{d}{dy}\left(\mu\frac{d\tilde{u}}{dy}\right) + \text{higher order terms in x.}$$

Again taking the limit of x = 0, the x-momentum equation becomes

$$\tilde{\rho}\tilde{u}^2 + \tilde{\rho}\tilde{v}\frac{d\tilde{u}}{dy} = \rho_\infty V_\infty^2 \left(1 - \frac{\rho_\infty}{\rho_s}\right)\frac{2}{R_N^2} + \frac{d}{dy}\left(\mu\frac{d\tilde{u}}{dy}\right). \tag{7}$$

The energy equation is reduced in a similar manner. Finally substituting Equation (5) into Equation (7) and discarding the tilde notation for the asymptotic values of the flow variables, the stagnation point flow field equations become

Momentum and Continuity

$$\frac{d}{dy}\left[\mu\frac{d}{dy}\left(\frac{1}{\rho}\frac{d(\rho v)}{dy}\right)\right] - \rho v\frac{d}{dy}\left(\frac{1}{\rho}\frac{d(\rho v)}{dy}\right)$$

$$- \left[\rho_\infty V_\infty^2 \left(1 - \frac{\rho_\infty}{\rho_s}\right)\frac{4}{R_N^2} - \frac{\rho}{2}\left(\frac{1}{\rho}\frac{d(\rho v)}{dy}\right)^2\right] = 0 \tag{8}$$

Energy

$$\rho v c_p \frac{dT}{dy} = \frac{d}{dy}\left(K\frac{dT}{dy}\right) - (\nabla\cdot\vec{F})_y \tag{9}$$

Here $(\nabla\cdot\vec{F})_y$ is the divergence of the radiative flux normal to the body surface. The boundary conditions used in the study for the above equations are

At the wall	At the shock
$\rho v = \dot{m}\rho_\infty V_\infty$	$\rho v = -\rho_\infty V_\infty$
$\frac{1}{\rho}\frac{d(\rho v)}{dy} = 0$	$\frac{1}{\rho}\frac{d(\rho v)}{dy} = -2\frac{du_s}{dx} = -2\frac{V_\infty}{R_N}$
$T = T_w$	$T = T_s$

Preheating in Ambient Air

Absorption of radiation by the air ahead of the bow shock wave may significantly affect the radiative and convective stagnation point heat transfer rates experienced by the body. The solution for the complete three-dimensional flow field perturbations ahead of the bow shock wave caused by the absorption of

forward traveling radiation from the high-temperature shock layer is difficult, since it requires an evaluation of $\nabla\cdot\vec{F}$ for all points ahead of the shock. However, the results of a previous investigation (Reference 8) have shown that the perturbation to the tangential velocity, u (normal to the centerline) is of second order compared to the perturbation to the normal velocity, v. Also, the bulk of the absorption occurs within several shock layer thicknesses of the shock so that the one-dimensional approximation for the radiation field used in the shock layer can be retained. Under these conditions Equations (1) through (4) reduce to

$$\frac{d(\rho v)}{dy} = 0 \tag{10}$$

$$\rho v \frac{dv}{dy} = - \frac{dp}{dy} \tag{11}$$

$$\rho v c_p \frac{dT}{dy} = - \nabla\cdot\vec{F} \quad . \tag{12}$$

The molecular transport can be neglected because the local Reynolds number does not approach zero in the preheating region. The kinetic term in the energy equation

$$-v \frac{dp}{dy} = \rho v^2 \frac{dv}{dy} ,$$

has also been neglected since, as shown in Reference 8, $\Delta v/V_\infty \sim 10^{-3}$. Applying the boundary conditions very far upstream the solution for the preheating region is

$$\rho v = \text{constant} = - \rho_\infty V_\infty$$

$$- \rho_\infty V_\infty v + p = \rho_\infty V_\infty^2 + p_\infty$$

$$- \rho_\infty V_\infty h + F = - \rho_\infty V_\infty h_\infty + F_\infty \quad .$$

Examination of the momentum equation solution shows that since, for the conditions of interest here, $\rho_\infty V_\infty^2 \gg p_\infty$, large changes in p result in small changes in v. Therefore, the approximate solution for the preheating region is

$$\rho(y) = \text{constant} = \rho_\infty$$

$$h(y) - h_\infty = \frac{F(y) - F_\infty}{\rho_\infty V_\infty} .$$

The static enthalpy just ahead of the shock is

$$h(\delta^+) = h_\infty + \frac{F(\delta) - F_\infty}{\rho_\infty V_\infty} . \qquad (13)$$

The increase in static enthalpy immediately ahead of the bow shock wave affects the heat transfer rates at the wall primarily through the mechanism of increased temperature behind the shock wave. Although the shock layer pressure is also increased a small percentage, this effect was neglected in this study.

The complete solution for the shock layer flow field and heat transfer rates considering preheating is obtained by an iterative technique. First, the solution for the shock layer properties and the radiative flux emitted in the forward direction without preheating is obtained. This flux is then used to obtain the temperature profile ahead of the shock and the total radiant energy absorption, $F(\delta) - F_\infty$. Using the normal shock relations a new T_s value is then found and the entire procedure repeated. Convergence is assumed when the difference between the nominal (no preheating) T_s and the T_s computed including preheating agrees to within 20% for successive iterations. Convergence is rapid since $F(\delta)$ is relatively insensitive to small changes in T_s. It should be noted that the absorption coefficients in the preheating region are dependent on the temperature and species concentrations, therefore, an intermediate iteration must be performed to determine the temperature profile in this region. The specific heat and absorption coefficients for these iterations were evaluated assuming chemical equilibrium.

The Diffusion Equation

For the purpose of obtaining the atomic, molecular, and ionic species concentrations across the shock layer under the condition of ablation products injection at the wall, a binary diffusion model is assumed. That is, one component, ablator, is assumed to diffuse into a second component, air. This binary diffusion analysis yields the local concentrations of ablator and air. Utilizing the elemental mass fractions (for nitrogen, oxygen, carbon, and hydrogen) in the ablator and air the local elemental concentrations are obtained. These values are then used in a thermochemical equilibrium computation of the individual atomic, molecular, and ionic species concentrations together with the local thermodynamic properties.

The thin shock layer binary diffusion equation for the ablator concentration is

$$\rho u \frac{\partial C_A}{\partial x} + \rho v \frac{\partial C_A}{\partial y} = \frac{\partial}{\partial y}\left(\rho \mathscr{D}_{12} \frac{\partial C_A}{\partial y}\right).$$

Utilizing the procedure described under Stagnation Point Limit this equation may be reduced to

$$\rho v \frac{dC_A}{dy} = \frac{d}{dy}\left(\rho \mathscr{D}_{12} \frac{dC_A}{dy}\right). \tag{14}$$

For the entry conditions and injection rates considered in this study, effectively none of the air penetrates to the wall. Therefore, no analysis of air-ablator surface reactions is necessary to determine the ablator concentration gradient at the wall. For the ablation conditions analyzed the boundary conditions for the diffusion equation are

At the wall	At the shock
$C_A = 1$	$C_A = 0$

The selection of appropriate effective binary diffusion coefficients was made on the basis of the dominant atomic species present. Since the ablation materials considered, viz., carbon phenolic and graphite, are predominantly (or all) carbon, while air is predominantly nitrogen, the binary diffusion coefficients for atomic carbon--atomic nitrogen interaction were used. While this selection procedure is purely intuitive, an a posteriori analysis revealed that the choice of binary diffusion coefficient is not critical. A direct comparison of the ablator concentration profiles computed using carbon-nitrogen and hydrogen-nitrogen diffusion coefficients is shown in Figure 1. The two profiles are in relatively close agreement even though the hydrogen-nitrogen binary diffusion coefficients are approximately an order of magnitude greater than those for carbon-nitrogen. The results shown in Figure 1 also tend to support the assumption that the numerous atomic, molecular, and ionic species in the ablation products can be represented as a single species. That is, even the hydrogen atoms apparently do not diffusively separate greatly from the heavier species in the ablation products.

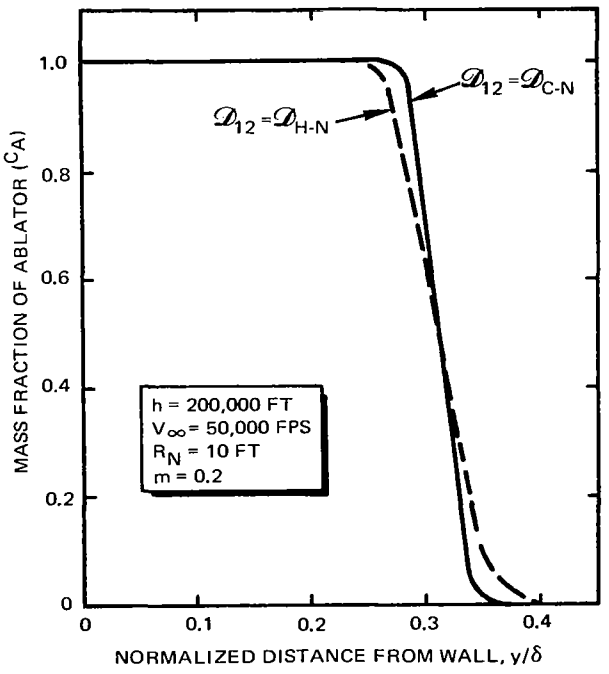

Figure 1. Comparison of Ablator Concentration Profiles Assuming Carbon-Nitrogen Diffusion and Hydrogen-Nitrogen Diffusion

Method of Solution

For the detailed spectral solutions it was discovered to be more convenient to use the flux rather than the divergence of the flux in the flow field computations. Therefore, the energy equation is written in the form

$$\rho v c_p \frac{dT}{dy} = \frac{d}{dy}\left(K\frac{dT}{dy} - F\right) \tag{15}$$

This equation together with Equation (8) can be written as a set of first-order differential equations which are solved by relatively straightforward techniques. However, a special procedure must be used for those cases which include injection at the wall. Because of numerical integration stability problems, which are discussed in Reference 2, the integration of the conservation equations must be begun at $\rho v = 0$ and proceed in both directions, i.e., toward the wall and then toward the shock. This procedure requires iteration on T, u, dT/dy, and the shear stress, all evaluated at $\rho v = 0$, until the boundary conditions on T and ρv are matched (within 1%) both at the wall and at the shock.

The detailed solution procedure is initiated by assuming a flux profile for the shock layer. A table of 30 values of flux versus tangential velocity is input to the computations and the conservation equations are solved. The temperature profile obtained is used to calculate an "output" flux profile. A new flux table is selected by averaging the input and output values and the iteration procedure continues. The criterion for final convergence used is a 2.5% difference between the input and output flux profiles. This criterion is relaxed in regions where the flux is very small or changing rapidly. In these regions the absolute difference between the two flux profiles must be less than 2.5% of the flux at the wall.

For the ablation products injection cases, the diffusion equation is solved following each solution of the energy and momentum equations. The elemental concentrations computed are used to re-evaluate the spectral absorption coefficients (and for one entry condition the thermodynamic and transport properties). It is not necessary, however, to re-evaluate the shock layer properties at each major iteration, that is, after each solution of the conservation equations. The gas mixture properties are recomputed after the first iteration, again after relatively good agreement in the flux profiles is obtained, and finally for the last iteration.

RADIANT ENERGY TRANSPORT

In the previous section the method used to solve the conservation equations for a known radiative transfer profile for the shock layer was given. In this section the corresponding procedures for determining the flux of radiation for a known temperature profile will be discussed. Also presented are the methods used to calculate the linear spectral absorption coefficients of the shock layer gases.

Linear Spectral Absorption Coefficients

The degree of rigor retained in calculations of spectral absorption coefficients of gases must be chosen so that their use will be accurate and feasible. The guiding consideration in this study was to produce absorption coefficients (k_ω) so that shock-layer radiation transfer could be accurately handled. Extremely detailed k_ω values are neither needed nor desired, as they complicate and limit the number of useful calculations that can be made during a finite time. The discussion below demonstrates the technique used; detailed descriptions of the methods used in radiative transfer and k_ω calculations are presented in full in References 9 and 10. Some discussion of the techniques is also presented in the Phase I final report for this study (Reference 2).

The basic elements of the analysis used are the following:

(1) Atomic lines are treated individually, except for grouping of multiplets and lines near photoelectric edges.

(2) Rigor retained in k_ω calculations is relaxed to a point where checks on radiative transfer in finite bands show no loss in accuracy.

(3) Chemical and thermodynamic equilibrium is assumed, and scattered radiation is not treated.

The six general types of formulations used to calculate k_ω in this study are presented in Table I. All of these techniques were used in the calculation of k_ω for air and air-ablation products gas mixtures in this study. The absorption coefficient k^*_ω is related to k_ω by

$$k_\omega = k^*_\omega \left[1 - \exp(- hc\omega/kT)\right]$$

Empirical.--For radiative transitions not treated as below, or for which little theoretical modeling is possible, absorption coefficients at some reference condition are used. These data are simply scaled with concentration and their contributions added to the sum for k_ω.

Lines, isolated.--Isolated atomic lines were treated using simple dispersion contour with electron-impact broadening (the coulombic model used by Stewart and Pyatt, Reference 11). Line strengths were obtained from tabulated data, such as Griem (Reference 12--visible lines only) or NBS (Reference 13). Where such data did not exist, or were very uncertain, such as near photoelectric edges in the far UV, the following more simplified model was used.

Lines, overlapping.--Overlapping atomic lines were treated using the same line broadening model as for isolated lines. However, the line strength was given by a hydrogen-like line model. The band model of Elsasser was used (Reference 14). This model was generally used between the last tabulated atomic line for a particular species and the photoelectric edge for ground-state ionization for that species. Thus, the far UV spectrum was filled in in a manner that treats the apparent lowering of the photoelectric edge caused by line merging.

Photoionization from the ground state.--The classical relation of Menzel and Pekeris (Reference 15) for photoionization of hydrogen was modified and used to treat ground-state ionization for all species. The effective charge on these hydrogen-like species was determined by dividing the actual ionization limit by the equivalent one for hydrogen with an electron in the same orbit (principal quantum number n--see Equation (T-8)). The degeneracy levels for the upper and lower states are taken to be equal. The Gaunt factor is taken

TABLE I

EQUATIONS USED TO CALCULATE SPECTRAL LINEAR ABSORPTION COEFFICIENTS

1. Empirical

$$k^*_\omega = k^{ref}_\omega \left(\frac{N}{10^{17}}\right) \tag{T-1}$$

2. Lines

a. Isolated

$$k^*_\omega = N_i \frac{e^2 b}{mcg_o} (g_\ell f_e) \frac{\exp(-E_\ell/kT)}{(\omega-\omega_c)^2 + b^2}, \text{ where b is} \tag{T-2}$$

$$b = \frac{2.88 \times 10^{-16} N_e n^4}{\sqrt{T}\,(m+1)^2}, \text{ and n is found from} \tag{T-3}$$

$$E_u = E_m - \frac{(m+1)^2 E_R}{n^2} \tag{T-4}$$

b. Overlapping

$$k^*_\omega = k^{P.I.}_\omega \frac{\sinh\zeta}{\cosh\zeta - \cos\alpha}, \text{where } \zeta \text{ and } \alpha \text{ are} \tag{T-5}$$

$$\zeta = N\overline{m}(0.01295)\,T^{-4}\,(m+1)^3 \left(\frac{E_m}{kT} - \frac{hc\omega}{kT}\right)^{-3.5} \tag{T-6}$$

$$\alpha \cong 2500\,(m+1)\left[T\left(\frac{E_m}{kT} - \frac{hc\omega}{kT}\right)\right]^{-1/2} \tag{T-7}$$

3. Photoionization from ground state:

$$k^*_\omega = k^{P.I.}_\omega = 2a' N_m \frac{E_m}{E_R} \frac{n^2}{(kT)^2} \left(\frac{kT}{hc\omega}\right)^3 \frac{E_m}{kT} \tag{T-8}$$

4. Photoionization from excited states and free-free

$$k^*_\omega = \frac{a'}{A'} N^2 \overline{m} h(\overline{m}) \left(\frac{kT}{hc\omega}\right)^3 (kT)^{-7/2} \exp\left(\frac{hc\omega}{kT}\right) \tag{T-9}$$

where

$$h(\overline{m}) = \begin{cases} \overline{m}^2 + 1/4 & \text{for } \overline{m} > 1/2 \\ \overline{m} & \text{for } \overline{m} \le 1/2 \end{cases}$$

5. Photodissociation

$$k^*_\omega = \frac{1}{\Delta\omega\sqrt{\pi}} \left[f(\omega_{e''})\right]^{1/2} \frac{\pi e^2}{mc^2} N_\ell f_e \exp\left[f(\omega_{e''})\left(\frac{\omega-\omega_c}{\Delta\omega}\right)^2\right] \tag{T-10}$$

where

$$f(\omega_{e''}) = \left[1 - \exp\left(\frac{-hc\omega_{e''}}{kT}\right)\right]\left[1 + \exp\left(\frac{-hc\omega_{e''}}{kT}\right)\right]^{-1} \tag{T 11}$$

6. Diatomic molecule band system

$$k^*_\omega = \frac{\pi e^2}{mc^2} N_\ell \left[1 - \exp\left(\frac{-hc\omega_{e''}}{kT}\right)\right] \exp\left(\frac{-v''hc\omega_{e''}}{kT}\right) q_{v''v'} f_e S(\omega) \tag{T-12}$$

where

$$S(\omega) = \frac{hc\beta_{e''}}{kT\Delta\beta} \exp\left[-\frac{hc\beta_{e''}}{kT\Delta\beta}(\omega - \omega_{v'v''})\right] \text{ in band.} \tag{T-13}$$

to be unity. This simple model has a much faster decline with increasing ω than more accurate calculations give, but the effect of this error upon radiative transfer through gas layers with thickness greater than a millimeter and temperatures up to 20,000°K is negligible.

Photoionization from excited states and free-free transitions.--A modified hydrogen-like approximation is made where all chemical species are combined to form a mixture assumed to have only two species--one with charge $\bar{m} + 1/2$ and one with charge $\bar{m} - 1/2$ (Reference 16). Additional modification is required to extend the model to low temperatures. The exponential term in Equation (T-9) is allowed to increase with ω until a maximum value of

$$\frac{E_m}{4kT} \exp\left(\frac{E_m}{4kT}\right) + \exp\left(\frac{E_m}{9kT}\right)$$

is attained. This restriction allows Equation (T-9) to be used for gases where the degree of ionization is small. Additional details of this restriction are available in Reference 10, pages 27-28.

Photodissociation.--The model used for photodissociation is that of an electronic transition in a diatomic molecule, where transition occurs to a vibrational level in the upper electronic state higher than the dissociation continuum. This behavior can be predicted based on the shape of the intramolecular potential curves, and appears to be of importance in O_2 and C_2, among the species considered in this study. The formulation used is similar to that of Sulzer and Wieland (References 17 and 18) and requires estimation of the center and half-width of the peaked photodissociation band.

Diatomic molecule band system.--The electronic transitions in diatomic molecules are described using the just-overlapping-rotational-line model, as discussed in Reference 19. Most of the vibrational-state data necessary are found in Herzberg (Reference 20). Oscillator strengths and Franck-Condon factors are available in the technical literature. Where data are missing, they can be estimated based on a simple-harmonic-oscillator model for the upper and lower vibrational states (Reference 21).

Highly reliable values for k_ω are obtained if very small increments in ω are used to define the table of ω's at which the k_ω's are to be calculated. If these increments are chosen to be of the order of the half-width of the narrowest line, an unwieldly large amount of data results which cannot be adapted for radiative-transfer calculations. If the increment is chosen uniformly as, for example, one ten-thousandth of the band width of interest, there is no guarantee that sufficient spectral resolution has been obtained; in fact many important lines will certainly be neglected. The choice of wave numbers used must be influenced by the particular set of species, transitions, and temperature range selected. The technique used for this study chooses a good set of wave numbers at which k_ω should be calculated by the following built-in conditions: the ω-table must include the end points of the table of empirical data, line centers, points 5 cm^{-1} from line centers, values immediately before and after photoelectric edges, immediately before and after band heads, and at the center and two points in the wings of the photodissociation bands. On top of these points, additional ω's are determined by specifying a minimum ω-interval as a function of ω. This table of ω's then contains all the critical wave numbers that define positions in the spectrum where rapid changes of k_ω with ω occur. The table normally is still too big to allow for efficient radiative-transfer calculations, so the amount of data is reduced further through the following shock-layer-dependent procedure.

The absorption coefficients, k_ω, are calculated for the complete table of wave numbers for a specially chosen reference case. The computer code used for these calculations then will screen the produced data to determine if critical wave numbers could have been removed from the wave-number table without changing the values of k_ω more than some set accuracy criterion (typically, 1% was used as this criterion in the study). The wave-number table is reduced in size accordingly, usually cutting the size of the data tables by two-thirds. The new wave-number table is then used unaltered in all computations of k_ω for the actual conditions of pressure and temperature of interest. The temperature and species concentrations for the reference case, therefore, must be selected such as to accentuate those contributions for which fine detail in the wave-number table is required for accurate specification of the spectral absorption coefficients. A high temperature is specified for the reference case, firstly, because the radiation transfer to be calculated

is characteristically that for a high temperature layer, and secondly, to emphasize the atomic line contributions. The species concentrations are arbitrarily adjusted until adequate detail is obtained, i.e., isolated lines and band systems are well defined. Since the continuum contribution to the spectral absorption coefficients due to ionic species does not require great detail in the wave-number table, the concentrations of these species are greatly reduced from their expected high temperature values. Typically, two or three reference case trials are required to obtain satisfactory detail in the wave-number table for each gas mixture, e.g., air or air-carbon phenolic. Judicious selection of a reference case facilitates accurate and rapid radiative transport calculations and is clearly enhanced by the experience of the investigator.

Many of the radiative transfer cases to be solved for this study involved strong emission from high-temperature air, reabsorption in cooler air, and a second reabsorption and re-emission in regions containing ablation products. The change in chemical composition through the shock layer can drastically change the values of the k_ω when examined at a particular wave number. The absorption coefficient data used must be chosen to assure that all of the critical wave numbers associated with both air and ablation products are retained. It has been shown that approximate techniques for handling radiative transfer tend to be inadequate when gross changes in gas composition occur (References 3 and 6).

For this study, the problem was solved by choosing as a reference case, from which to derive the table of ω for all further calculations, an appropriate balanced mixture of air and ablation products. The important wave numbers for all species considered were retained in both pure air and pure ablation products regions of the shock layer.

The reference case used is shown in Figure 2, and many of the apparent contributions are identified thereon. The data presented in Figure 2 do not represent any real shock layer temperature-concentration case, but were computed to screen out automatically those wave numbers where nothing significant will happen in the shock layer. For air, 1154 points, for air-carbon phenolic, 1487 points, and for air-graphite, 1375 points resulted in the wave

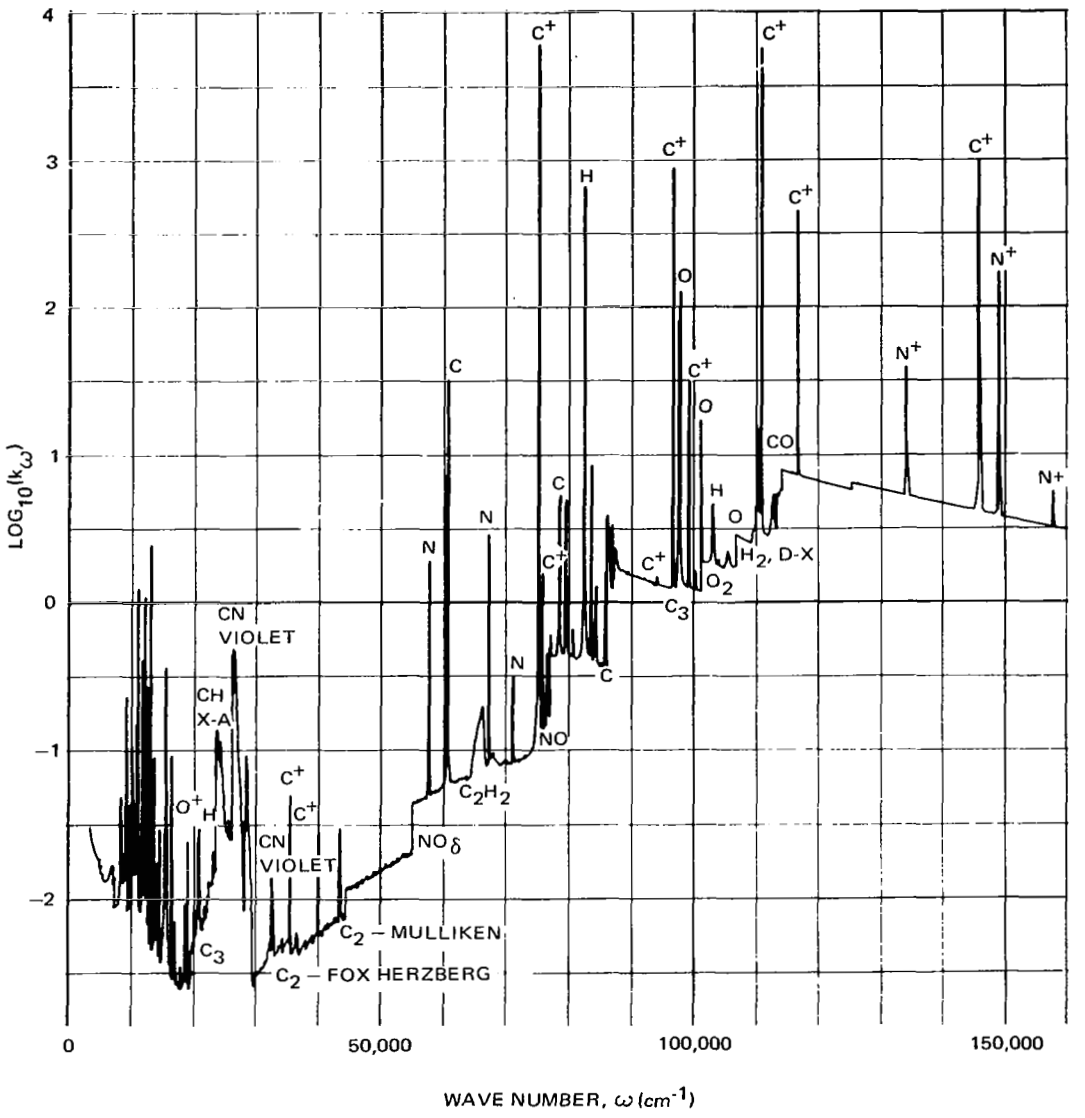

Figure 2. Spectral Absorption Coefficient of Air-Carbon Phenolic Ablation Products Mixture for P = 1 atm and T = 16,000 ^{0}K

number table. The variation of k_ω across the shock layer for an ablation products injection case is illustrated in Figure 3. The spectral absorption coefficients are shown for selected values of temperature and ablator (carbon phenolic) mass fraction.

The data used for the absorption coefficient calculations are presented in Appendix A. The species considered and the transitions treated are listed. Also, sources for much of the data are given.

Equation of Radiative Transfer

The radiative transfer along a path length through a nonscattering medium is described by the Lambert-Bouguer equation

$$\frac{dI_\omega}{ds} = k_\omega \left[B_\omega^\circ - I_\omega\right] . \tag{16}$$

The solution of this equation for a path length, t, is

$$I_\omega(t) = I_\omega(0)\exp\left(-\int_o^t k_\omega ds\right) + \int_o^t k_\omega B_\omega^\circ \exp\left(-\int_s^t k_\omega ds'\right) ds .$$

For this study the procedure followed is to solve Equation (16) directly. For the most part a second-order Runge-Kutta technique is employed. However, when the intensity at any wave number approaches the black-body value, the asymptotic form of Equation (16)

$$I_\omega \approx B_\omega^\circ - \frac{1}{k_\omega}\frac{dB_\omega^\circ}{ds}$$

is used. The use of this asymptotic expression for the intensity permits relatively large intervals to be used. Typical path length increments are on the order of 0.01δ, rather than intervals of the order of $1/k_\omega$ required for integration stability.

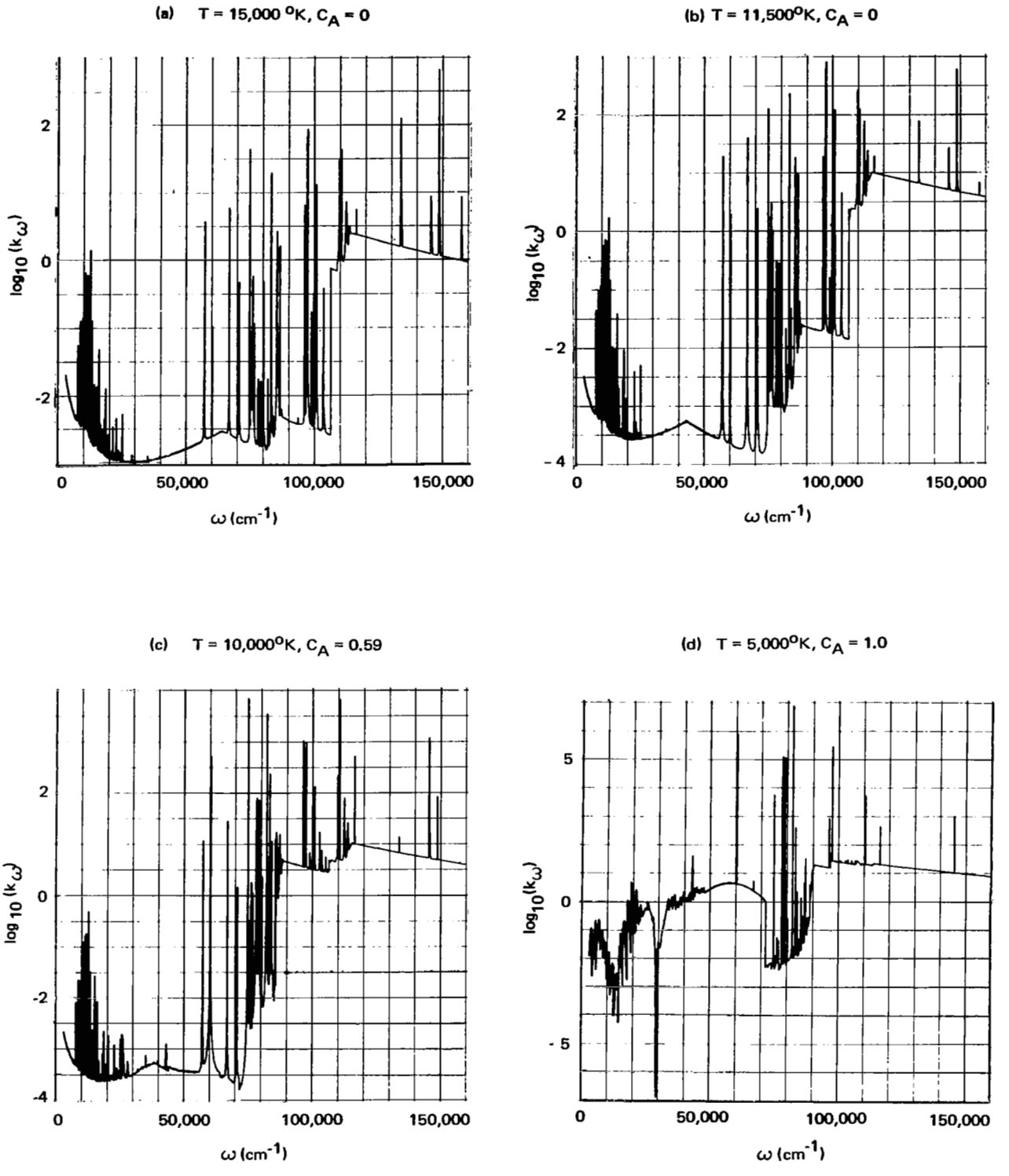

Figure 3. Typical Variation of k_ω Across the Shock Layer with Ablation Products Injection

The results of the first part of this study (Reference 2) showed that for realistic entry body materials the radiative properties of the wall have no significant effect on the shock-layer radiative transfer. Therefore, for all cases considered here the wall is assumed to be transparent. The boundary conditions for Equation (16) are

$$I_\omega(0,\theta) = 0 \qquad \text{for all } \omega \text{ and } 0 \le \theta \le \frac{\pi}{2}$$

$$I_\omega(\delta,\theta) = 0 \qquad \text{for all } \omega \text{ and } \frac{\pi}{2} \le \theta \le \pi$$

The positive (toward the shock) and negative (toward the wall) y-components of the flux are given by the following equations

$$F^+(y) = -2\pi \int_{\theta=o}^{\frac{\pi}{2}} \int_o^\infty I_\omega(y,\theta) \cos\theta \, d\omega \, d(\cos\theta) \tag{17}$$

$$F^-(y) = -2\pi \int_{\theta=\frac{\pi}{2}}^{\pi} \int_o^\infty I_\omega(y,\theta) \cos\theta \, d\omega \, d(\cos\theta) \tag{18}$$

The total flux is

$$F(y) = F^+(y) + F^-(y) \tag{19}$$

Approximate Representation for $\nabla \cdot \vec{F}$

Detailed evaluation of the flux divergence during the course of a flow field analysis can involve complex and time consuming calculations. As a result the appeal to develop an approximate method for calculating the divergence of the radiative flux is great. One of the objectives of this study was to obtain and use a simplified expression for the flux divergence suitable for application to high-temperature shock layer analyses.

During Phase I of this study an approximate relation was developed through an analysis of the important shock layer radiative transfer mechanisms. The resulting expression included "Planck-like" and "Rosseland-like" terms for atomic line emission and absorption plus terms for continuum absorption. Two models of continuum absorption were treated; the first assumed optically thick continuum transfer, and the second assumed pure absorption by the continuum. The derivation of the approximate relation is presented and discussed in References 2 and 6.

The results of comparing the approximate relation with detailed spectral calculations presented in Reference 2 indicated that the pure absorption model for continuum transfer should be used. The continued investigation of the approximate formulation revealed, however, that the pure absorption term should apply only for the radiation traveling toward the wall. Furthermore, in the derivation of the continuum absorption term the local flux toward the wall should be assumed proportional to the black-body emission at the temperature behind the shock, T_s, rather than at the local temperature. The resulting expression for the divergence of the flux is

$$\nabla \cdot \vec{F} = 2\bar{k}_P \sigma T^4 \left\{ \left(\frac{Bu_P}{Bu_P + \tau_P} \right)^{1/2} + \left(\frac{Bu_P}{Bu_P + \tau_{Po} - \tau_P} \right)^{1/2} \right\}$$

$$+ \frac{16}{3} \sigma T^3 \frac{dT}{dy} \left\{ \frac{\tau_L}{(Bu_L + \tau_L)^{1/2}} - \frac{\tau_{Lo} - \tau_L}{(Bu_L + \tau_{Lo} - \tau_L)^{1/2}} \right\}$$

$$+ \frac{15}{\pi^4} \sigma T^3 \frac{dT}{dy} \left(\frac{hc\omega_o}{kT} + 1 \right)^4 \exp\left(-\frac{hc\omega_o}{kT} \right) \left(\frac{\tau_c}{Bu_c + \tau_c} \right)^{1/2}$$

$$+ \frac{4\pi kc}{\sigma T_s^3} \exp\left(-\frac{hc\omega_o'}{kT_s} \right) \omega_o'^3 \bar{k}_c F^- \left(\frac{\tau_{co} - \tau_c}{Bu_c + \tau_{co} - \tau_c} \right)^{1/2} \qquad (20)$$

While three parameters, Bu_P, and Bu_L, and Bu_c, appear in Equation (20), only two are independent. The continuum and line Bouguer numbers are related through the equation

$$Bu_L = \left(\frac{\tau_{Lo}}{\tau_{co}} \right) Bu_c .$$

The procedure for evaluating the remaining two parameters involves a comparison of the fluxes at the wall and at the shock between approximate and detailed calculations. That is, the flow field solution is obtained using the approximate relation for $\nabla \cdot \vec{F}$ with assumed values for Bu_p and Bu_c. The resulting temperature profile is used for a detailed calculation of the flux at the boundaries. This detailed calculation may be made in roughly one-third the time required for a complete flux profile calculation. New values for Bu_p and Bu_c are selected and the iteration continues.

When the expression in Equation (20) is evaluated for a given temperature profile, reasonably good agreement is obtained with detailed flux divergence values. Figure 4 presents such a comparison of detailed and approximate divergence of the flux profiles as computed for a temperature profile obtained from the detailed flow field solution for the indicated entry conditions.

While the result shown in Figure 4 is encouraging, the complexity of the expression for the divergence of the flux given in Equation (20) is not. For an ablation products injection case, the flow field calculations require iteration on starting values for the flux toward the wall and the three optical depths--all evaluated at $\rho v = 0$, plus the three total optical depths, in addition to the iteration on T, u, dT/dy, and $\mu(du/dy)$ at $\rho v = 0$. In order to obtain the detailed fluxes at the wall and at the shock for evaluation of Bu_p and Bu_c, the spectral absorption coefficients must still be calculated for the ablation products-air mixture. Also, the mean absorption coefficients must be adjusted accordingly. It is apparent, therefore, that the time and effort saved over a detailed solution resulting from the approximate method would at best be slight.

In addition to the operational complexities associated with the approximate method as listed above, numerical integration stability problems were encountered when attempts to use the approximate formulation for the divergence of the flux in actual flow field calculations were made. In regions of negative $\nabla \cdot \vec{F}$, that is, where $\nabla \cdot \vec{F}$ <u>should be</u> negative, the magnitude and sign of the divergence of the flux, as given by Equation (20), becomes critically dependent on the local values of T and dT/dy. It is in these regions of the shock layer,

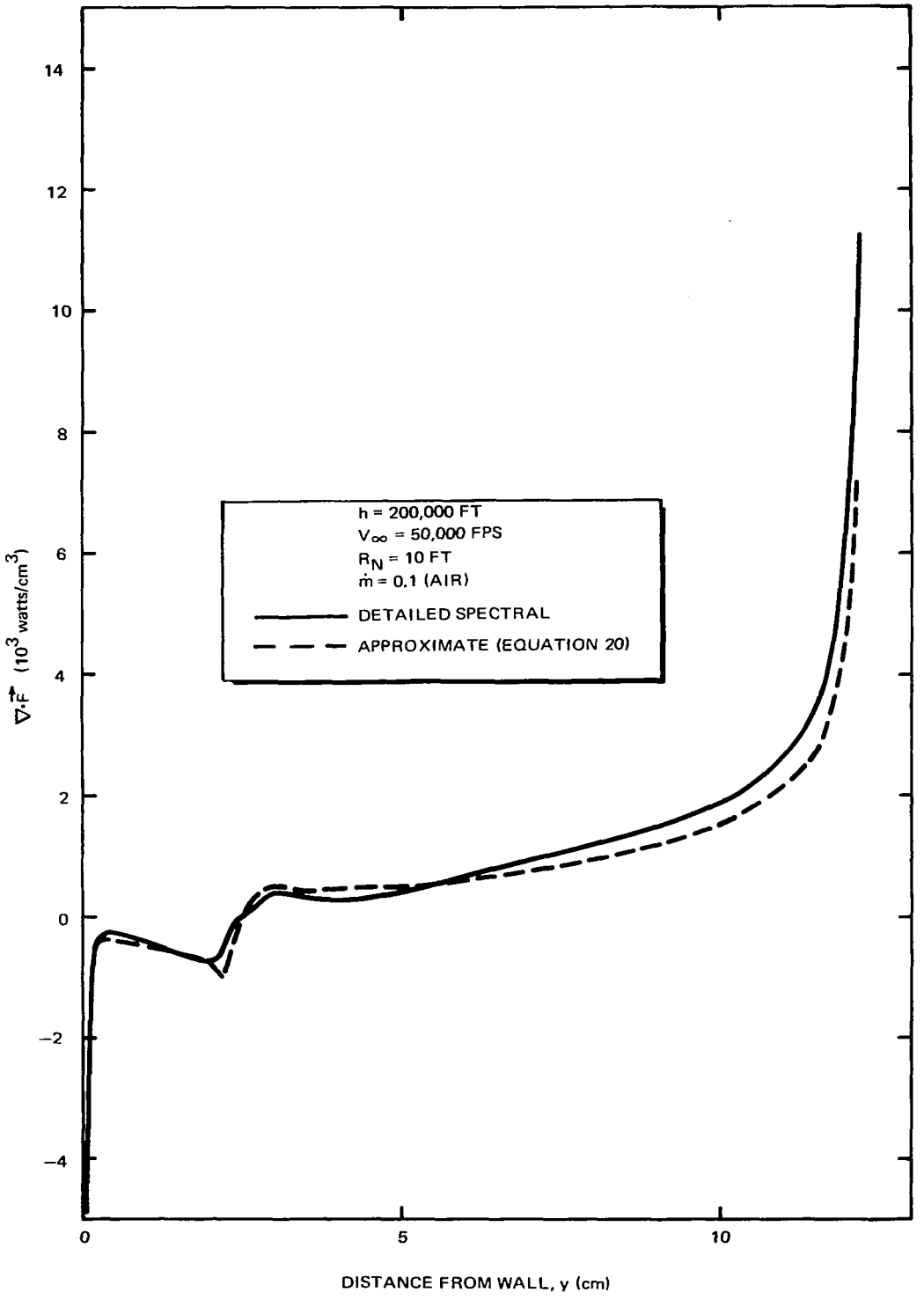

Figure 4. Comparison of Detailed Spectral and Approximate $\nabla \cdot \vec{F}$ Profiles

however, that the temperature profile is most sensitive to the divergence of the flux. An inherent instability is therefore introduced into the energy equation.

As a result of the overall difficulty associated with the approximate method, and the minimal time savings anticipated from its use, all further development of the approximate representation for $\nabla \cdot \vec{F}$ was abandoned.

Numerical Methods

The calculation of the radiation intensity profiles proceeds by solution of the normalized Lambert-Bouguer equation of transfer, viz.,

$$\frac{dI_\omega}{ds^*} = \delta k_\omega \left[B^\circ_\omega - I_\omega\right]$$

where

$$s^* = \frac{s}{\delta} \quad .$$

The numerical solution of this equation (or its asymptotic form) is generated for the line-of-sight path normal to the wall. Under the assumption that the temperature is a function only of y the intensities along other paths are obtained exactly by scaling procedures appropriate to the specified gas layer geometry. The computer code used to solve the equation of transfer includes the capability to consider a concentric spherical shock geometry, however, all calculations for this study were made assuming an infinite tangent slab shock layer. The spectral flux values are computed by Gaussian quadrature using intensities for eight slant directions. The integration of the flux over wave number is accomplished by a simple trapezoidal rule integration between each value of wave number. The limits of the integration over wave number used in all cases were 3,000 cm^{-1} and 160,000 cm^{-1}.

The shock layer temperature profile is specified by a table of 40 values of T versus y. The temperature used in the solution of the Lambert-Bouguer equation are obtained by linear interpolation in this table. Ten tables of absorption coefficient versus wave number are specified at ten values of

temperature. Logarithmic interpolation is used to obtain the spectral absorption coefficients at intermediate temperatures. The intensity and flux are computed at each value of wave number for which absorption coefficients are tabulated.

The selection of integration step sizes is optimized by dividing the shock layer into three regions. This procedure permits the use of larger integration intervals in regions of slowly varying temperature. For most of the cases considered in this study the spectral intensity and the spectral and integrated fluxes are computed at 65 points across the shock layer. The location of these points and the associated integration intervals are determined by specifying 50 intervals for $0 \leqq y/\delta \leqq 0.5$, 9 intervals for $0.5 < y/\delta \leqq 0.95$, and 5 intervals for $0.95 < y/\delta \leqq 1.0$.

A more complete description of the procedures used to calculate the intensities and fluxes is presented in Reference 9.

DISCUSSION OF RESULTS

For all of the cases considered in this study the flow field and radiative heating results are obtained by the detailed spectral method of solution. The conservation equations are solved, retaining the viscous and heat conduction terms across the entire shock layer, by the method discussed earlier. The radiation term in the energy equation is evaluated, retaining full spectral detail in the shock layer radiative properties, by the procedures outlined in the previous section.

A summary of the flow field and wall heating results for all cases considered is given in Appendix B. As shown in Appendix B, results have been obtained for several conditions of altitude, velocity, nose radius, and mass injection at the wall. However, not enough solutions have been obtained to attempt to develop a correlation equation for wall heat fluxes. The discussion presented here, therefore, is confined to a qualitative analysis of the results.

Solutions for No Blowing

The radiative heat transfer rate without blowing and normalized with the freestream flow energy is shown in Figure 5. Also shown are the results of Wilson and Hoshizaki (Reference 3) and Page, et al., (Reference 4) which include the effect of energy transport by atomic lines. These results are about 20% lower than the present results when preheating is not included. Significant differences between the methods used for these computations preclude the possibility of identifying the exact causes for this difference. Both Wilson and Page employed simpler equivalent line group models to determine line transport rather than the detailed line-by-line treatment of this work. The effect of this approximation is uncertain. Thomas (Reference 6) has made a direct comparison between these two methods and found, for a case typical of those considered here, that the line grouping technique

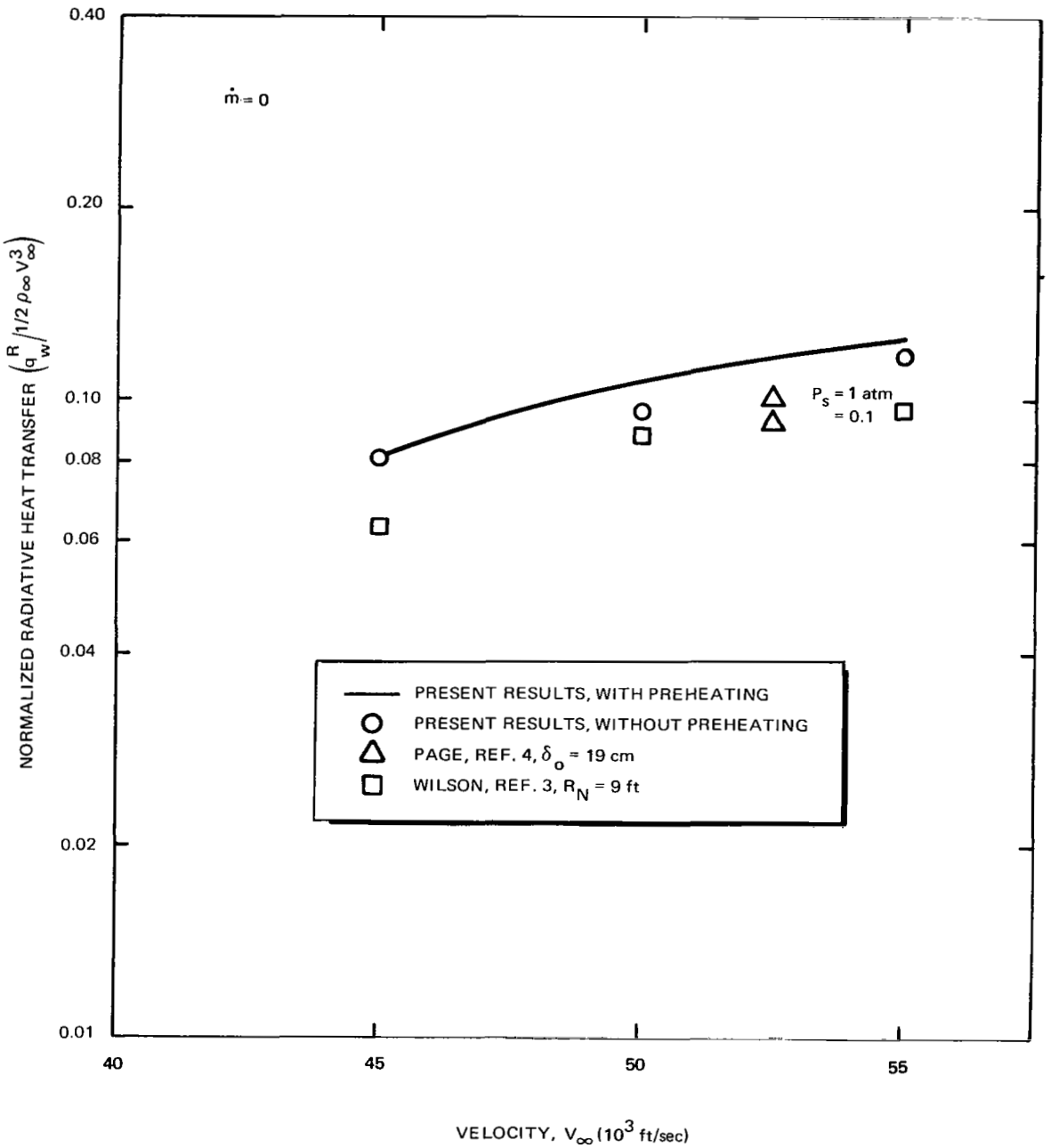

Figure 5. Radiative Heat Transfer with and without Preheating

underpredicted the total radiative flux at the wall by about a third. Wilson, however, has made the same comparison and found that five line groups underpredicted the cold wall flux by only 7%. It is not clear whether the attenuation of the line emission by the background continuum was included in this comparison.

Absorption of radiant energy by the cool air ahead of the shock was included using the method described earlier. It was found that this absorption was only important for the 10-foot nose radii cases at 50,000 and 55,000 feet per second velocity, and even for these cases increased the radiative heat transfer rate by less than 10 percent. As noted earlier, the primary effect of the increase in static enthalpy ahead of the shock wave is to raise the temperature immediately behind the shock wave. At a velocity of 50,000 feet per second this increase was only 200°K while at 55,000 feet per second it amounted to 500°K. These increases in T_s were used in the solutions of the ablation cases to be discussed subsequently since the forward traveling radiation emitted from the shock layer is relatively insensitive to the presence of an ablation products layer close to the wall. Figure 6 shows the integral of the spectral flux absorbed by the cool air. All of this absorption takes place above 67,000 cm^{-1} wave numbers. As pointed out in Reference 22, cold air would be expected to absorb strongly above 125,900 cm^{-1} due to the photoionization of nitrogen molecules. Somewhat less absorption would be expected from 97,600 cm^{-1} to 125,900 cm^{-1} from photoionization of O_2. The present results indicate that while the N_2 photoionization process does indeed absorb completely the energy above 125,900 cm^{-1}, the fraction is small because little energy is emitted from the shock layer in this spectral range. O_2 absorption on the other hand accounts for almost half of the total energy absorbed. The remainder of the energy is apparently absorbed by N lines resulting from the increased temperature ahead of the shock. The rise in temperature ahead of the shock wave is illustrated in Figure 7. The bulk of the absorption is seen to occur within about two shock layer thicknesses validating the neglect of three-dimensional effects.

The results for case numbers 2 and 3 (Appendix B, Table B-1) reveal that the shock layer radiation transport is insensitive to the wall temperature. However, the convective heat flux at the wall does decrease as the wall temperature increases.

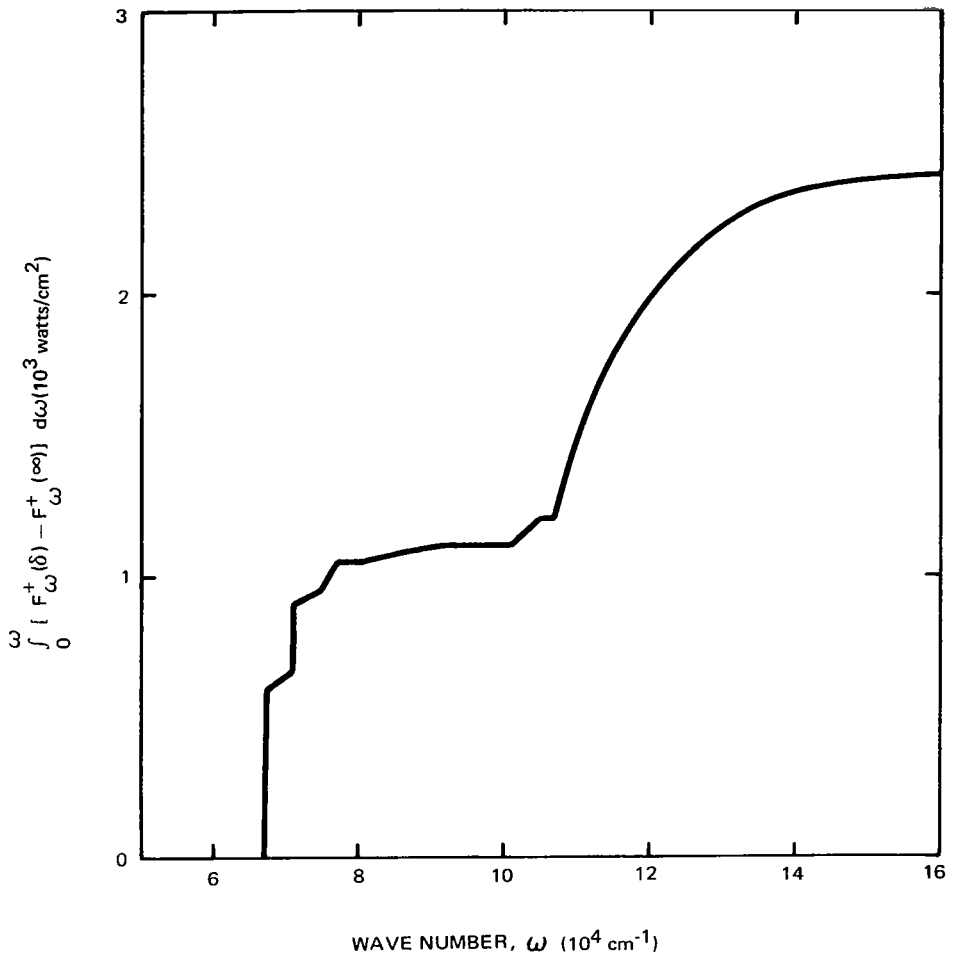

Figure 6. Spectral Absorption of Radiation by Ambient Air

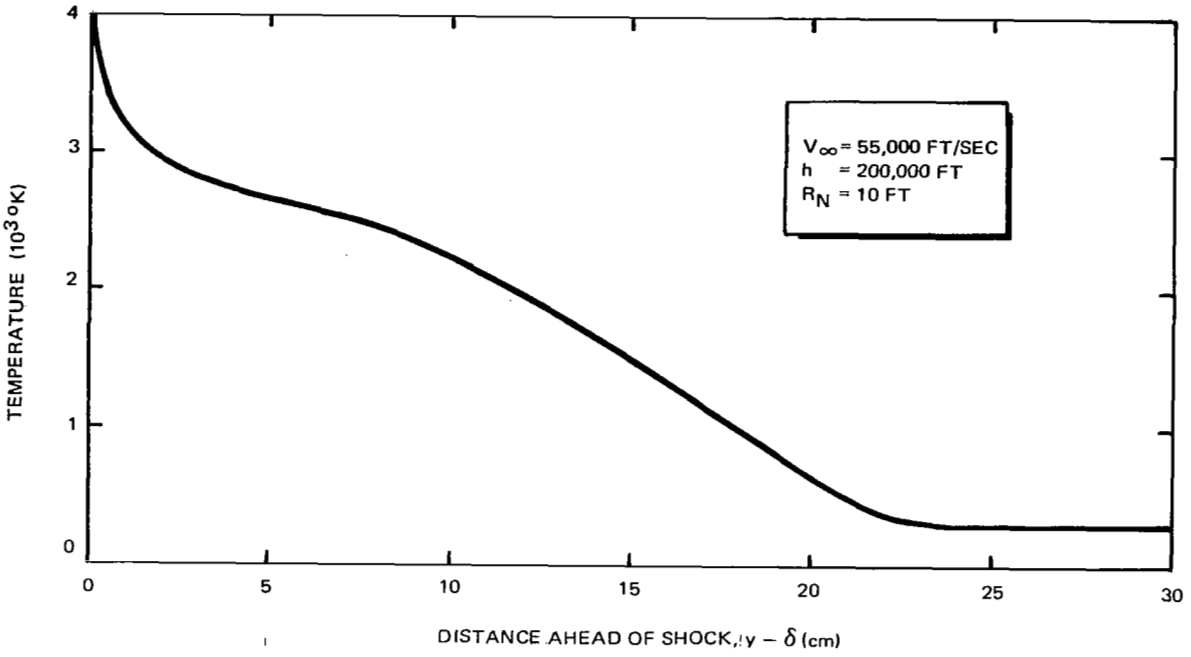

Figure 7. Temperature Profile in Preheating Region

Air Blowing and Wall Ablation

Accurate prediction of the effect of ablation (or blowing) at the wall on the radiative heat transfer rate requires an accurate analysis of the properties of the ablation gas layer. In particular, the temperature and thickness of this layer are of prime importance. The present results consider the solution of the differential form of the energy and momentum equations across the entire shock layer including both viscosity and heat conduction. As pointed out previously, this approach requires integration in both directions from $\rho v = 0$ in order to maintain numerical

stability and therefore requires iteration on the unknown values of u and T at $\rho v = 0$. Simpler methods have been tried by various investigators to circumvent this added complication, however, as shown in Figure 8 the ablation layer thickness is not accurately determined by these approximations. The integral technique used by Hoshizaki with much success for the no-blowing problem fails to correctly predict the ablation layer thickness within a factor of four. This is not surprising since the form of the u velocity profile has been known for some time not to obey a simple quadratic or cubic polynominal law as used in that work. The inviscid technique developed by Thomas and Wilson (as reported in Reference 22) underpredicts the ablation layer thickness by almost a factor of two. In the limit of very large Reynolds numbers this technique should give a much better representation of the u velocity profile than evidenced in Figure 8. However, since the energy equation is singular at $\rho v = 0$ when energy transport by heat conduction is not included, the temperature profile is poorly represented by this model thereby affecting the u velocity profile.

The effectiveness of an injected gas layer in reducing the radiative heat flux at the wall is illustrated in Figure 9. Carbon phenolic vapor is seen to be about twice as effective as air. From Figure 10, which shows the spectral flux integral, it is seen that the injected air layer is almost 100% effective in absorbing the radiative flux above 80,000 cm^{-1} wave numbers and that some absorption of the strong lines in the region 60 to 80,000 cm^{-1} occurs. The carbon phenolic vapor products layer is virtually 100% effective in absorbing all the radiation above 40,000 cm^{-1}; a small increase in flux from 13,000 to 35,000 cm^{-1}, apparently due to radiation from molecular carbon species, is evident.

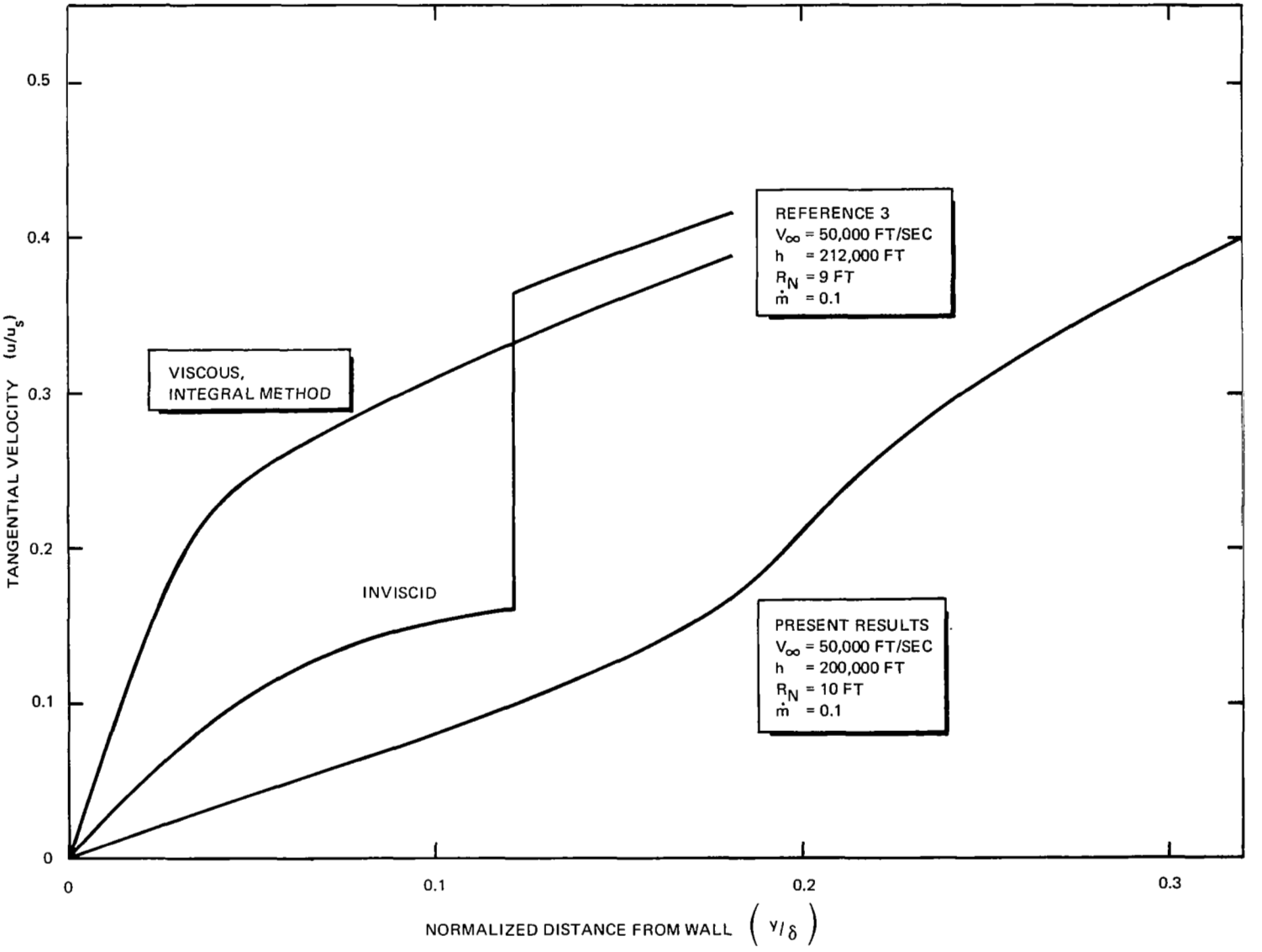

Figure 8. Comparison of Tangential Velocity Profiles with Strong Blowing

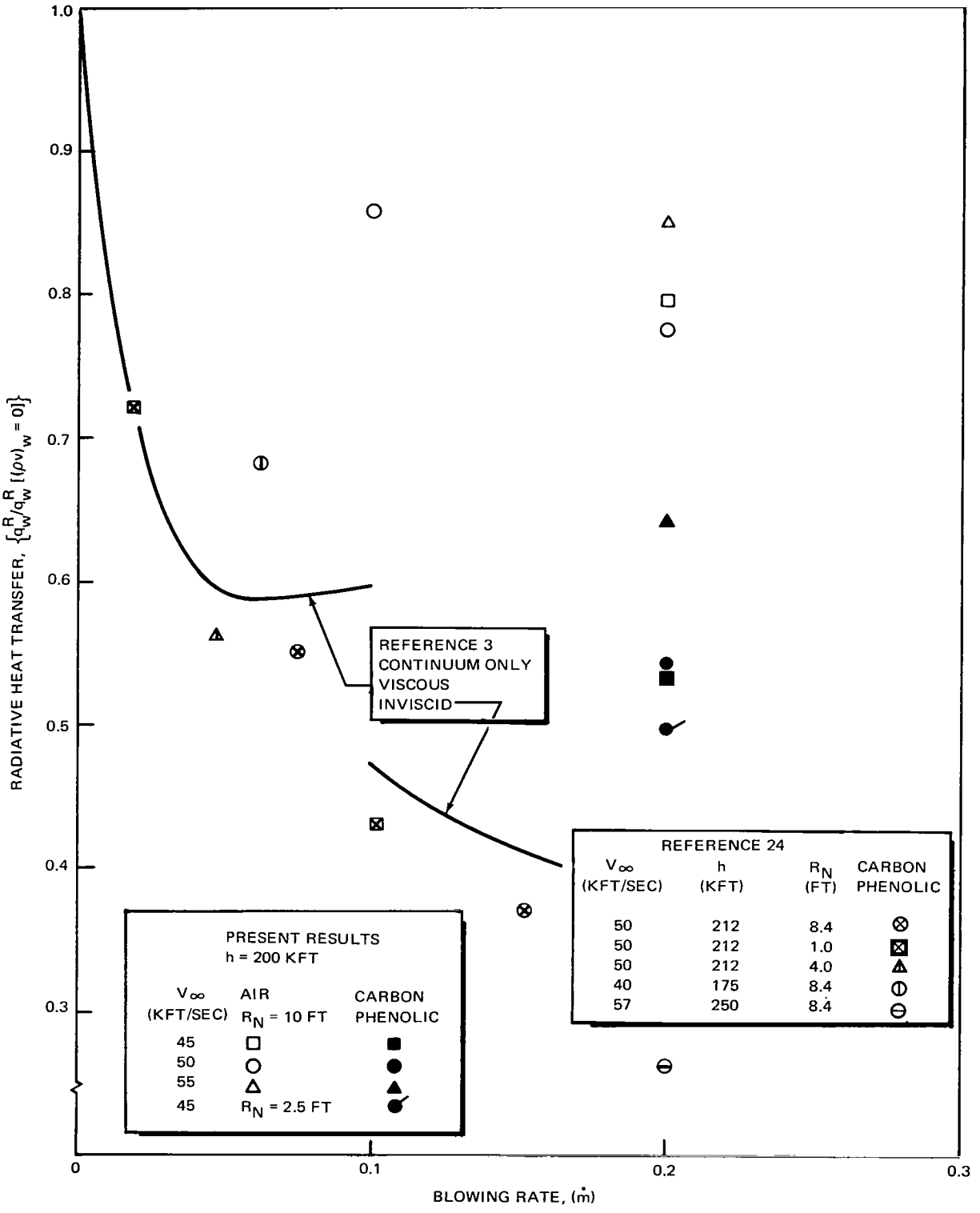

Figure 9. Effectiveness of Blown Gas in Reducing Radiative Heat Transfer

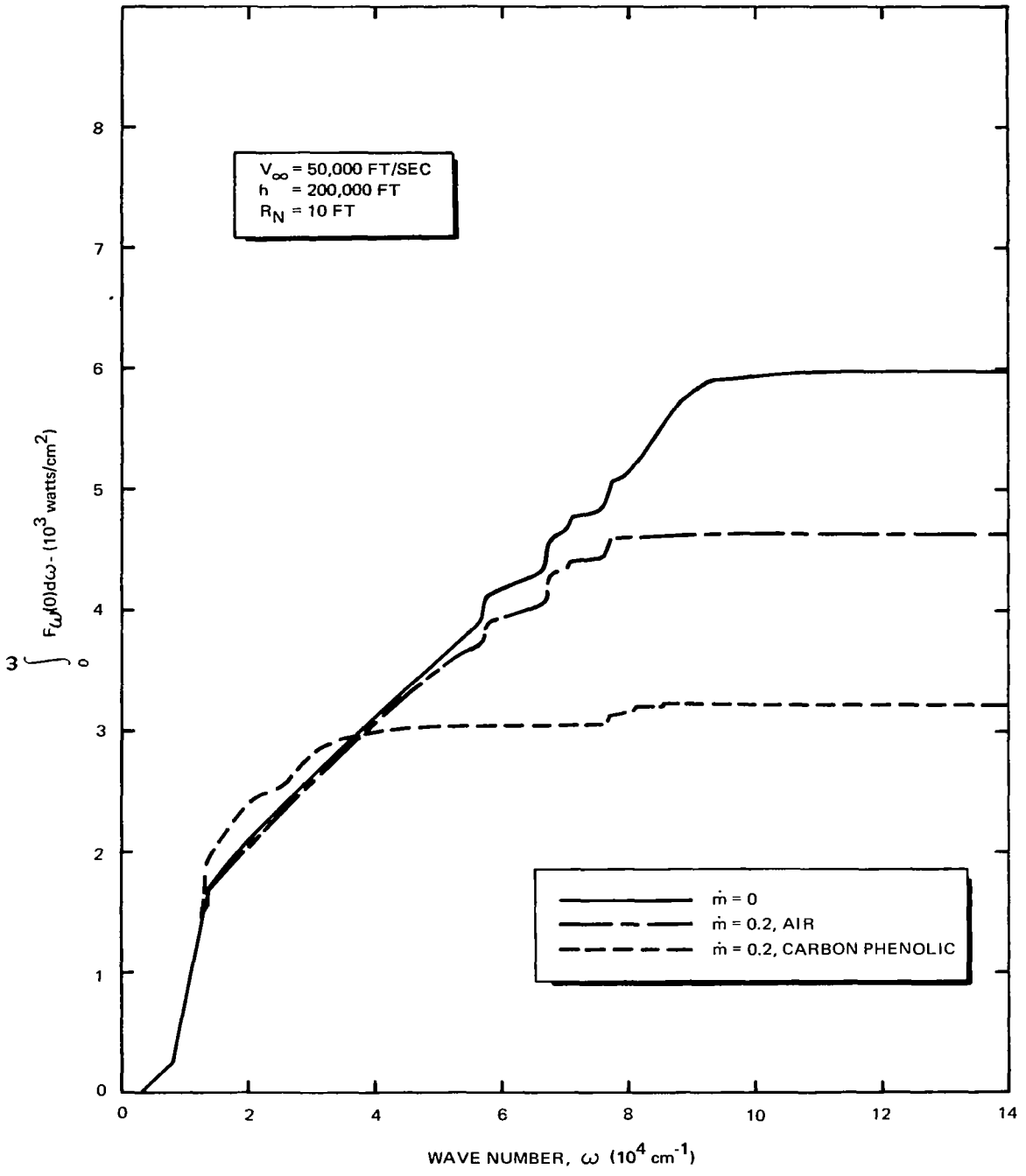

Figure 10. Spectral Contribution to Radiative Flux at Wall

Returning to Figure 9, a comparison is drawn between the results of the present analysis and the work of Chin (Reference 23) and that of Wilson and Hoshizaki (Reference 3). Chin's results are based on an inviscid two-layer model considering the effects of energy transport by lines. Only lines from nitrogen and oxygen atoms in the air layer are considered. These are treated using 18 line groups, three of which contain only a single isolated line. The results of Wilson and Hoshizaki are limited to continuum only radiation transport since the line-grouping technique they had previously employed to compute energy transport by lines is invalid when changes in elemental species composition occur across the radiating layer. For the cases of interest here, the ablation products layer contains mostly C atoms while mainly N and O atoms are present in the air layer. Since the lines from these two groups of elements are well isolated, use of a line-grouping technique which requires all lines in the group to emit at the same frequency will overpredict the absorption by the carbon vapor layer. The present results for carbon phenolic vapor products, which consider energy transport by individual lines, fall above the results of both Chin and Wilson. Although a detailed comparison of the radiative transport properties and numerical methods used in these investigations is beyond the scope of this report, the primary difference appears to lie in the treatment of the infrared lines from N and O atoms. As indicated in Figure 10, virtually no absorption of these lines by either the air or carbon phenolic vapor layer occurs. Since the radiation from the infrared lines constitutes about 50 percent of the radiation reaching the wall for the injection cases, their omission, as in Hoshizaki's continuum only analysis, will significantly increase the apparent effectiveness of the injected vapor in reducing the wall radiative flux. Chin's results for the wall flux with no ablation layer are about fifty percent lower than those given in Figure 5 and this difference appears to be primarily in the contribution of the infrared lines and the infrared and visible continuum. (The contribution of the N^+ continuum was neglected in Chin's work.) Again decreased emission in these frequency intervals will yield higher apparent effectiveness for the injected vapor.

Figure 9 also indicates a reduction in effectiveness of carbon phenolic vapor as an absorber as the velocity is increased. Reference to the figures for case numbers 8, 16, and 19 (Appendix B, Figures B-8, B-16, and B-19) indicates that this result is due to lessened absorption of the continuum between 30,000 and 70,000 cm^{-1}. The figures also show that this decreased absorption is due to higher temperatures over the bulk of the vapor region as the entry velocity increases resulting in a substantial decrease in the concentration of molecular carbon species and CO, which are primarily responsible for the absorption in this wavelength region. This effect is illustrated graphically in Figure 11.

In addition to the carbon phenolic ablation cases, one case of graphite ablation was considered. While graphite is probably not a suitable ablator for large nose radius vehicles due to structural considerations, the results of this case do indicate the relative importance of the hydrocarbon molecules and carbon monoxide in absorbing radiation. Comparing the results of case numbers 8 and 11 (see Table B-1, Appendix B) it is seen that for corresponding entry conditions and injection rates the carbon phenolic vapor is approximately 7% more effective in absorbing radiation than pure carbon vapor.

The above conclusions apply to the baseline cases of ablation product absorption which considered the ablation products vapor to have the same thermodynamic and transport properties (i.e., ρ, c_p, K, and μ) as air. Two cases were studied to determine the effect of correcting these properties in accord with the actual species composition across the region. The change in the radiative flux toward the wall as a function of assumed thermodynamic properties is shown in Figure 12. Two models were considered in addition to the baseline model. In the first the thermodynamic properties, ρ and c_p, were modified at each major iteration along with the radiative properties to correspond to the actual distribution of species across the shock layer. For the second model, all thermodynamic and transport properties corresponded to those of the actual species present. The figure shows that the change in ρ and c_p substantially modifies the radiative energy transport in the carbon

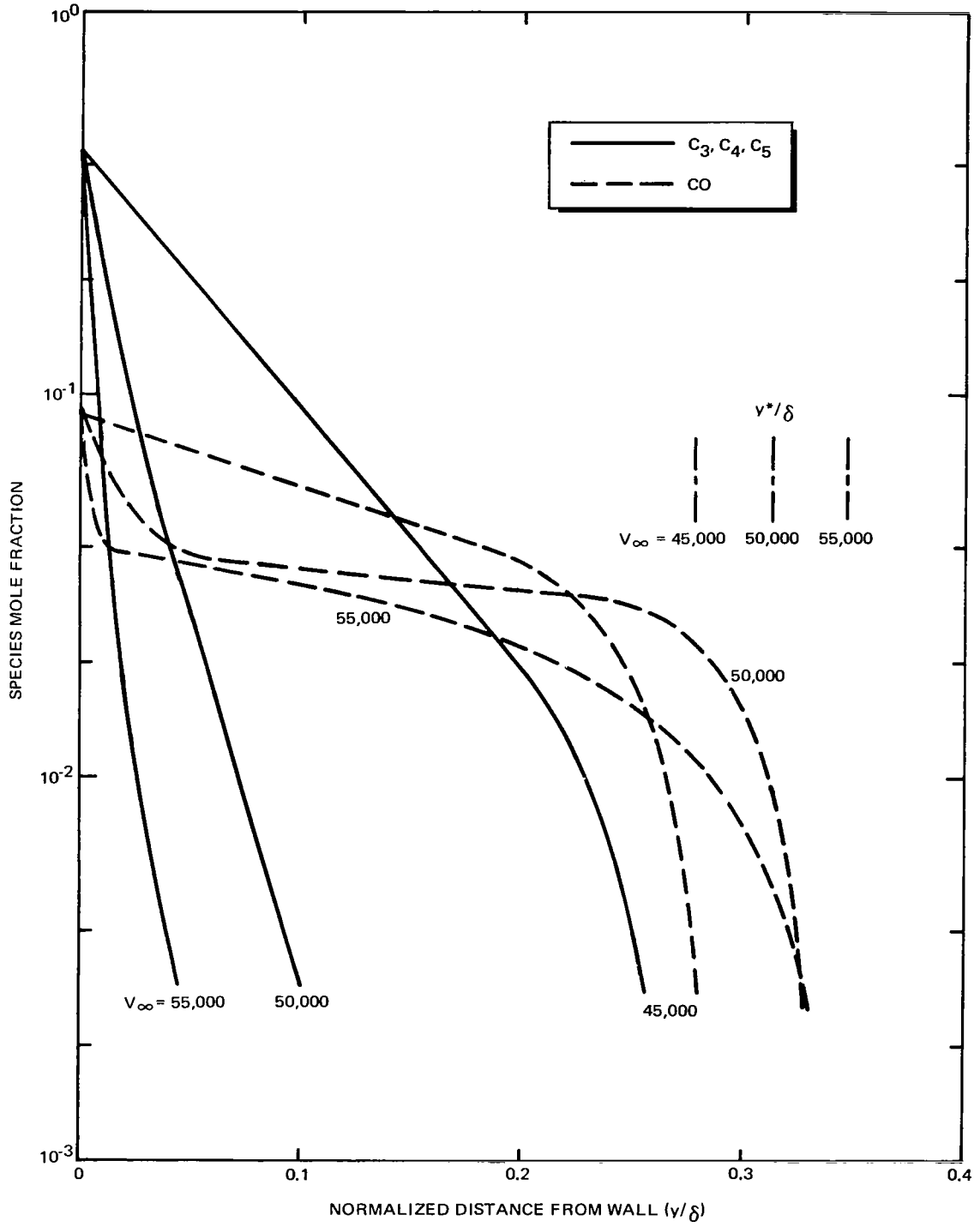

Figure 11. Molecular Concentration Profiles for the Ablation Layer

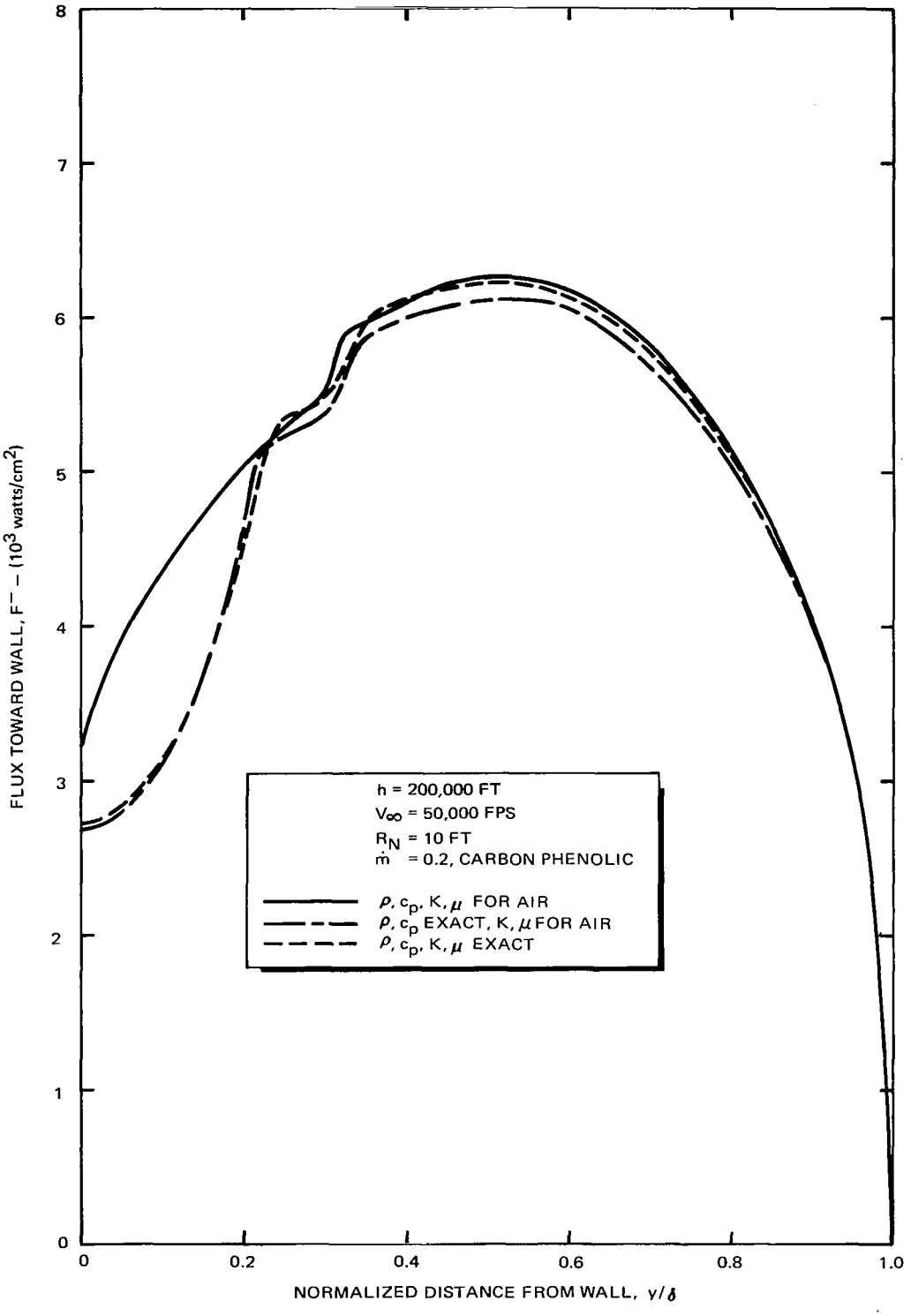

Figure 12. Effect of Thermodynamic and Transport Properties on F^-

phenolic vapor region resulting in increased absorption by the vapor layer. Modification of K and μ has a negligible effect on the radiative energy transport since the effect of those variables is confined to a relatively narrow region around $\rho v = 0$. Figure 13 shows the relative difference in the carbon phenolic-air mixture and air thermodynamic and transport properties, for the actual distribution of species obtained for this case.

Comparison of Figures B-3, B-7, B-8, B-9, and B-10 reveals the effect of ablation and ablator properties on the shock layer temperature profile. A relatively low temperature is maintained throughout the injected gas region when the blowing rate is a significant fraction of the freestream mass flux. This result is not unexpected since similar results have been obtained when radiation was not an important mode of energy transport. The effects of molecular heat conduction are confined to a thin layer centered about $\rho v = 0$ and it is in this region that the most pronounced equilibration between the wall temperature and shock temperature occurs. The temperature in the injectant region is significantly affected by both the absorption of radiant and the specific heat of the injectant. Figures B-7 and B-8 show that the increased absorption of radiation resulting from the use of carbon phenolic ablation products radiative properties tends to increase the temperature in the injectant layer. This tendency is evidenced by a sharper temperature rise near the wall for case number 8. Comparison of Figures Figures B-8, B-9, and B-10 reveals that a much lower temperature across the injected gas region is obtained when the carbon phenolic thermodynamic properties are used. This effect is a natural consequence of the specific heat of carbon phenolic being 4 to 10 times greater than that for air in the temperature range 3500°K to 5000°K (see Figure 13). The effect of the carbon phenolic transport properties on the temperature profile is confined to the narrow region around $\rho v = 0$. While the temperature across the injectant layer in case numbers 9 and 10 is significantly lower than for case number 8, it is interesting to note that the thickness of the ablation layer is nearly constant for these three cases. This effect is a result of the density of carbon phenolic being lower than the density of air.

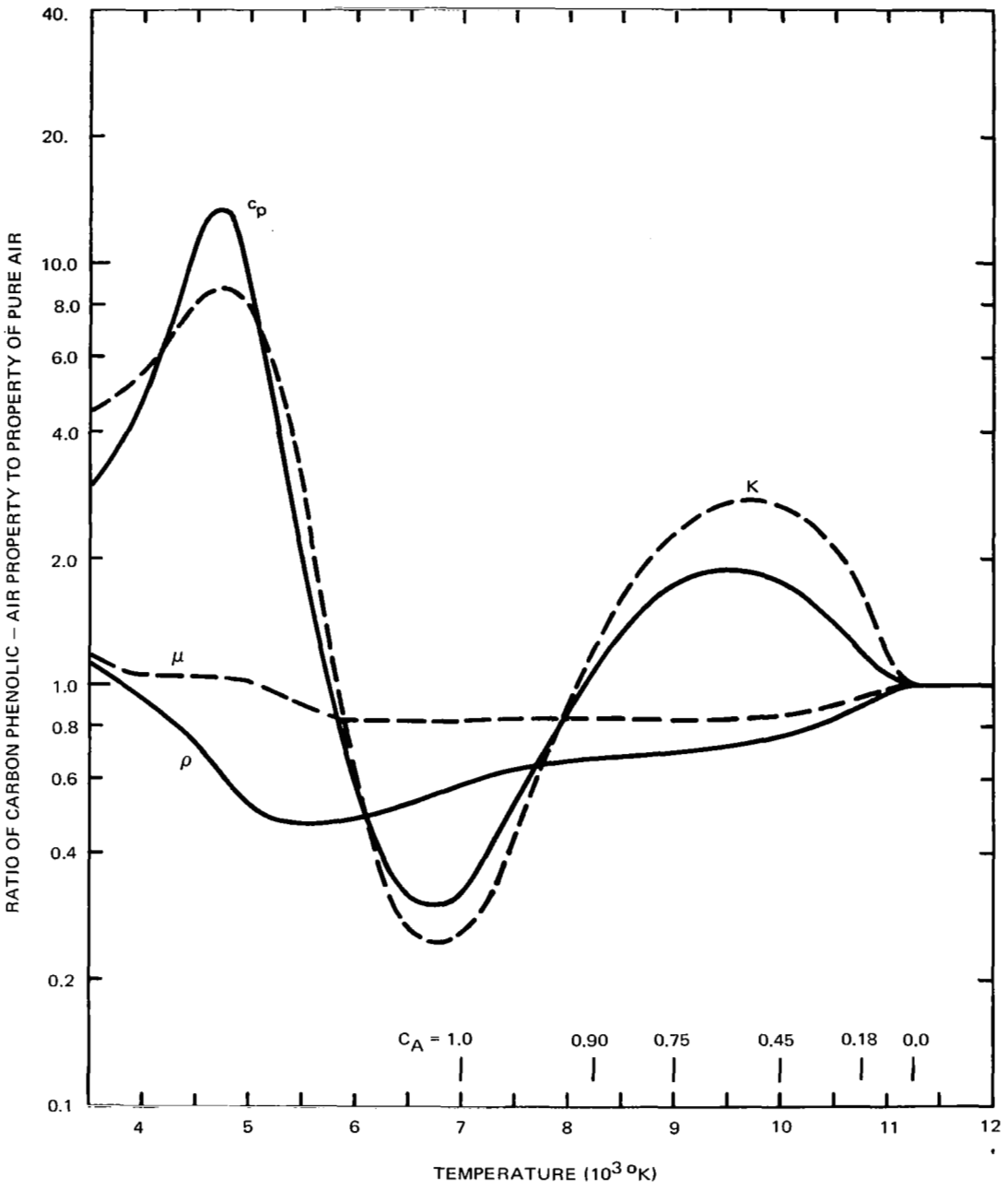

Figure 13. Comparison of Properties of Air and Carbon Phenolic - Air Mixture

CONCLUSIONS

The stagnation-point thin-shock-layer equations have been solved using detailed spectral calculations of the radiative transfer. Both air blowing and ablation products injection at the wall have been considered. The investigation of ablation products injection has included an examination of the effects of the thermodynamic and transport as well as the radiative properties of the ablation products on the radiative flux. Also, the effect of radiative preheating of the ambient air ahead of the shock has been investigated. Finally, an attempt was made to develop an approximate formulation for the divergence of the radiative flux which would simplify the analysis of hypervelocity entry vehicle shock layers.

The results of this study have shown that accurate calculations of the radiative flux to a hypervelocity entry vehicle undergoing ablation must include detailed descriptions of the distinctly different radiative properties of the ablation products and air. Furthermore, the thermodynamic properties of the ablation products must be properly described.

The results have also shown that radiative preheating of the air ahead of the shock wave increases the wall heat flux by less than 10% for entry velocities up to 55, 000 feet per second and shock layer pressures of approximately 1 atmosphere. For these conditions a one-dimensional treatment of the radiant energy transport forward of the shock is justified. However, the increase in ambient temperature ahead of the shock wave should be computed in order to accurately account for the absorption processes.

The detailed calculation methods utilized in this study are, indeed, time consuming; hence the need for approximate computation procedures remains. The quasi-locally evaluated approximate formulation for the net radiant

emission investigated in this study leads to integration instabilities and is so complex that little time savings would result from its use. Simplified approaches to the analysis of the radiation transport, e.g., line grouping, fail to account for the changes in emission and absorption characteristics with changes in elemental mass fractions across the shock layer resulting from ablation products injection at the wall. The most obvious approximate procedure to pursue is to simply relax the accuracy requirements on the detailed spectral method utilized here. For an ablation products injection case the ablation products thermodynamic and radiative properties could be corrected only at the first iteration. The iteration on the flux profiles could be carried out until only 5% agreement in the flux profiles is obtained. The use of this type of approximate procedure for a parametric analysis is particularly appealing since the iteration procedures can be carried out with greater accuracy at selected points in the array of entry conditions considered. Since the viscous, heat conduction, and diffusion effects seem to be confined to a narrow region around $\rho v \approx 0$, a properly formulated inviscid, non-heat conducting, two-layer analysis should yield accurate results for large injection rates at velocities greater than 50,000 feet per second.

Appendix A
GAS MIXTURE PROPERTIES

All of the thermodynamic, transport, and radiative properties for the shock layer gas mixtures considered in this study were computed for each stagnation pressure encountered. The procedures used to calculate the species concentrations and thermodynamic properties are described in detail in Reference 25. The transport properties are computed by the techniques presented in Reference 26. For the calculation of the thermodynamic and transport properties of air the following species were considered: N, O, N_2, O_2, NO, NO^+, N^+, O^+, N^{++}, O^{++}, e^-. For case number 9 the thermodynamic properties, and for case number 10 the thermodynamic and transport properties of the carbon phenolic-air mixture were computed. For these calculations the species considered were: N, O, C, H, C_2, H_2, CO, N_2, O_2, NO, C_2H_2, CH, C_3, C_4, C_5, C_2^-, CN, O^-, O_2^-, C^-, H^-, N^+, O^+, C^+, NO^+, H^+, N^{++}, O^{++}, C^{++}, e^-.

The methods used for calculating the spectral absorption coefficients have been discussed previously. Two steps are involved in the determination of the radiative properties. First, the species concentrations are computed, then, secondly, the actual absorption coefficient calculations are made. Some additional species were considered when computing the thermodynamic equilibrium conditions, but only those species with known or suspected radiative contributions were included in the k_ω calcuations. Also, species were lumped together when similar radiative properties were expected. Thus, for air the concentrations were computed for the species: N, O, C, N_2, O_2, NO_2, CO_2, NO, CN, CO, O^-, O_2^-, N_2^+, NO^+, N^+, O^+, C^+, N^{++}, O^{++}, C^{++}, e^-. For the spectral absorption coefficient calculations this set of species was reduced by grouping O^- and O_2^-, N_2^+ and NO^+, the doubly ionized species, and by ignoring the electron.

For the carbon phenolic-air mixture the concentrations were computed for the species: N, O, C, H, C_2, H_2, CO, N_2, O_2, NO, C_2H_2, CH, C_3, C_4, C_5, C_2^-, CN, O^-, O_2^-, C^-, H^-, N^+, O^+, C^+, NO^+, H^+, N^{++}, O^{++}, C^{++}, and e^-.

For the k_ω calculations the species C_2^-, NO^+, H^+, and the electron were ignored. Also, the following groupings were made: C_3, C_4, and C_5; O^- and O_2^-; C^- and H^-; and N^{++}, O^{++}, and C^{++}. For the graphite-air mixture all species containing hydrogen were eliminated from the above sets of species. The transition data used in the spectral absorption coefficient calculations are listed in Table A-1.

The elemental mass fractions defining the basic gas mixtures considered in this study are presented in Table A-2. The species mole fractions used for the carbon phenolic-air absorption coefficient calculations reference case are given in Table A-3.

TABLE A-1

TRANSITION DATA

Species (E_m, eV)	Usage*	Transition	f-Number	Reference	FC-Factor	Reference	Number of Bands or Lines
N	A, B, C	Isolated atomic lines	NBS	12, 13			42 (44 for pure air)
(14, 48)	A, B, C	Overlapping atomic lines					$\omega > 109,000\ cm^{-1}$
O	A, B, C	Isolated atomic lines	NBS	12, 13			42 (38 for pure air)
(13, 55)	A, B, C	Overlapping atomic lines					$\omega > 106,500\ cm^{-1}$
C	B, C	Isolated atomic lines	NBS	13			7
(11, 2)	B, C	Overlapping atomic lines					$\omega > 85,880\ cm^{-1}$
H	B	Isolated atomic lines	NBS	13			20
(13, 6)	B	Overlapping atomic lines					$\omega > 109,200\ cm^{-1}$
C_2	B, C	$X^3\Pi_u \rightarrow A^3\Pi_g$ (Swan)	0.048	27	Morse	28	27
(12, 0)	B, C	$b^1\Pi_u \rightarrow c^1\Pi_g$ (d'Azambuja)	0.065	27	Morse	28	16
	B, C	$X^1\Sigma_g^+ \rightarrow d^1\Sigma_u^+$ (Mulliken)	0.102	27	Morse	28	9
	B, C	$X^3\Pi_u \rightarrow A'^3\Sigma_g^-$ (Ballik-Ramsay)	0.0066	27	SHO		25
	B, C	$X^3\Pi_u \rightarrow B^3\Pi_g$ (Fox-Herzberg)	0.818	27	Morse	28	22
	B, C	+ photodissociation	0.82	27	ω_c = 58,000 cm^{-1}, $\Delta\omega$ = 5500 cm^{-1}		
H_2	B	$X^1\Sigma_g^+ \rightarrow D^1\Pi_u$	0.16	Calculated from 29	SHO	21	39
(15, 6)	B	$X^1\Sigma_g^+ \rightarrow B^1\Sigma_u^+$ (Lyman)	0.5	Estimated	SHO	21	45
CO	A, B, C	$X^1\Sigma^+ \rightarrow A^1\Pi$ (4+)	0.003	Estimated	Morse	39	40
(14, 1)	B, C	$X^1\Sigma^+ \rightarrow B^1\Sigma$ (Hopfield-Birge)	0.01		SHO	21	32
	B, C	$B^1\Sigma^+ \rightarrow A^1\Pi$ (Angstrom)	0.003	Estimated	SHO	21	35
	B, C	$A^1\Pi \rightarrow C^1\Sigma^+$ (Herzberg)	0.004	Estimated	SHO	21	35
	B, C	$a^3\Pi \rightarrow a'^3\Sigma$ (Asundi)	0.002	Average of data in 28	Morse		44
	B, C	$d^3\Delta \rightarrow a^3\Pi$ (triplet)	0.006		Morse		44
N_2	A	$X^1\Sigma_g^+ \rightarrow a^1\Pi_g$ (LBH)	10^{-5}	36	Morse	37	43
(15, 5)	A, B, C	$B^3\Pi_g \rightarrow C^3\Pi_u$ (2+)	0.036		Morse	37	31
	A, B, C	$X^1\Sigma_g^+ \rightarrow b'^1\Sigma_u^+$ (Worley)	0.5	Calculated from 38	SHO	21	27
	A, B, C	$X^1\Sigma_g^+ \rightarrow b^1\Pi_u$ (Birge-Hopfield)	0.04	Estimated	Morse	39	27
	A, B, C	$A^3\Sigma_u^+ \rightarrow B^3\Pi_g$ (1+)	0.0028		Morse	37	46
O_2	A, B, C	$X^3\Sigma_g^- \rightarrow B^3\Sigma_u^-$ (Schumann-Runge) Photodissociation	0.163	34	ω_c = 69000 cm^{-1}, $\Delta\omega$ = 5700 cm^{-1} (ref. 38)		
(12, 5)							
NO	A, B, C	$X^2\Pi \rightarrow A^2\Sigma^+$ (γ)	0.0025	40	Morse	41	32
(9, 5)	A, B, C	$X^2\Pi \rightarrow B^2\Pi$ (β)	0.0024	40	Morse	41	32
	A, B, C	$X^2\Pi \rightarrow C^2\Sigma^+$ (δ)	0.017	40	Morse	40	32
	A, B, C	$X^2\Pi \rightarrow D^2\Sigma^+$ (ε)	0.013	40	Morse	40	32
C_2H_2	B	Vacuum UV	Empirical	31	Table Length	30	
(11, 6)							
CH	B	$X^2\Pi \rightarrow A^2\Delta$	0.0049	30	Morse	45	6
	B	$X^2\Pi \rightarrow B^2\Sigma^-$	0.0012	30	Morse	45	20
C_3	B, C	$X^1\Sigma_g^+ \rightarrow A^1\Pi_u$ (Swings' comet-head)	Empirical	30	Table Length	11	
(12, 0							
CN	A, B, C	$X^2\Sigma^+ \rightarrow A^2\Pi_i$ (Red)	0.008	42	Morse	43	26
(14, 0)	A, B, C	$X^2\Sigma^+ \rightarrow B^2\Sigma^+$ (Violet)	0.03	44	Morse	45	19
	A, B, C	$X^2\Sigma^+ \rightarrow D^2\Pi_i$	0.02	Estimated	SHO	21	62
O^-, O_2^-	A, B, C	Photodetachment	Empirical	33	σ 6.5 x 10^{-18} cm^2		
C^-, H^-	B, C	Photodetachment	Empirical	33	σ 14. x 10^{-18} cm^2		
N^+	A, B, C	Isolated atomic lines	NBS	13			52
(29, 47)							(57 for pure air)
O^+	A, B, C	Isolated atomic lines	NBS	13			64
							(68 for pure air)
C^+	B, C	Isolated atomic lines	NBS	13			28
N_2^+	A	$X^2\Sigma_u^+ \rightarrow B^2\Sigma_g^+$ (1-)	0.035		Morse	37	37
++	A, B, C	None					

* A - pure air
B - air-carbon phenolic
C - air-graphite

TABLE A-2

ELEMENTAL MASS FRACTIONS

	N	O	C	H
Air - thermodynamic and transport properties	0.7900	0.2100	0.0	0.0
Air - radiative properties	0.7875	0.2095	0.003	0.0
Carbon phenolic	0.0086	0.0491	0.9207	0.0216
Graphite	0.0	0.0	1.0	0.0

TABLE A-3

CARBON PHENOLIC-AIR k_ω REFERENCE CASE CONDITIONS

T = 16,000°K P = 1 atmosphere

Species	Mole Fraction
N	7.774×10^{-2}
O	7.774×10^{-2}
C	7.774×10^{-2}
H	7.774×10^{-2}
C_2	7.774×10^{-4}
H_2	2.221×10^{-2}
N_2	2.221×10^{-2}
O_2	2.221×10^{-2}
CO	7.774×10^{-2}
NO	7.774×10^{-3}
CN	7.774×10^{-2}
C_2H_2	7.774×10^{-4}
CH	7.774×10^{-2}
C_3, C_4, C_5	2.221×10^{-3}
N^+	7.774×10^{-2}
O^+	7.774×10^{-2}
C^+	2.221×10^{-1}

Appendix B

FLOW FIELD AND RADIATIVE TRANSPORT FOR THE ENTRY CONDITIONS STUDIED

In this appendix a tabular summary of results for all cases considered in this study is presented. Also figures showing flow field and wall radiation results for each case are included. Table B-1 lists, for each case studied, the case description (entry conditions, nose radius, injectant rate and properties, shock temperature, and wall temperature) and the basic results (shock detachment distance, convective and radiative heat fluxes at the wall, and the flux forward of the shock). Figures B-1 through B-22 present the temperature, velocity, flux, and ablator concentration profiles for each case. In addition, the integral of the flux at the wall and the spectral steradiancy at the wall are shown.

The results shown for case numbers 1 and 5 are slightly different from the values given in Reference 2 for the same entry and blowing conditions. The differences are a result of the use of improved radiative and transport property values in this study.

TABLE B-1

SUMMARY OF RESULTS

Case Number	Altitude (ft)	Velocity (ft/sec)	Nose Radius (ft)	T_s (^oK)	T_w (^oK)	$\dot{m}$	Injectant Properties			δ (cm)	q_w^C (watts/cm^2)	q_w^R (watts/cm^2)	q_δ^R (watts/cm^2)
							Radiative	Thermodynamic	Transport				
1*	200,000	50,000	10	14,500	2000	0	--	--	--	9.85	667	5,380	9,750
2	200,000	50,000	10	14,700	2000	0	--	--	--	10.21	690	5,990	10,690
3	200,000	50,000	10	14,700	3600	0	--	--	--	10.02	462	5,990	10,600
4*	200,000	50,000	2-1/2	14,500	2000	0	--	--	--	2.79	984	3,330	6,380
5*	200,000	50,000	10	14,500	2000	0.1	Air	Air	Air	12.57	36	4,650	9,720
6	200,000	50,000	10	14,700	3600	0.1	Air	Air	Air	12.76	24	5,130	10,640
7	200,000	50,000	10	14,700	3600	0.2	Air	Air	Air	14.90	6	4,630	10,390
8	200,000	50,000	10	14,700	3600	0.2	Carbon Phenolic	Air	Air	15.44	10	3,240	9,930
9	200,000	50,000	10	14,700	3600	0.2	Carbon Phenolic	Carbon Phenolic	Air	15.48	0.4	2,670	9,330
10	200,000	50,000	10	14,700	3600	0.2	Carbon Phenolic	Carbon Phenolic	Carbon Phenolic	15.69	2	2,710	9,530
11	200,000	50,000	10	14,700	3600	0.2	Graphite	Air	Air	15.01	7	3,470	9,580
12*	200,000	50,000	2-1/2	14,500	3600	0.2	Carbon Phenolic	Air	Air	3.99	14	1,630	5,420
13*	200,000	55,000	10	16,000	2000	0	--	--	--	8.84	853	8,780	17,770
14	200,000	55,000	10	16,500	2000	0	--	--	--	8.98	977	9,260	20,040
15	200,000	55,000	10	16,500	3600	0.2	Air	Air	Air	13.92	12	7,870	19,740
16	200,000	55,000	10	16,500	3600	0.2	Carbon Phenolic	Air	Air	14.58	49	5,910	17,850
17*	200,000	45,000	10	13,500	2000	0	--	--	--	10.88	456	3,300	5,580
18*	200,000	45,000	10	13,500	3600	0.2	Air	Air	Air	15.82	3	2,640	5,500
19*	200,000	45,000	10	13,500	3600	0.2	Carbon Phenolic	Air	Air	15.85	3	1,760	5,350
20*	200,000	45,000	2-1/2	13,500	3600	0.2	Carbon Phenolic	Air	Air	4.17	7	1,040	3,110
21*	180,000	45,000	2-1/2	14,000	3600	0.2	Carbon Phenolic	Air	Air	4.28	12	1,960	6,360
22*	180,000	40,000	2-1/2	12,600	3600	0.1	Carbon Phenolic	Air	Air	3.86	14	1,060	2,540

*Precursor effects not included for these cases.

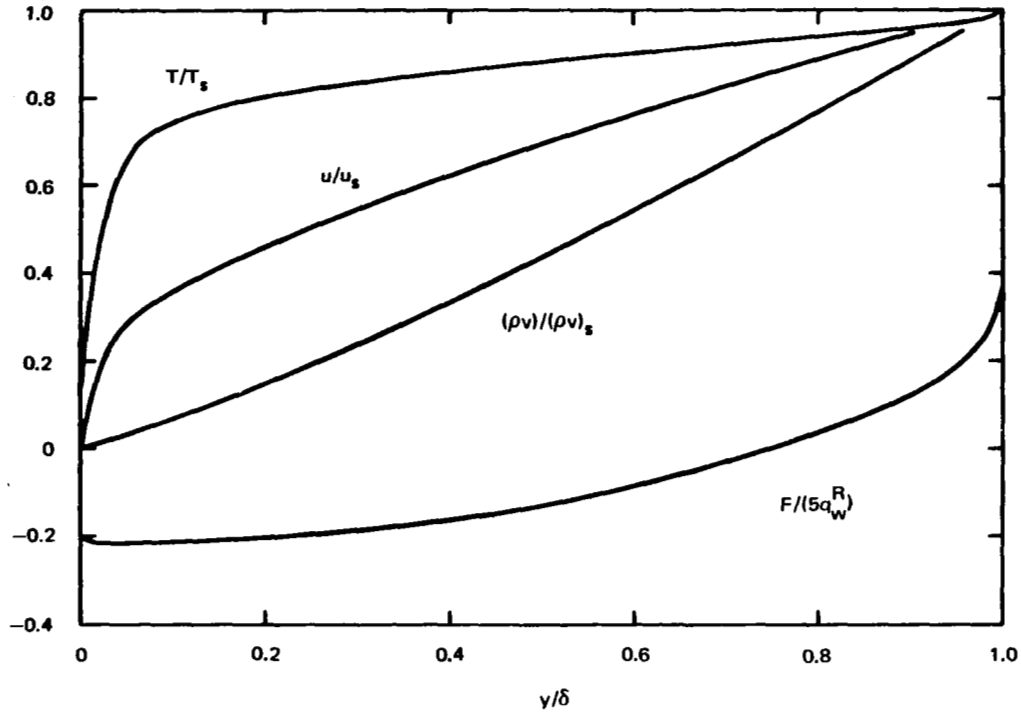

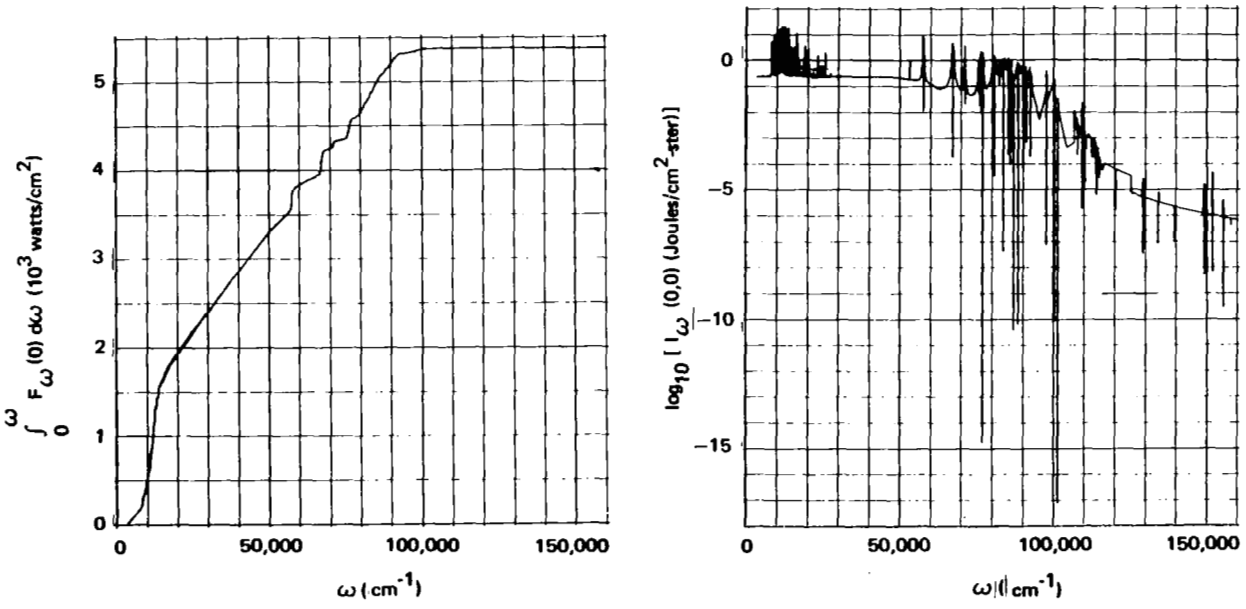

Figure B-1. Case Number 1

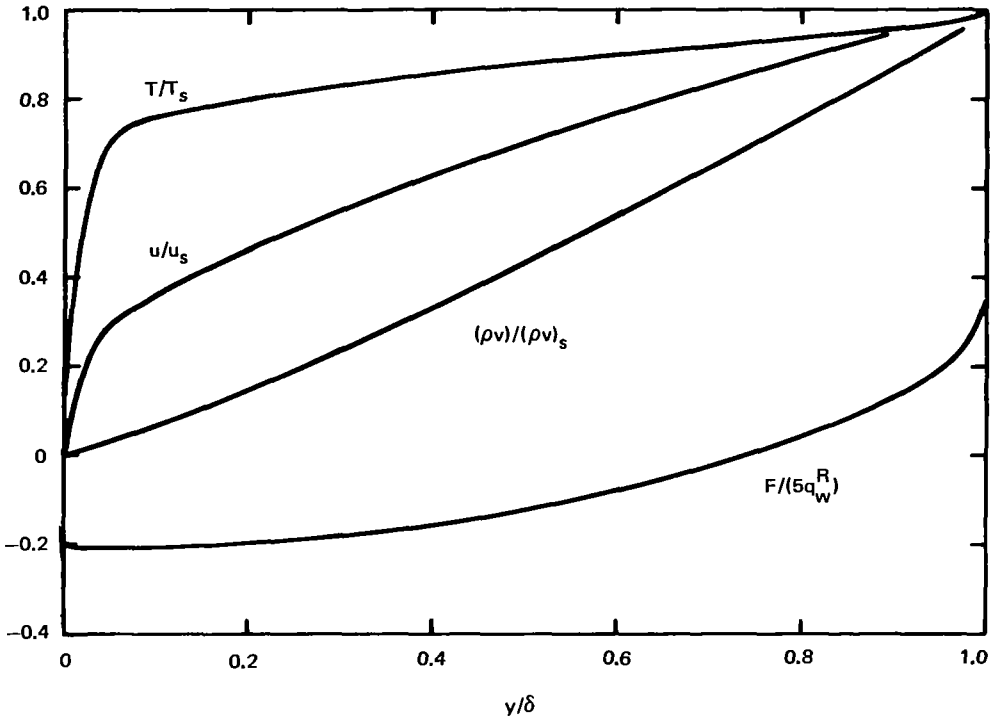

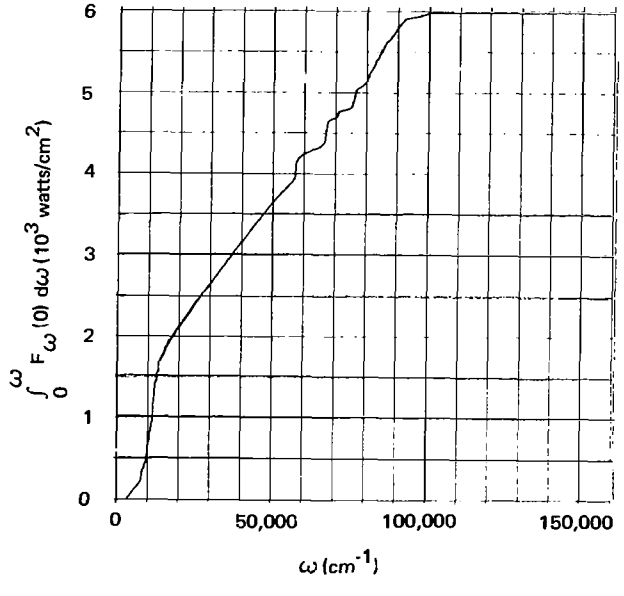

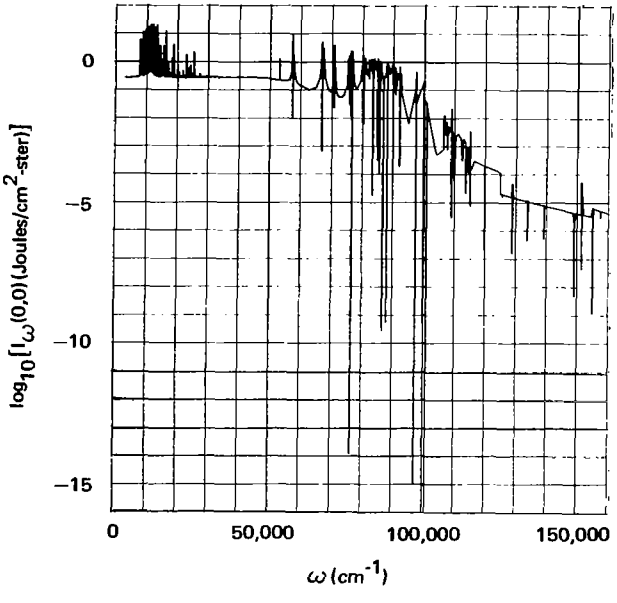

Figure B-2. Case Number 2

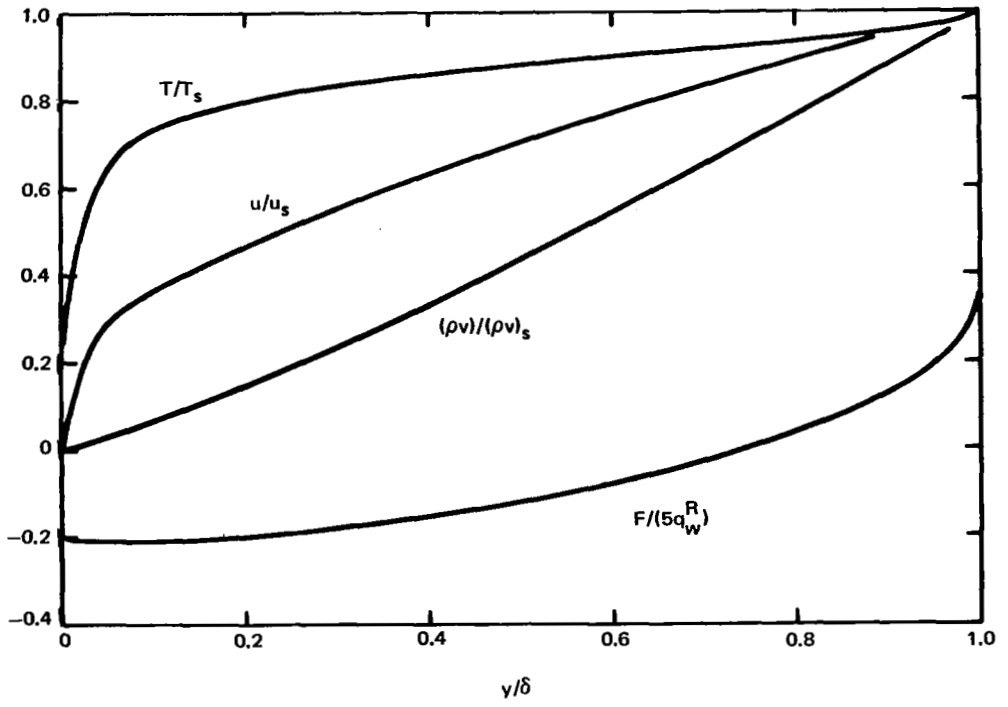

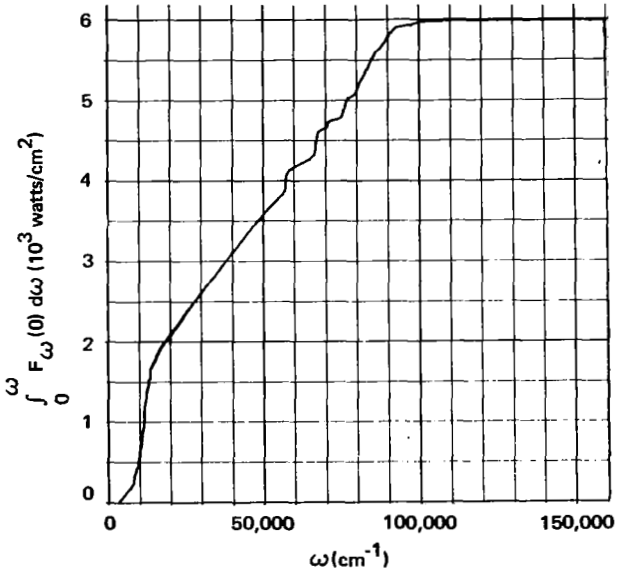

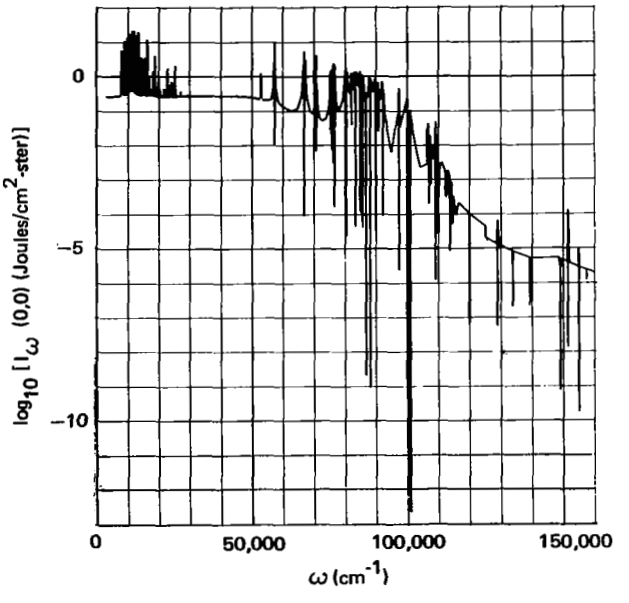

Figure B-3. Case Number 3

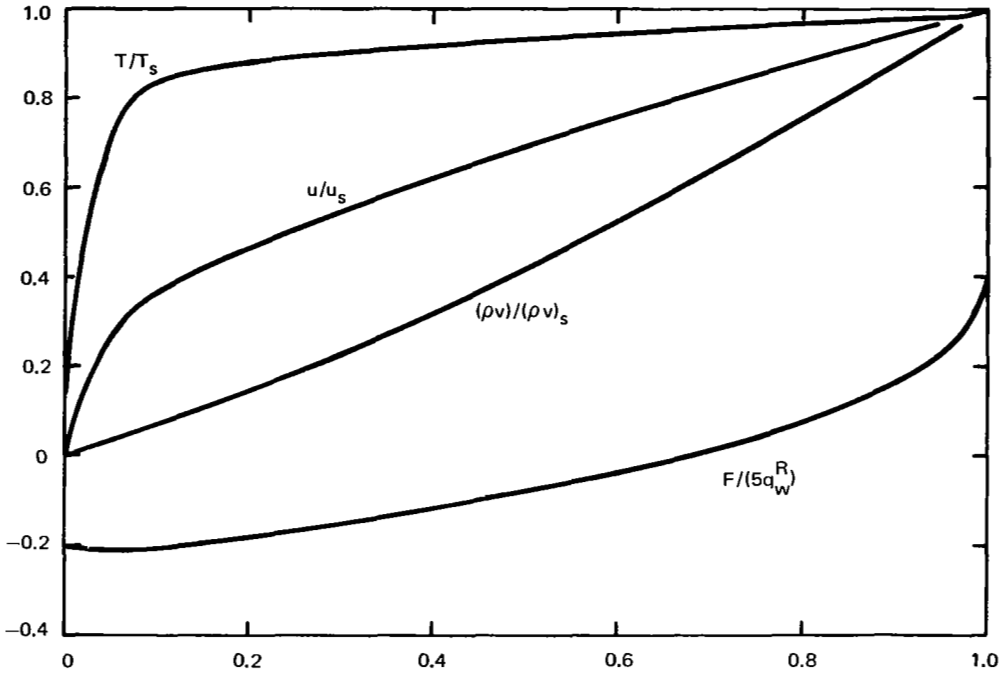

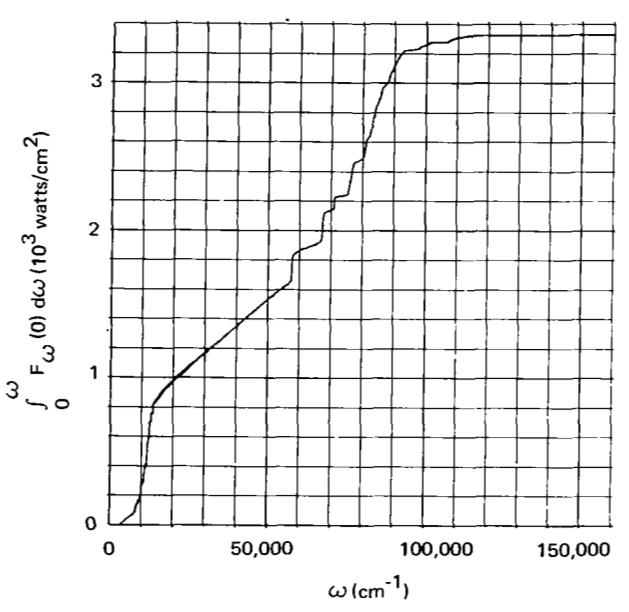

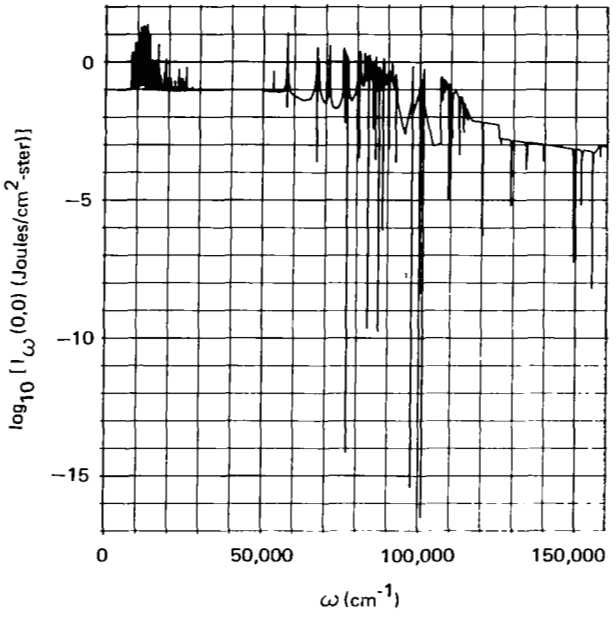

Figure B-4. Case Number 4

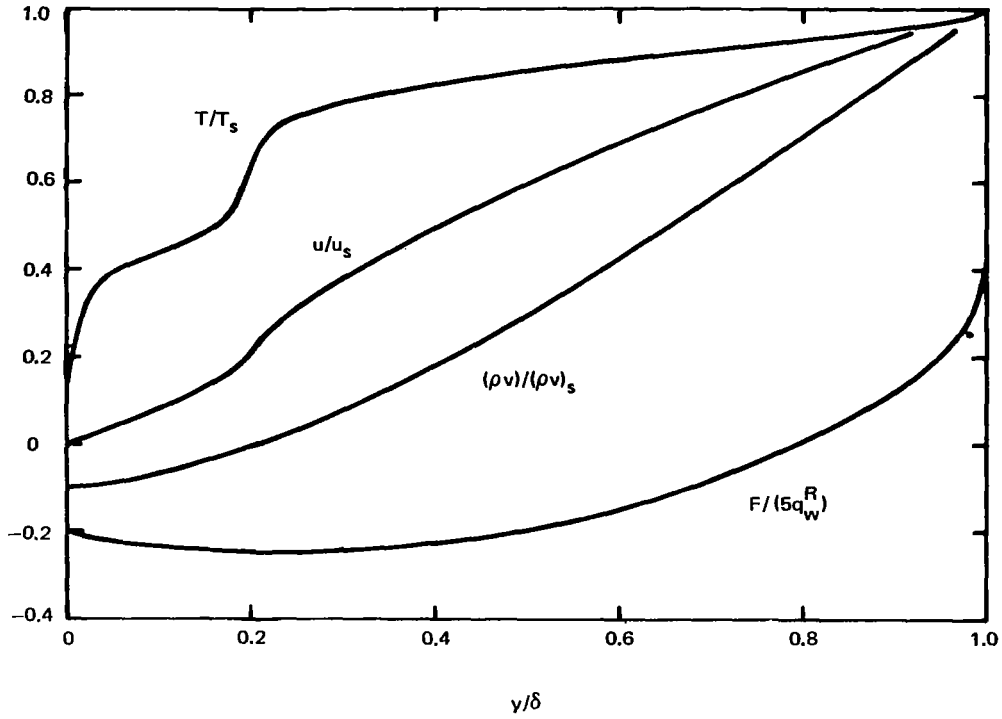

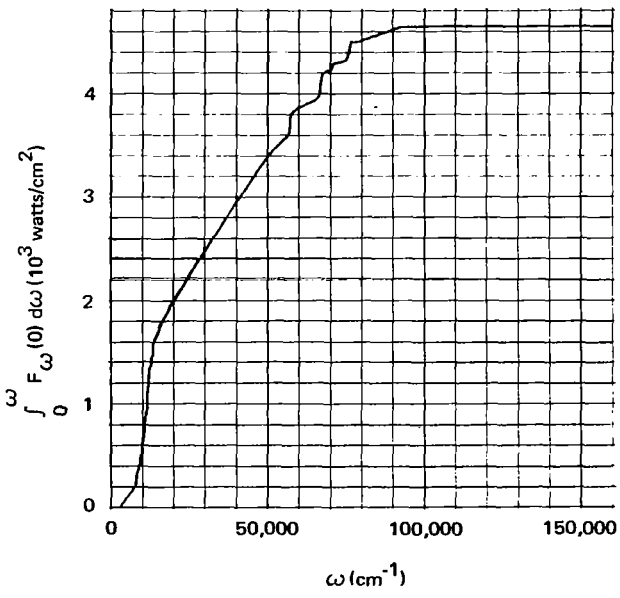

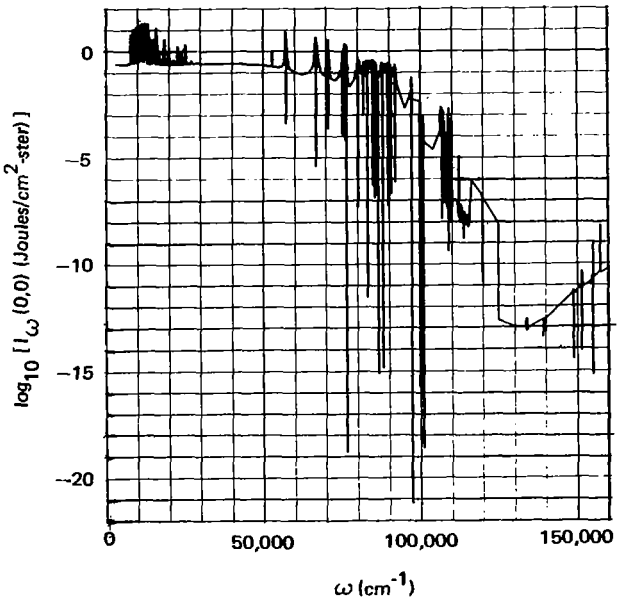

Figure B-5. Case Number 5

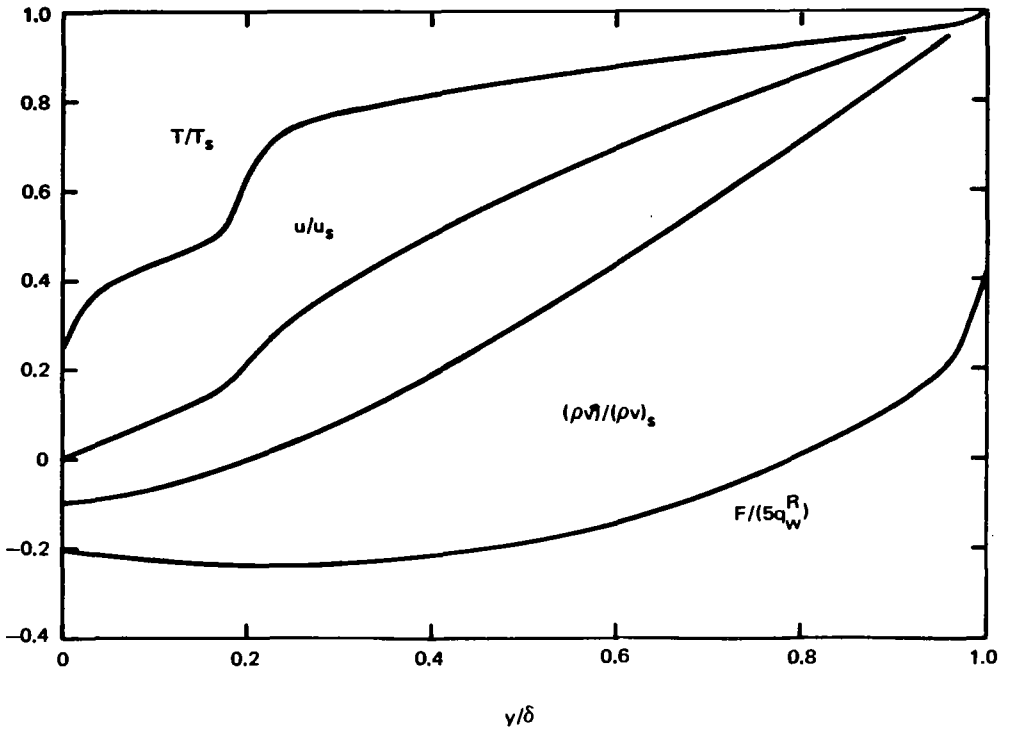

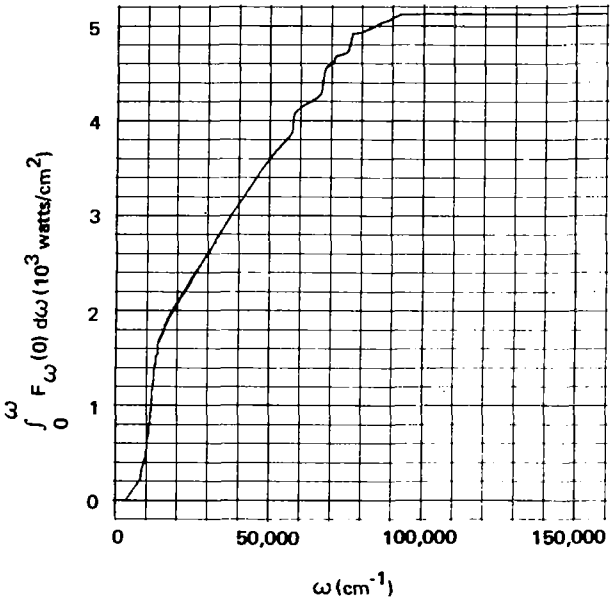

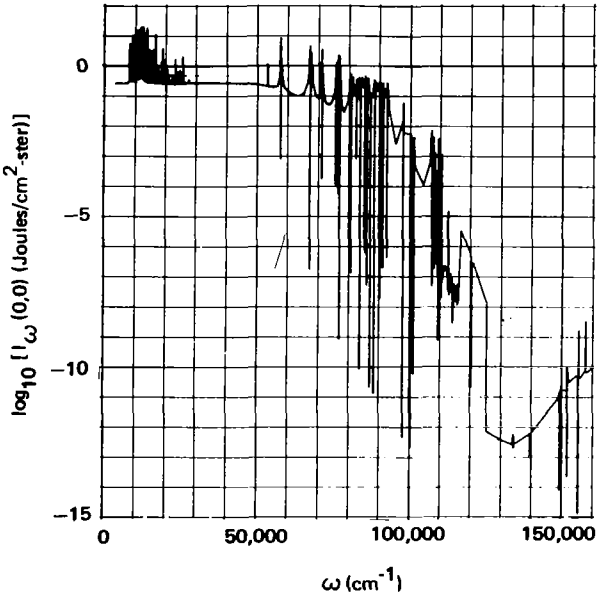

Figure B-6. Case Number 6

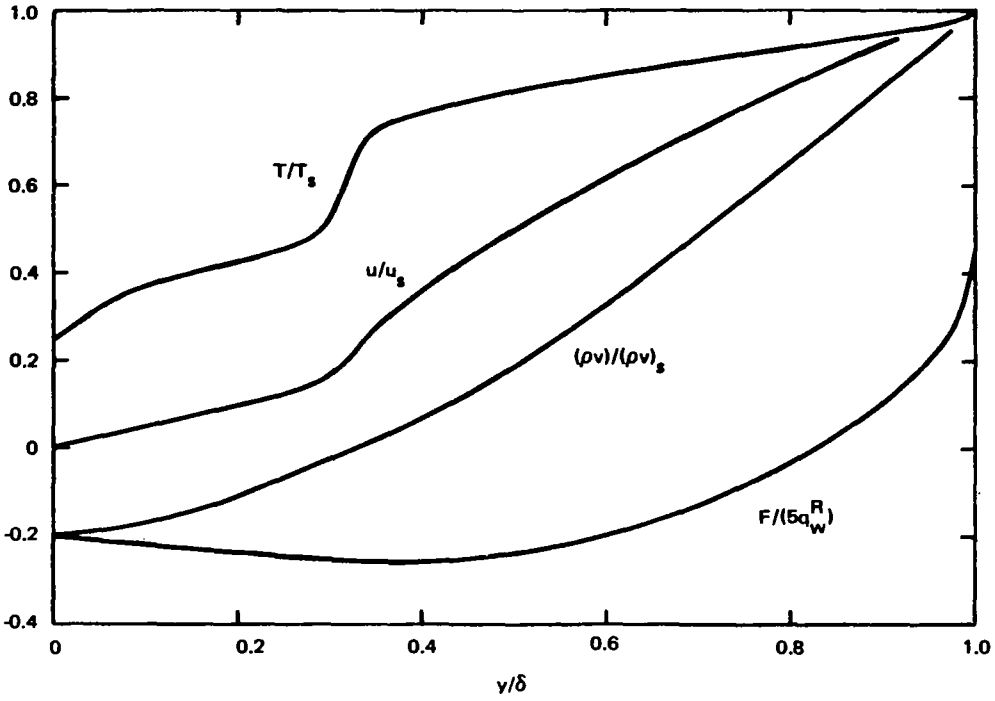

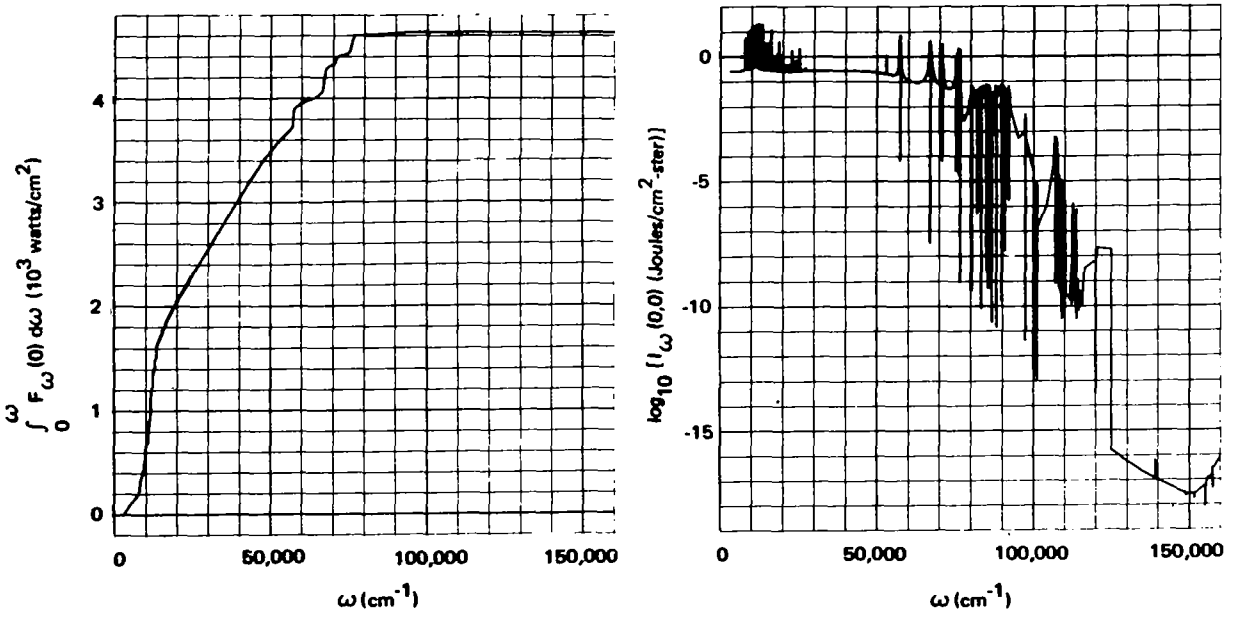

Figure B-7. Case Number 7

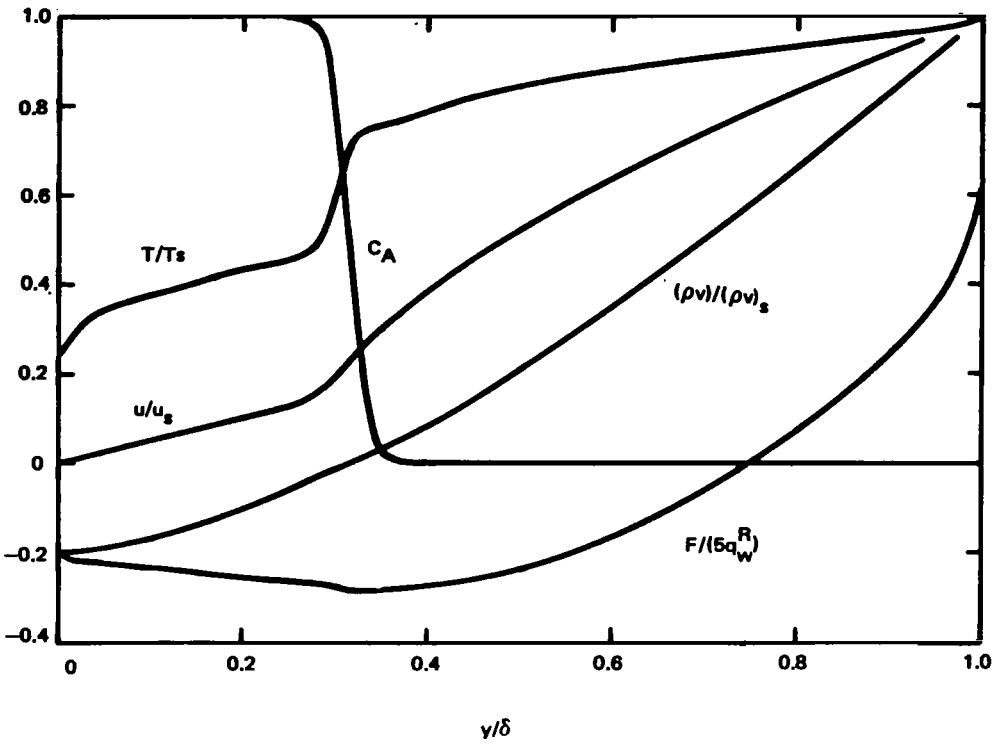

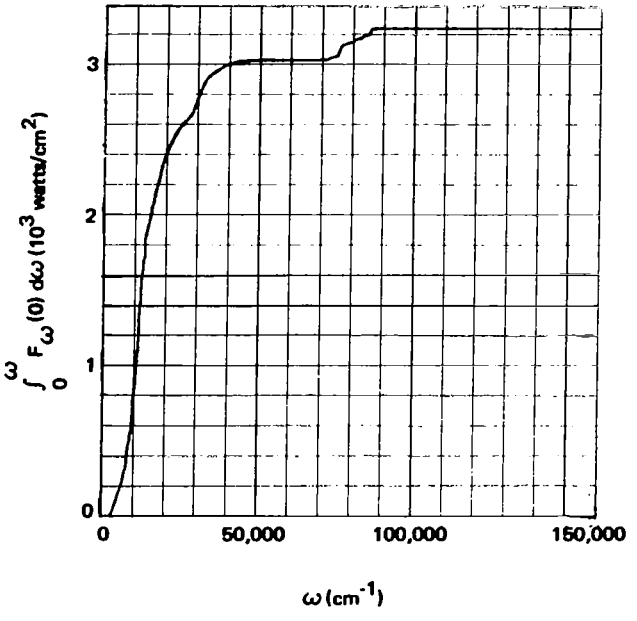

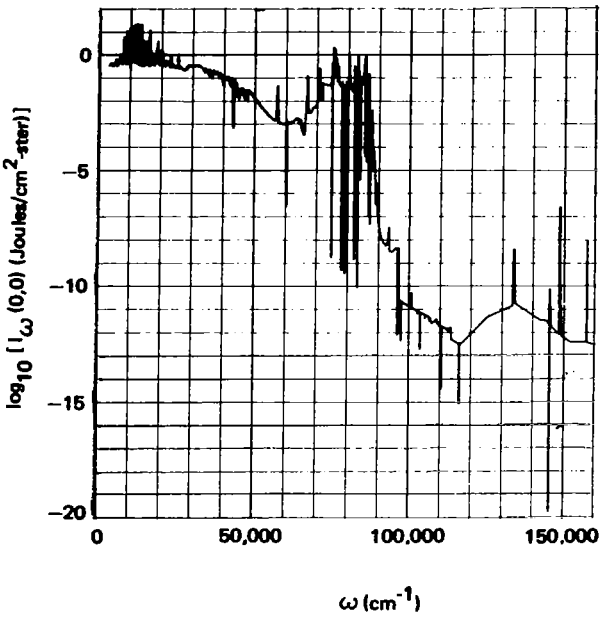

Figure B-8. Case Number 8

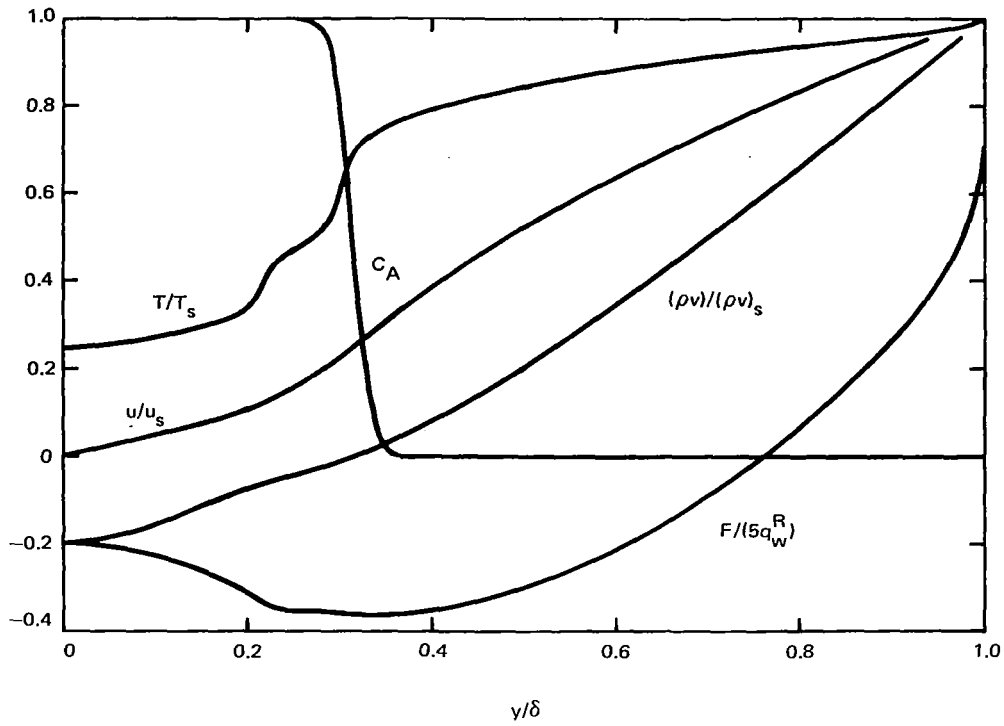

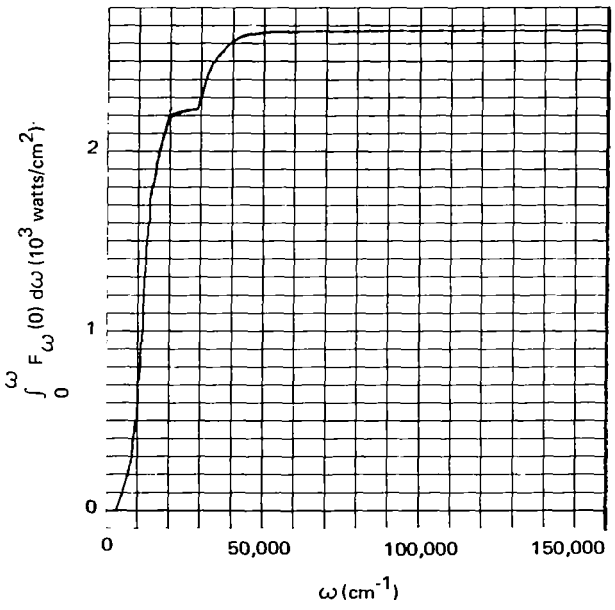

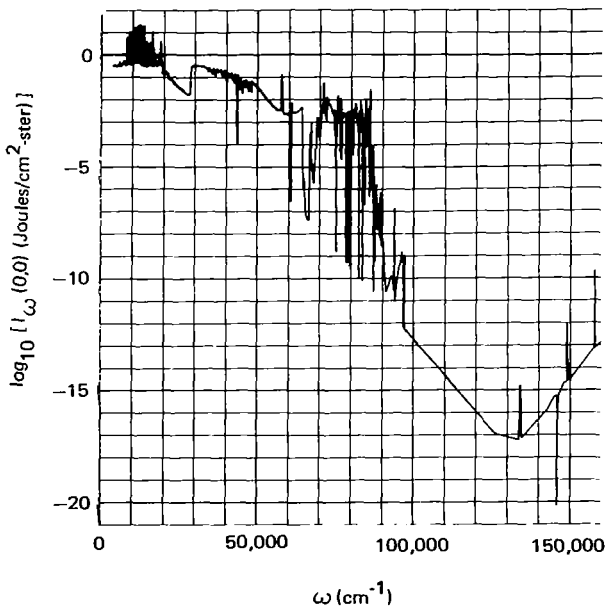

Figure B-9. Case Number 9

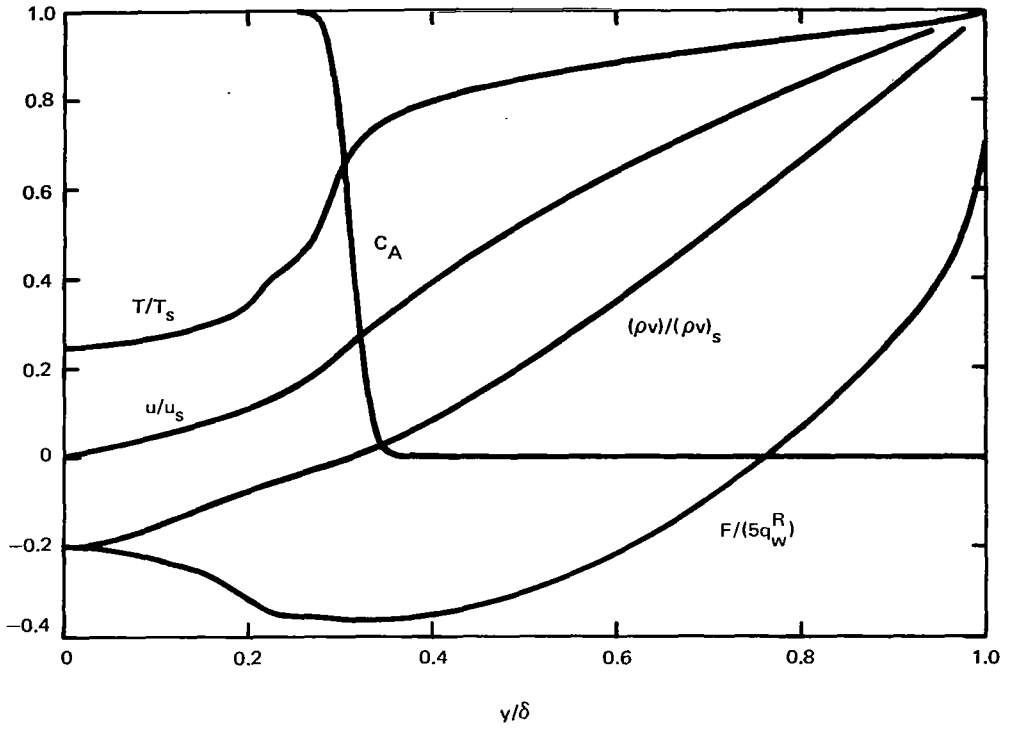

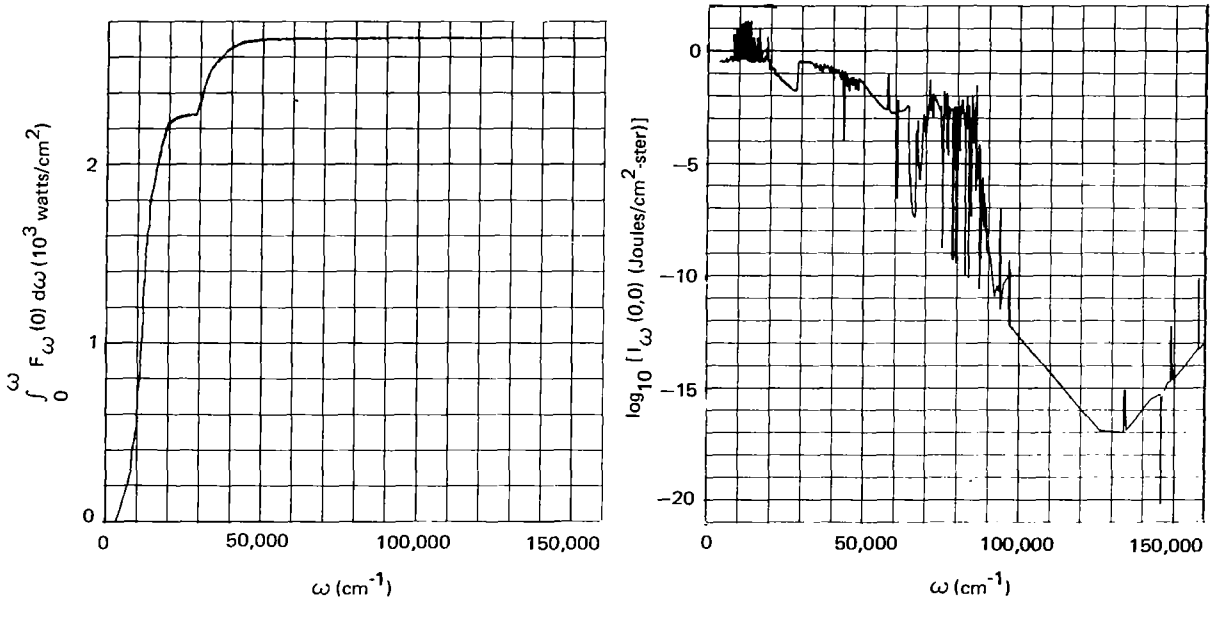

Figure B-10. Case Number 10

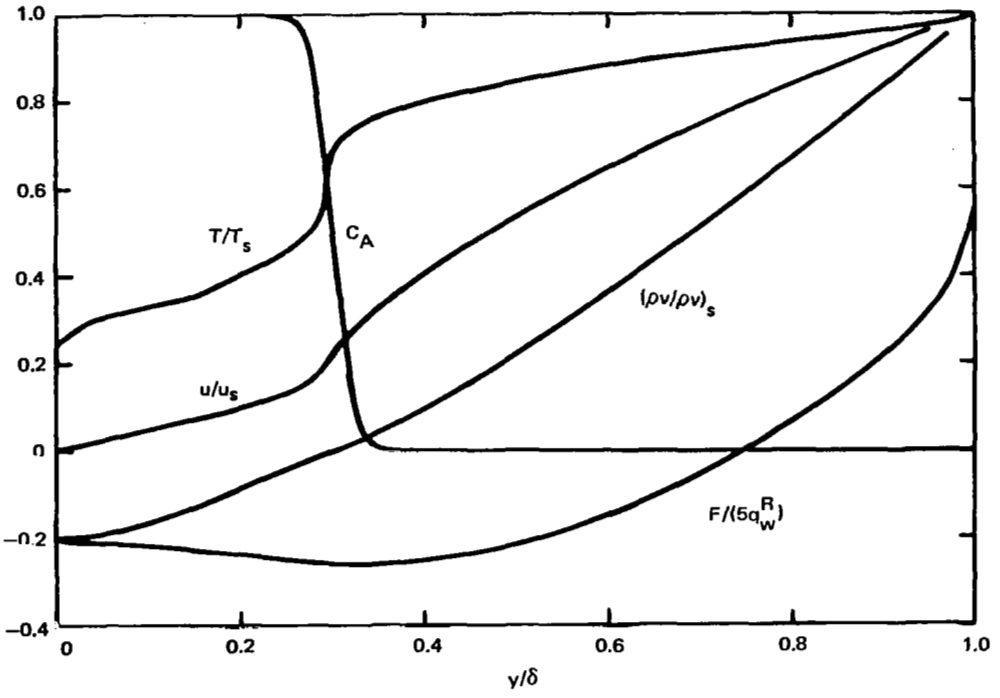

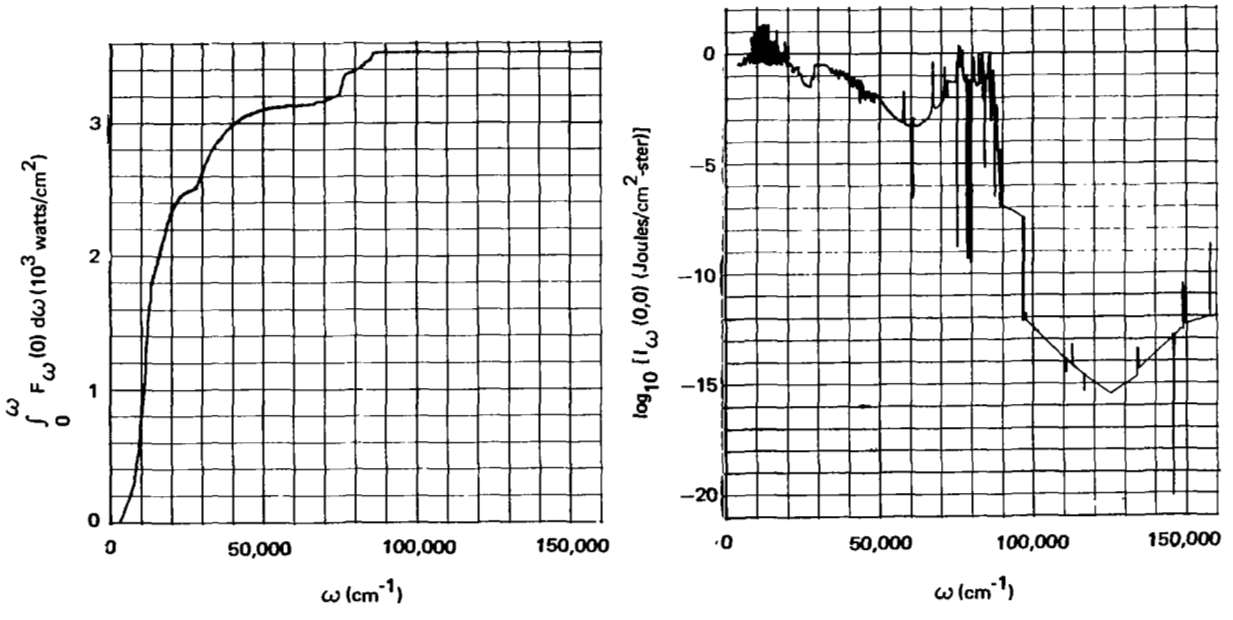

Figure B-11. Case Number 11

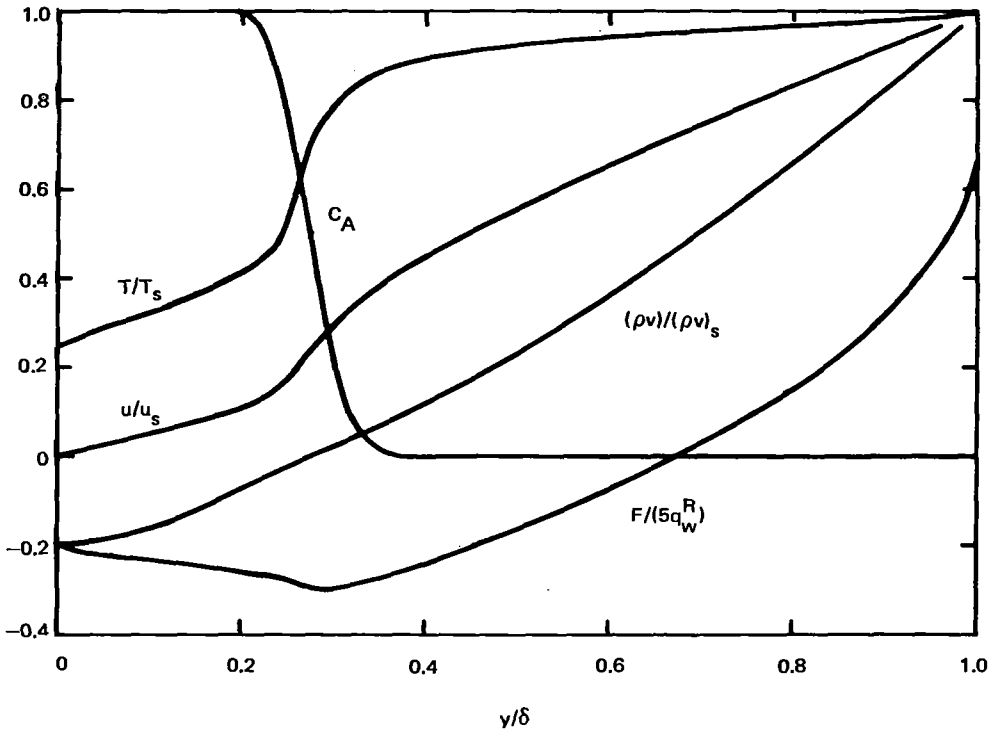

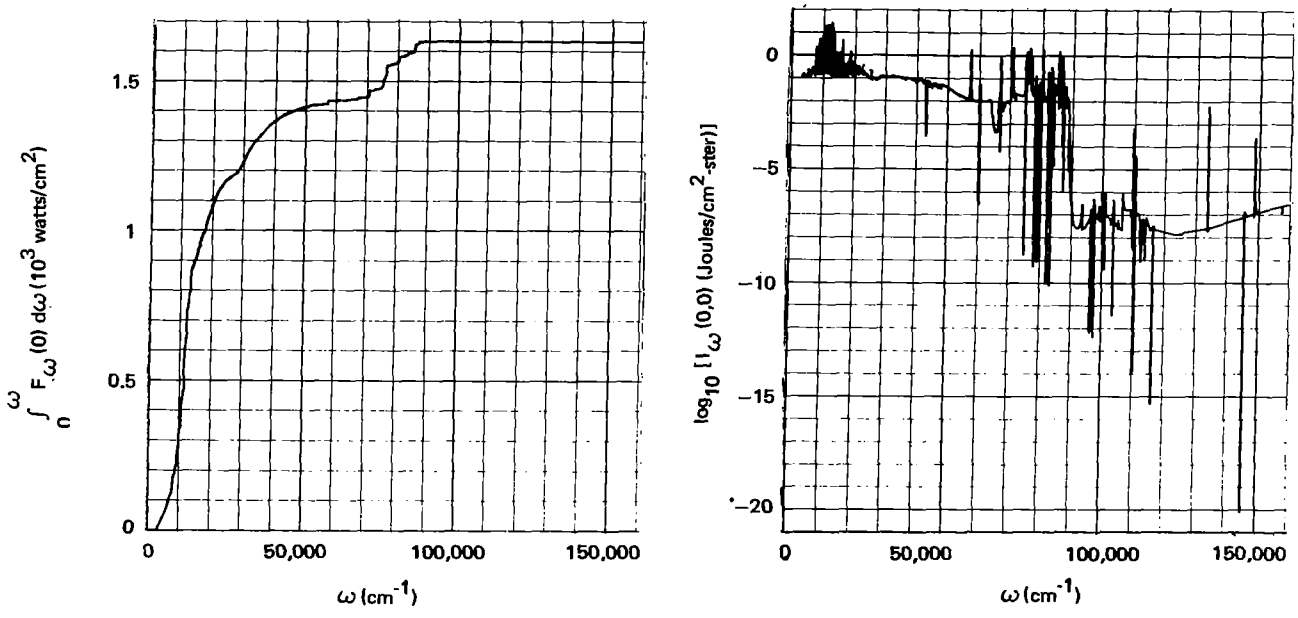

Figure B-12. Case Number 12

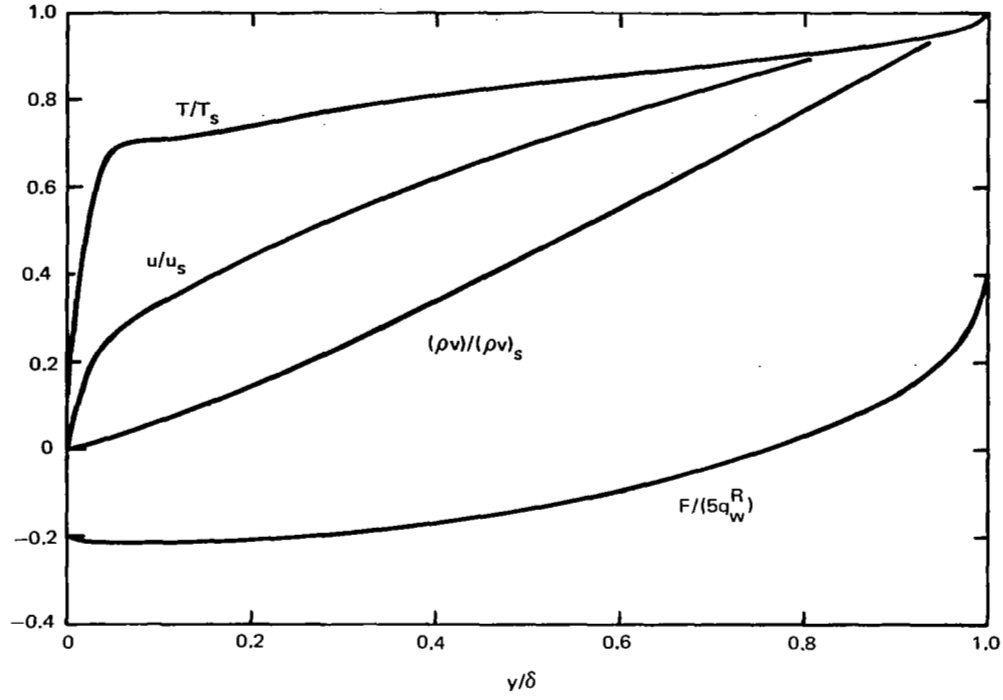

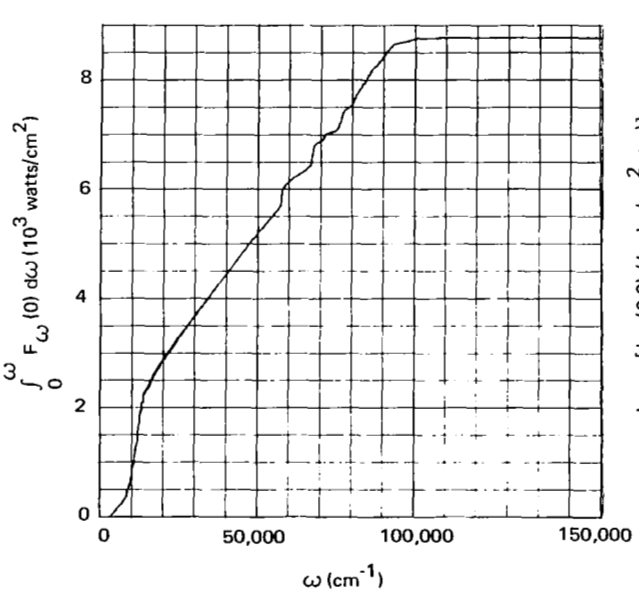

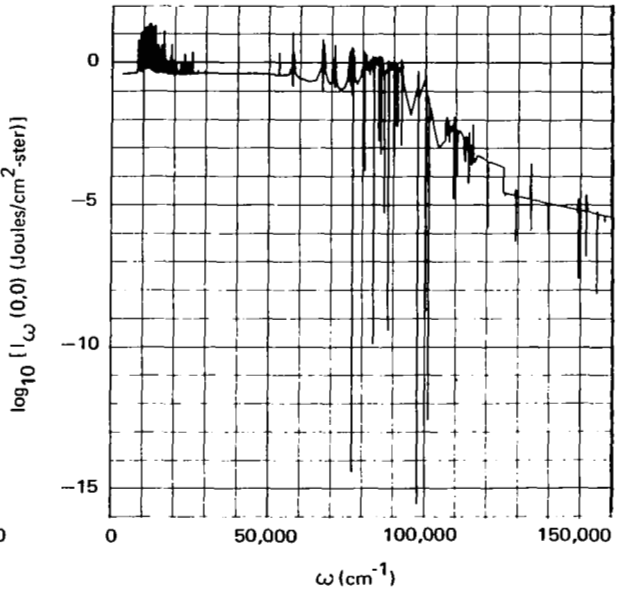

Figure B-13. Case Number 13

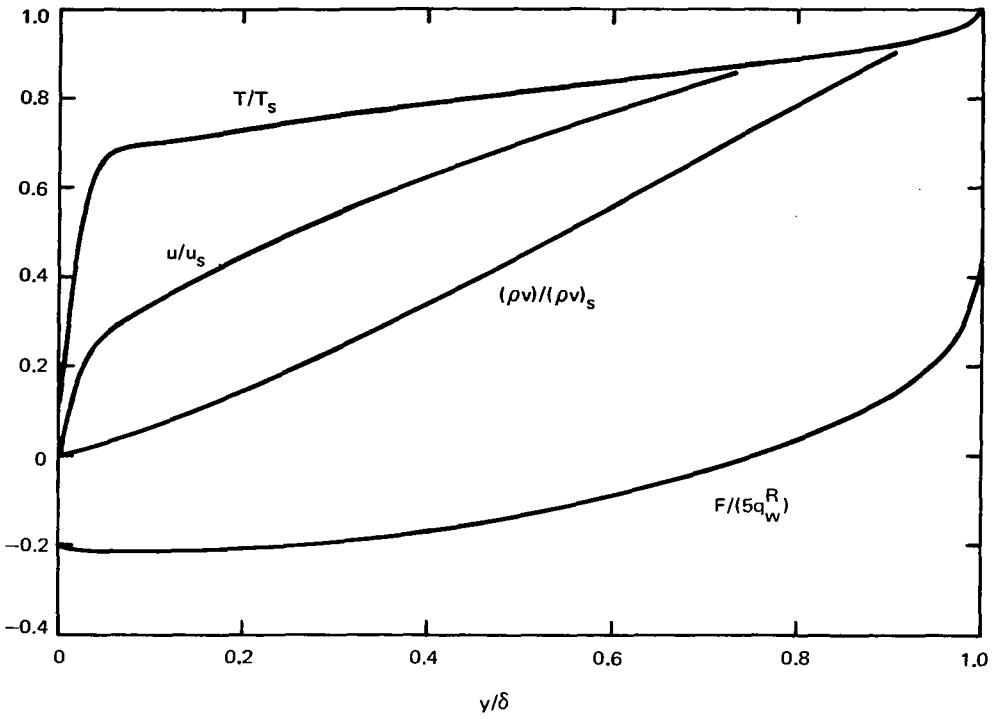

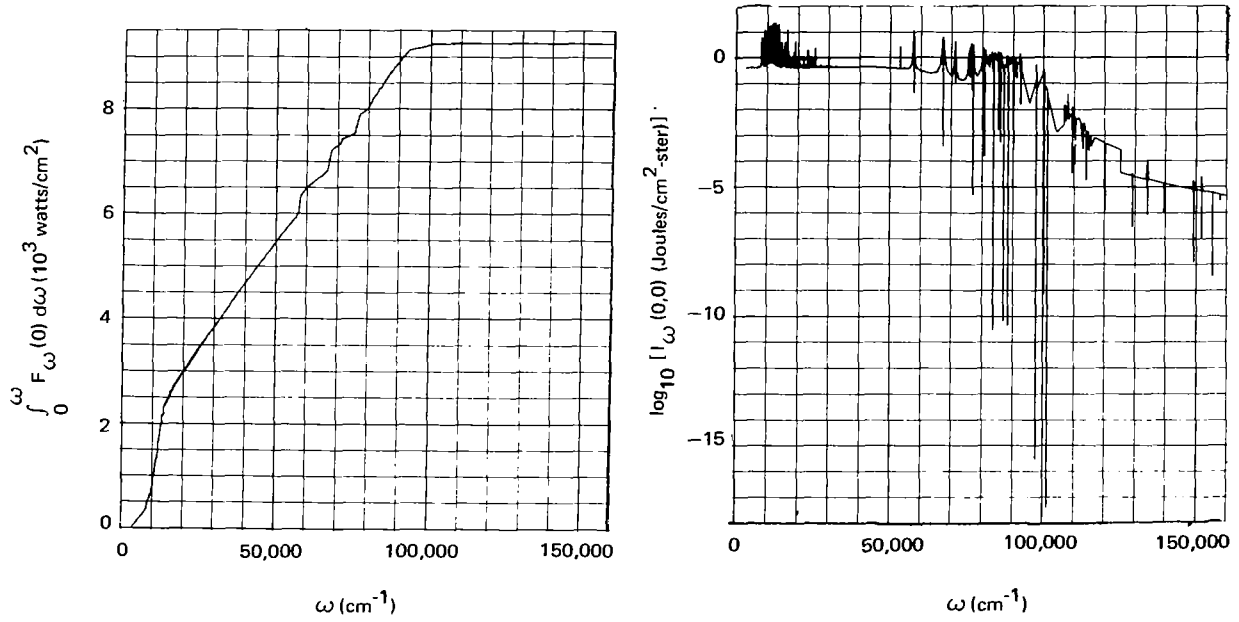

Figure B-14. Case Number 14

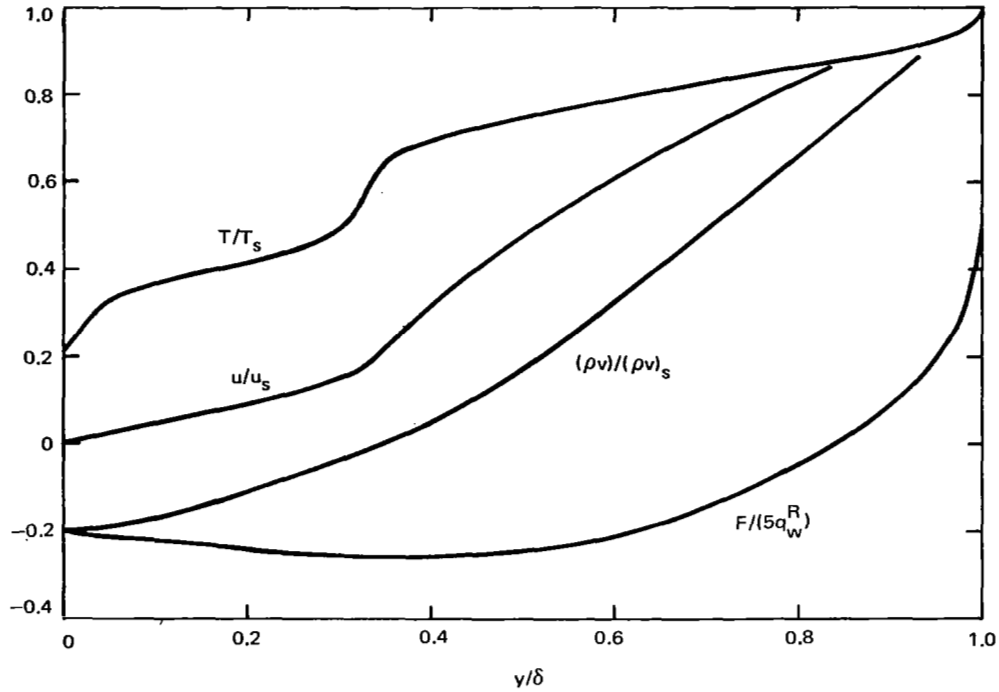

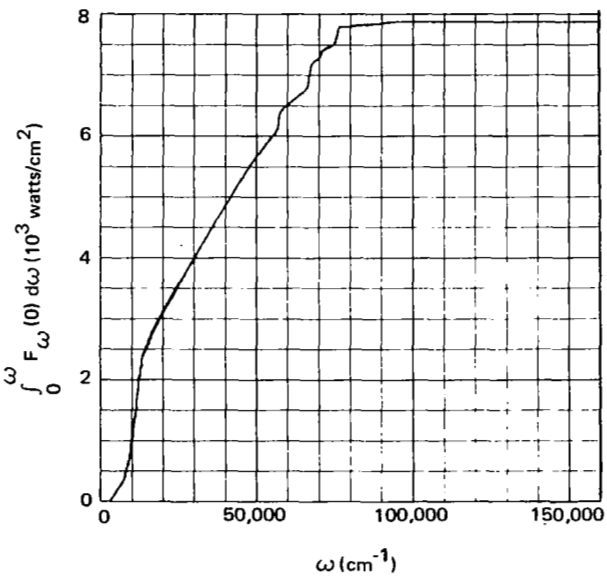

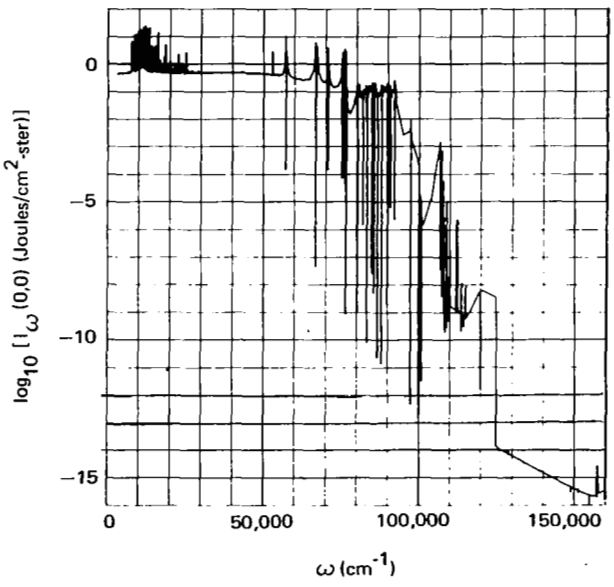

Figure B-15. Case Number 15

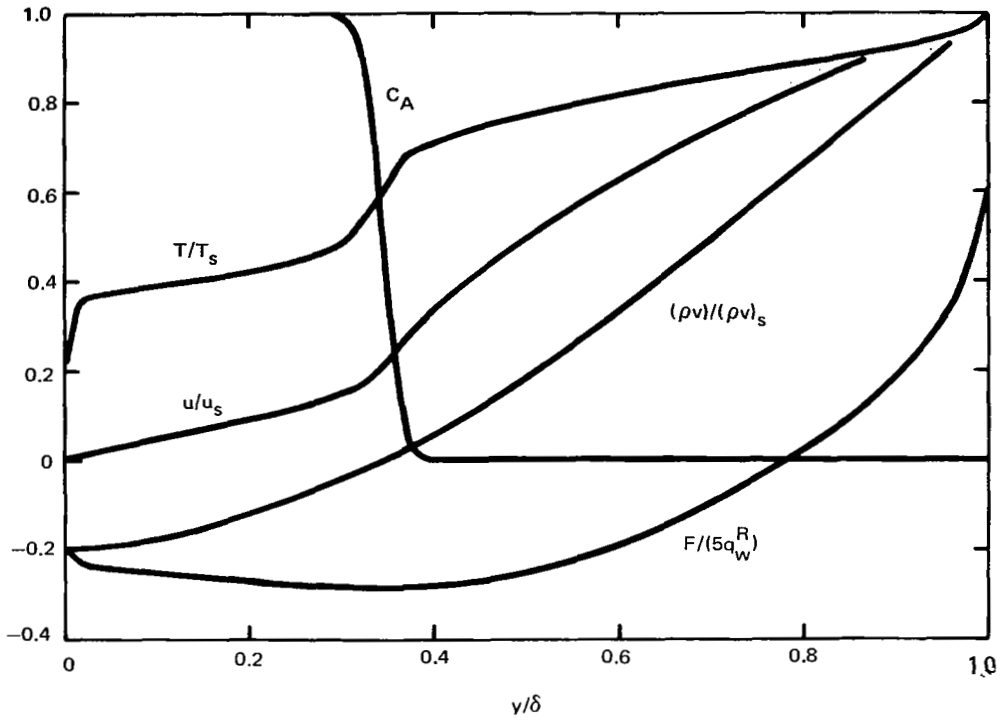

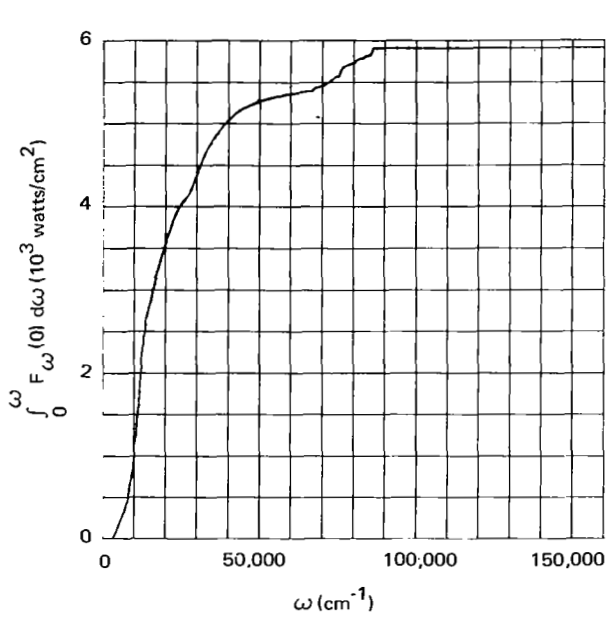

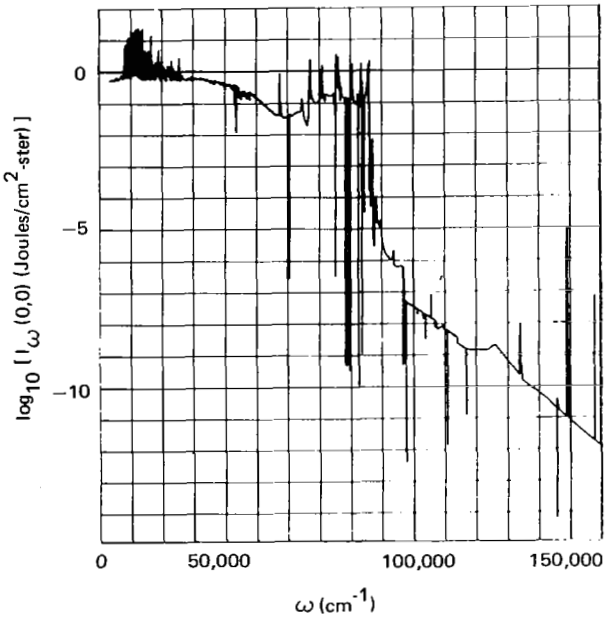

Figure B-16. Case Number 16

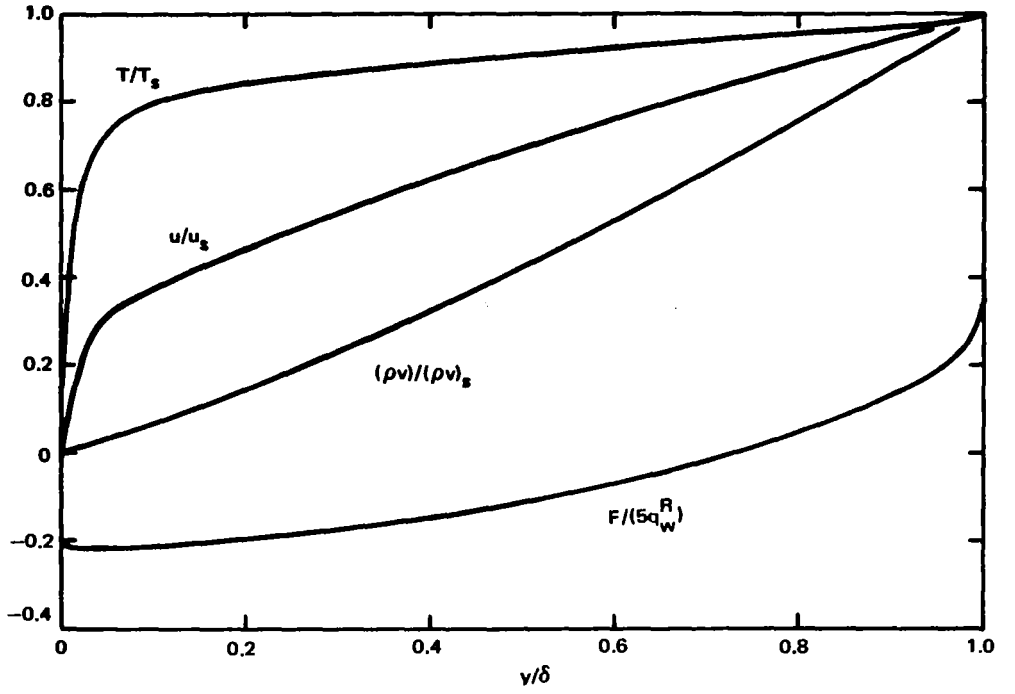

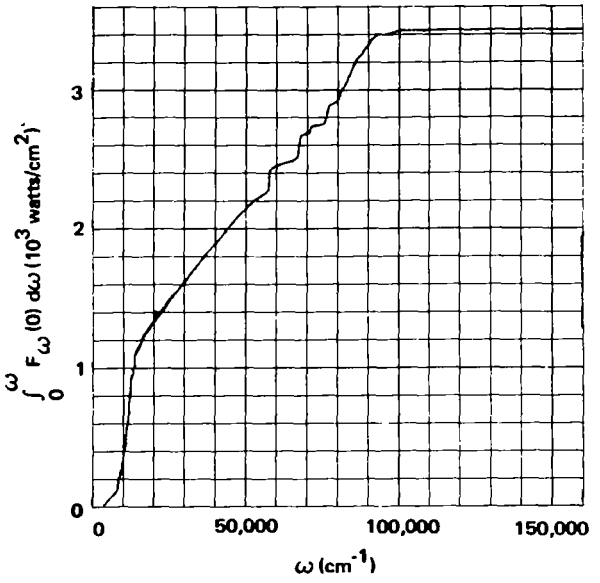

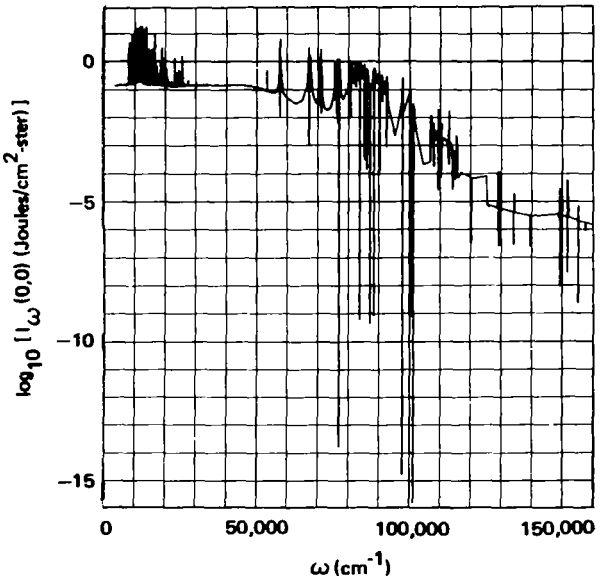

Figure B-17. Case Number 17

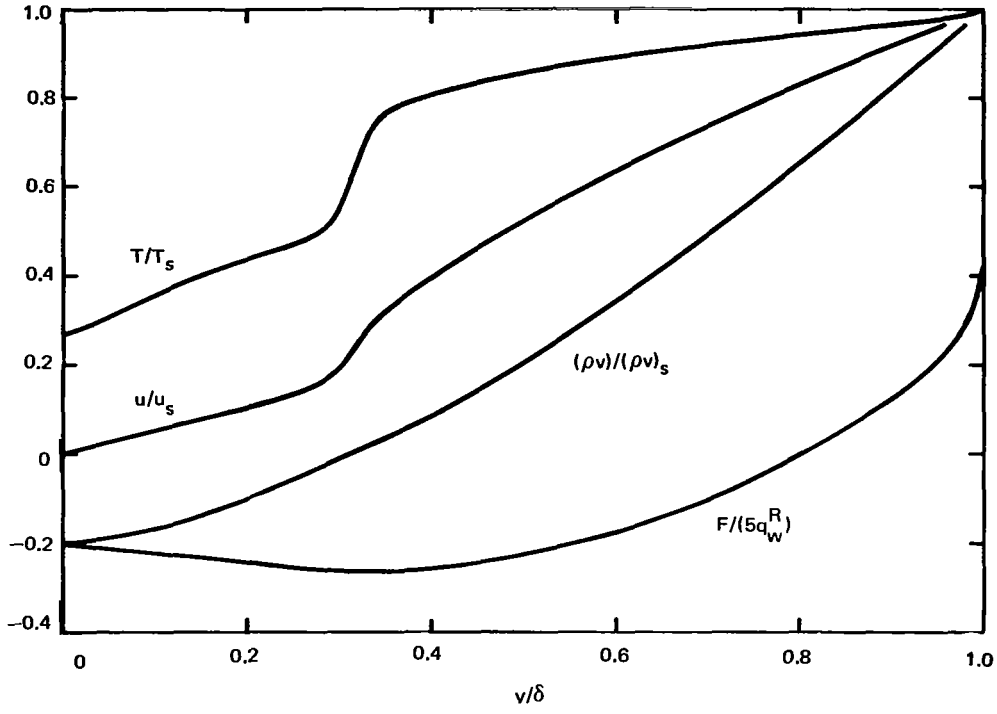

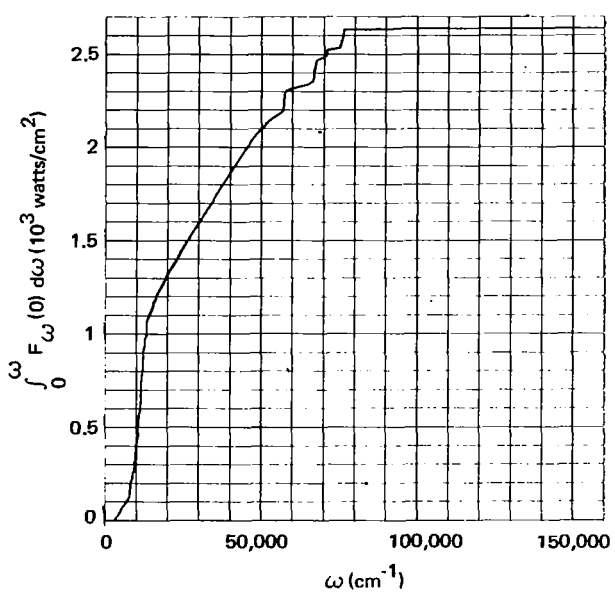

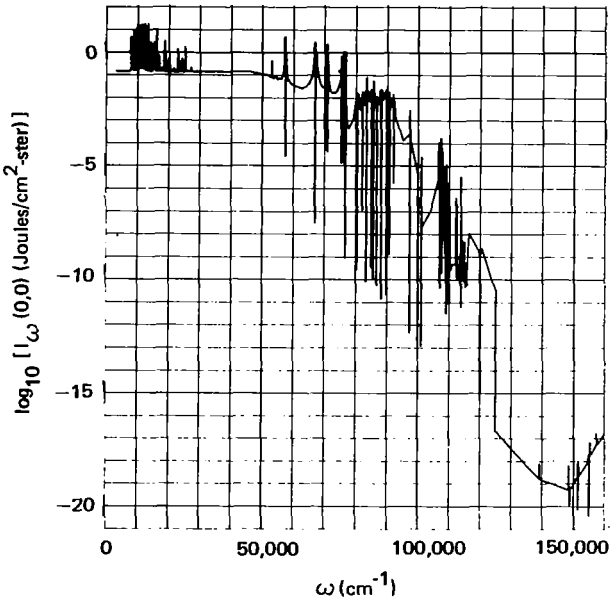

Figure B-18. Case Number 18

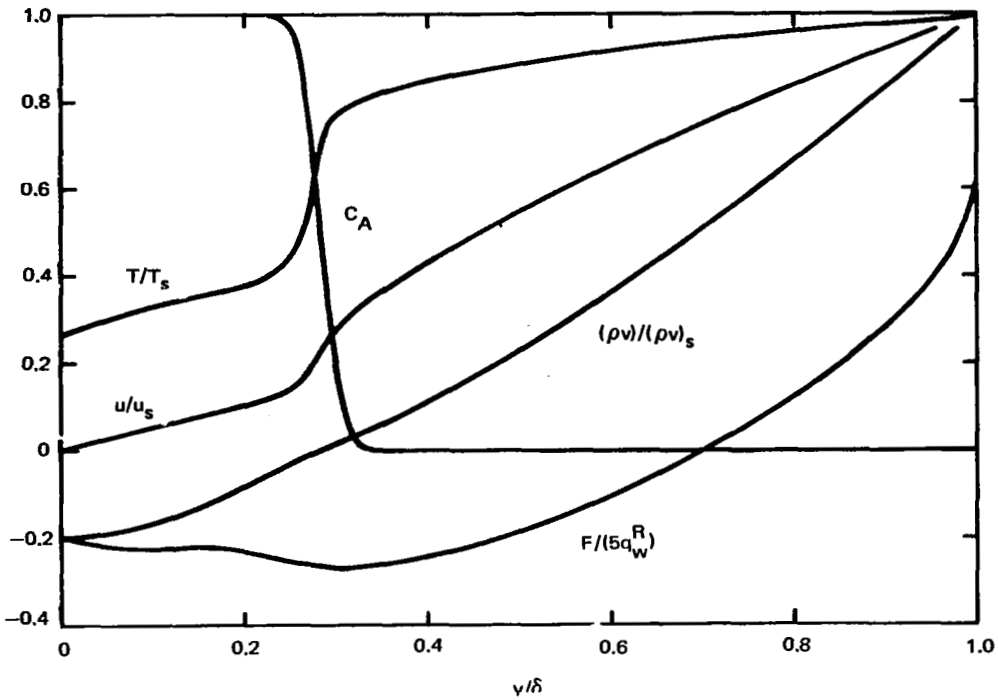

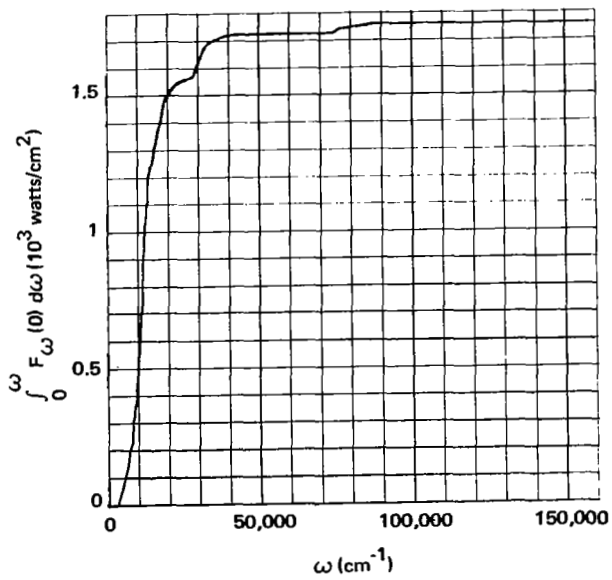

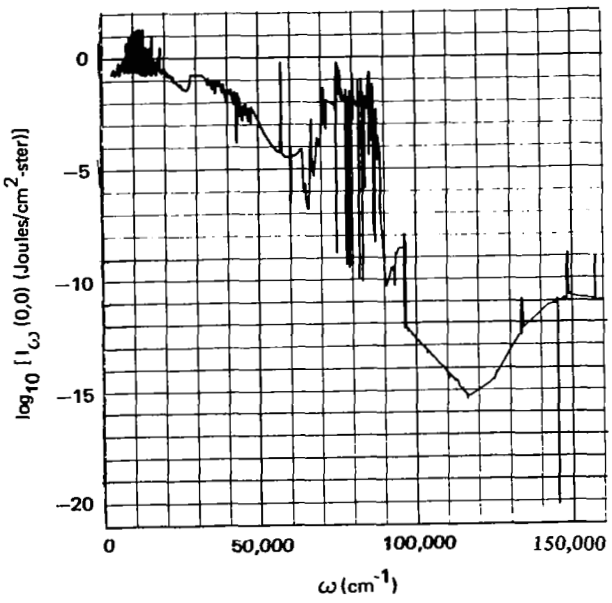

Figure B-19. Case Number 19

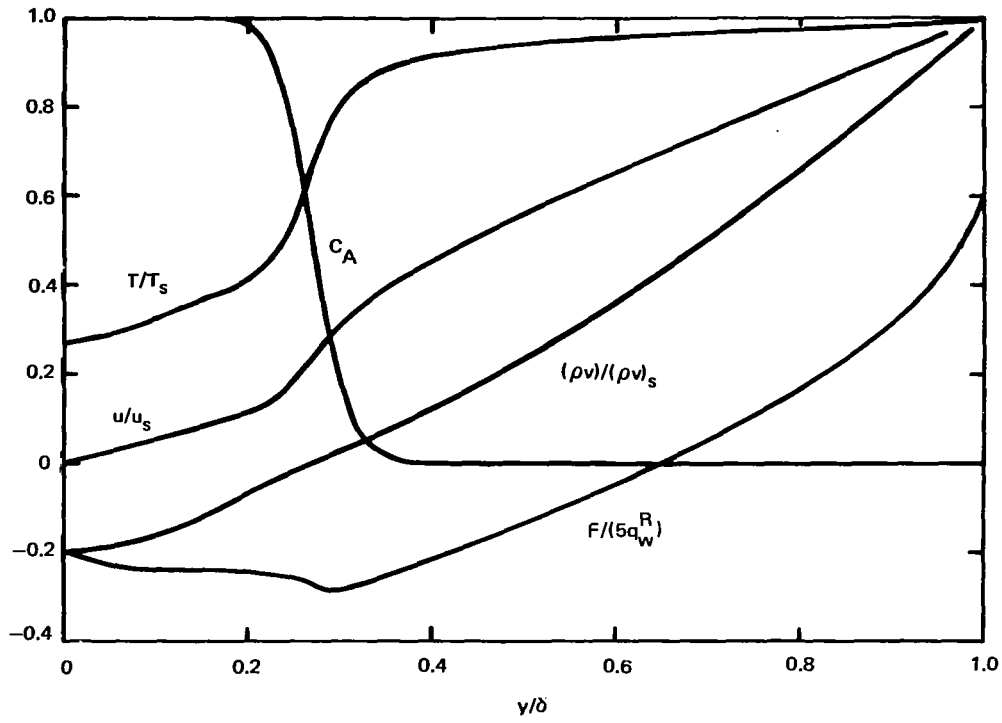

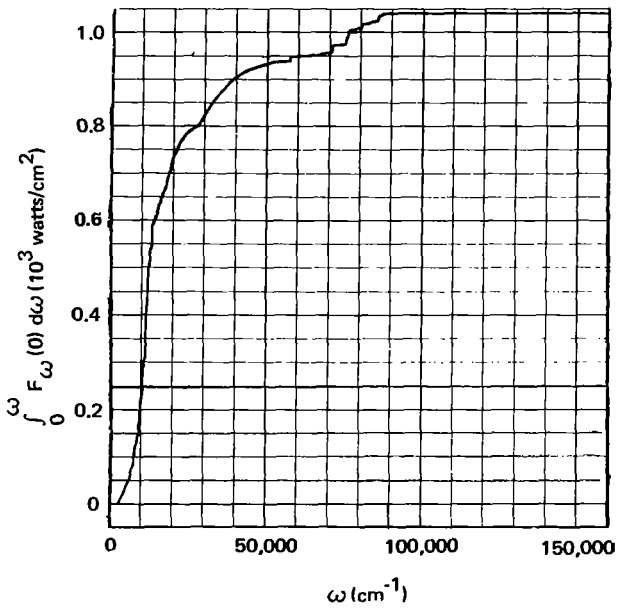

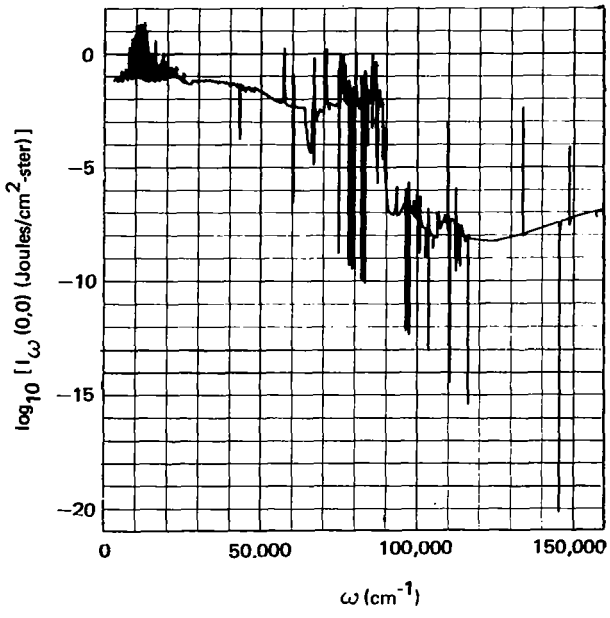

Figure B-20. Case Number 20

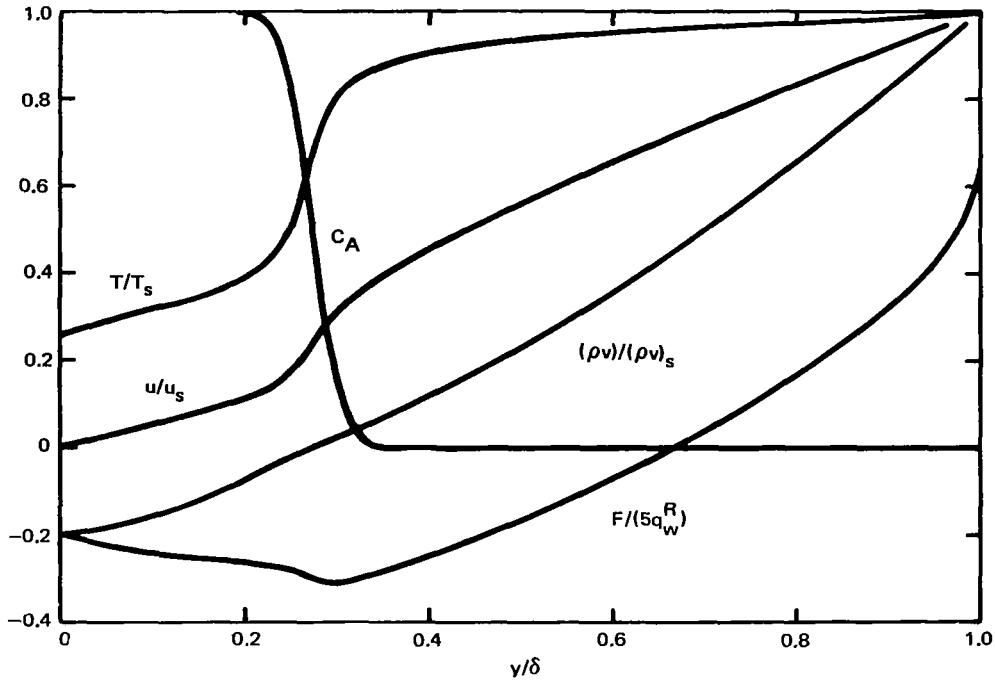

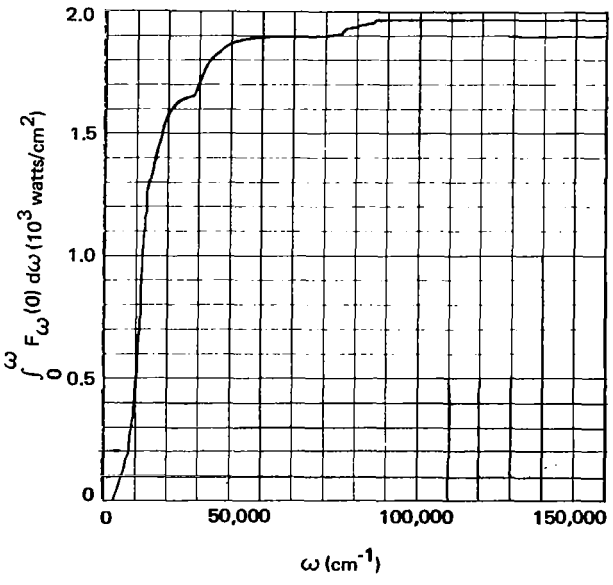

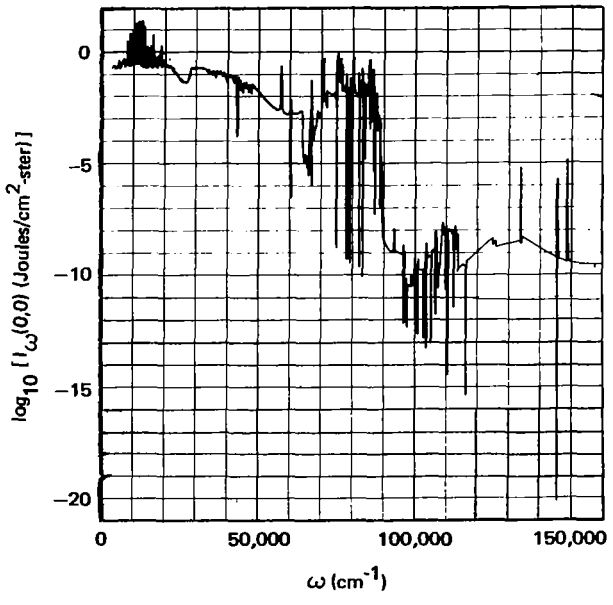

Figure B-21. Case Number 21

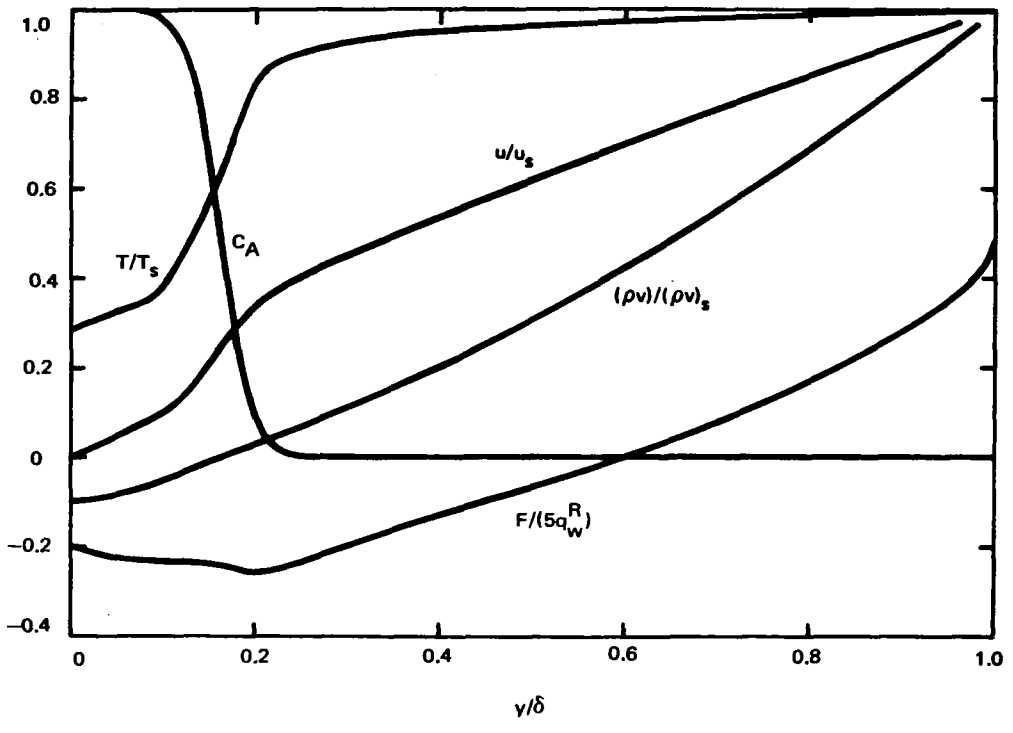

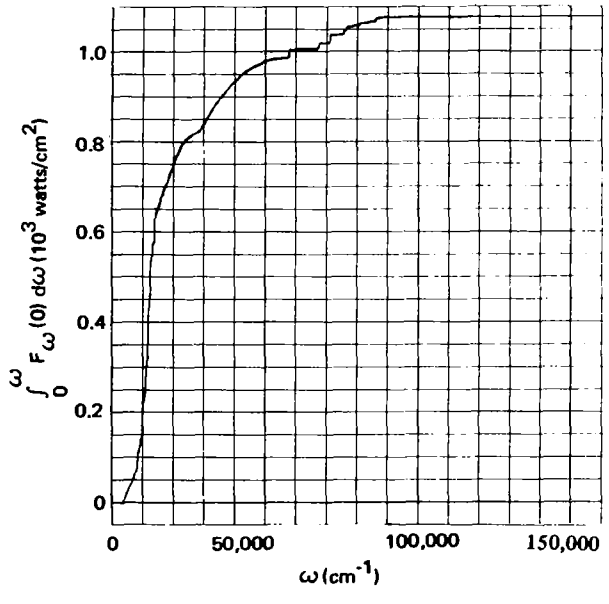

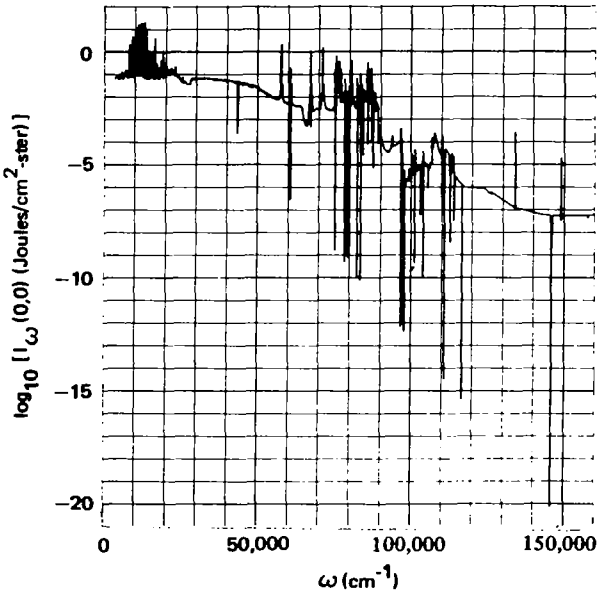

Figure B-22. Case Number 22

REFERENCES

1. Wick, B. H.: Radiative Heating of Vehicles Entering the Earth's Atmosphere. Fluid Mechanics Panel of AGARD, NATO, Brussels, Belgium, Apr. 3-6, 1962.

2. Rigdon, W. S.; Dirling, R. B., Jr.; and Thomas, M.: Radiative and Convective Heating During Atmospheric Entry. NASA Contractor Report, CR-1170, Sep. 1968.

3. Wilson, K. H. and Hoshizaki, H.: Effect of Ablation Product Absorption and Line Transitions on Shock Layer Radiative Transport. NASA Contractor Report, CR-1264, Feb. 1969.

4. Page, W.A.: Compton, D. L.; Borucki, W. J.; Ciffone, D.L.; and Cooper, D.M.: Radiative Transport in Inviscid Nonadiabatic Stagnation-Region Shock Layers. AIAA Paper No. 68-784, Jun. 1968

5. Anderson, J. D. Jr.: Non-Gray Radiative Transfer Effects on the Radiating Stagnation Region Shock Layer and Stagnation Point Heat Transfer. NOLTR 67-104, 1967.

6. Thomas, M., Jr.: Radiation Transfer Through High-Temperature Shock Layers. Thermal Design Principles of Spacecraft and Entry Bodies, Vol. 21 of AIAA Progress in Astronautics and Aeronautics, in Press.

7. Dirling, R. B., Jr.; Rigdon, W. S.; and Thomas, M.: Stagnation-Point Heating Including Spectral Radiative Transfer. Proceedings of the 1967 Heat Transfer and Fluid Mechanics Institute, Stanford University Press, 1967.

8. Smith, G. L.: Radiation Induced Precursor Flow Field Ahead of a Reentering Body. presented to AIAA Fluid and Plasma Dynamics Conference, Jun. 1968.

9. Thomas, M.: Radiant Energy Transfer--Computer Program STER (H040). Douglas Report DAC-59137, McDonnell Douglas Astronautics Co. - Western Division, May 1968.

10. Thomas, M.: The Spectral Linear Absorption Coefficient of Gases - Computer Program SPECS (H189). Douglas Report DAC-59135, McDonnell Douglas Astronautics Co. - Western Division, May 1967.

11. Stewart, J. C.; and Pyatt, K. D., Jr.: Theoretical Study of Optical Properties - Photon Absorption Coefficients, Opacities, and Equations of State of Light Elements, Including the Effect of Lines. Report GA-2528, Vol. I (AFSWC-TR-61-71, Vol. 1). General Atomic Division, General Dynamics Corporation, Sep. 1961.

12. Griem, H. R.: Plasma Spectroscopy. McGraw-Hill Book Co., New York, 1964.

13. Wiese, W. L.; Smith, M. W.; and Glennon, B. M.: Atomic Transition Probabilities. Vol. I, Hydrogen through Neon. National Bureau of Standards, NSRDS - NBS 4, May 1966.

14. Elsasser, W. M.: Heat Transfer by Infrared Radiation in the Atmosphere. Harvard Meteorological Studies, No. 6, Blue Hill Meteorological Observatory, Harvard Unitiversity, Milton, Mass., 1942.

15. Menzel, D. H.; and Pekeris, C. L.; Absorption Coefficients and Hydrogen Line Intensities. Mon. Not. Roy. Astr. Soc., Vol. 96, 1935, pp. 77-111

16. Penner, S. S.; and Thomas, M.: Approximate Theoretical Calculations of Continuum Opacities. AIAA J., Vol. 2, 1964, pp. 1672-1675.

17. Sulzer, P.; and Wieland, K.: Intensitätsverteilung eines Kontinuierlichen Absorptionsspektrums. Helvetica Physica Acta, Vol. 25, 1952, pp. 653-676.

18. Jacobs, T. A.; and Giedt, R. R.: Absorption Coefficients of Cl_2 at High Temperatures. J. Quant. Spectr. Radiat. Transfer, Vol. 5, 1965, pp. 457-463.

19. Patch, R. W.; Shackleford, W. L.; and Penner, S. S.: Approximate Spectral Absorption Coefficient Calculations for Electronic Band Systems Belonging to Diatomic Molecules. J. Quant. Spectr. Radiat. Transfer, Vol. 2, 1962, pp. 263-271.

20. Herzberg, G.: Molecular Spectra and Molecular Structure, I. Spectra of Diatomic Molecules. D. Van Nostrand Company, Inc., Princeton, New Jersey, 1950.

21. Henderson, J. R.; Willett, R. A.; Muramoto, M.; and Richardson, D. C.: Tables of Harmonic Franck-Condon Overlap Integral Including Displacement of Normal Coordinates. Douglas Report SM-45807, McDonnell Douglas Astronautics Co. - Western Division, Jan. 1964.

22. Lasher, L. E.; and Wilson, K. H.: Effect of Shock Precursor Heating on Radiative Flux to Blunt Bodies. NASA Contractor Report, CR-1256, Feb. 1969.

23. Chin, J. H.: Radiation Transport for Stagnation Flows Including the Effect of Lines and Ablation Layer. AIAA Paper No. 68-644, Jun. 1968.

24. Coleman, W. D.; Hearne, L. F.; Lefferdo, J. M.; and Vojvodich, N.S.: A study of the Effects of Environmental and Ablator Performance Uncertainties on Heat Shield Requirements for Blunt and Slender Hyperbolic-Entry Bodies. AIAA Paper No. 68-154, Jan. 1968.

25. Martinez, M. R.: Description of Computer Programs H187 - Thermochemical Equilibrium Properties of Multicomponent Systems; and H289 - Statistical Thermodynamic Properties of Single Gas Species. Douglas Report DAC-59133, McDonnel Douglas Astronautics Co. - Western Division, Jun. 1967.

26. Rigdon, W. S.: A Computer Code for Calculation of Transport Properties of High-Temperature Gases. Douglas Report DAC-59134, McDonnell Douglas Astronautics Co. - Western Division, Jul.1968.

27. Clementi, Enrico: Transition Probabilities for Low-Lying Electronic States in C_2. Astrophysical J., Vol. 132, 1960, pp. 898-904.

28. Nicholls, R. W.; Fraser, P. A.; and Jarmain, W. R.; Transition Probability Parameters of Molecular Spectra Arising from Combustion Processes, Combustion and Flames. Vol. 3, 1959, pp. 13-38.

29. Cook, G. R.; and Metzger, P. H.: Photoionization and Absorption Cross Sections of H_2 and D_2 in the Vacuum Ultraviolet Region. J. Op. Soc. Am., Vol. 54, 1964, pp. 968-972.

30. Williams, D. ed.: Methods of Experimental Physics. Vol. 3,Molecular Physics, Academic Press, N. Y., 1962.

31. Nakayama, T.; and Watanabe, K.: Absorption and Photoionization Coefficients of Acetylene, Propyne, and 1-Butyne. J. Chem. Phys., Vol. 40, 1964, pp. 558-559.

32. Brewer, L.; and Engelke, J. L.: Spectrum of C_3. J. Chem. Phys., Vol. 36, 1962, pp. 992-998.

33. Cooper, J. W.; and Martin, J. B.: Electron Photodetachment from Ions and Elastic Collision Cross Sections for O, C, Cl, and F. Phys. Rev., Vol. 129, May 1962, pp. 1482-1488.

34. Bethke, G. W.: II. Oxygen Schumann-Runge Bands, J. Chem. Phys., Vol. 31, 1959, pp. 669-673.

35. Jarmain, W. R.; and Nicholls, R. W.: A Theoretical Study of the $O_2X^3\Sigma_g - B^3\Sigma_u^-$ Photodissociation Continuum. Proc. Phys. Soc. Vol. 84, 1964, pp. 417-424.

36. Wilkinson, P. G.: Forbidden Band System in Nitrogen. I. The Vegard-Kaplan System in Absorption. J. Chem. Phys., Vol. 30, 1959, pp. 773-776.

37. Nicholls, R. W.: Franck-Condon Factors to High Vibrational Quantum Numbers. I: N_2 and N_2^+. J. Research NBS, 66A, 1961, pp. 451-460.

38. Watanabe, K.; and Marmo, F. F.: Photoionization and Total Cross Section of Gases. II. O_2 and N_2 in the Region 850-1500A. J. Chem. Phys., Vol. 25, 1956, pp. 965-971.

39. Nicholls, R. W.: Laboratory Astrophysics. J. Quant. Spectrosc. Radiat. Transfer, Vol. 2, 1962, pp. 433-449.

40. Ory, H. A.: Franck-Condon Factors and Electronic Oscillator Strengths for Nitric Oxide Ultraviolet Band Systems. J. Chem. Phys., Vol. 40, 1964, pp. 562-566.

41. Nicholls, R. W.: Franck-Condon Factors to High Vibrational Quantum Numbers, II: SiO, MgO, SrO, AlO, VO, NO. J. Research NBS, Vol. 66A, 1962, pp. 227-231.

42. Fairbairn, A. R.: Spectrum of Shock-Heated Gases Simulating the Venus Atmosphere. AIAA J., Vol. 2, 1964, pp. 1004-1007.

43. Nicholls, R. W.; Fraser, P. A.; and Jarmain, W. R.: Transition Probability Parameters of Molecular Spectra Arising from Combustion Processes. Combustion and Frame, Vol. 3, 1959, pp. 13-38.

44. Bennett, R. G.; and Dalby, F. W.: Experimental Oscillator Strength of the Violet System of CN. J. Chem. Phys., Vol. 36, 1962. pp. 399-400.

45. Childs, D. R.: Vibrational Wave Functions and Overlap Integrals of Various Band Systems. Research Report 147, AVCO-Everett Research Laboratory, Jan. 1963 (Also, with abridged data in J. Quant. Spectrosc. Radiat. Transfer, Vol. 4, 1964, pp. 283-290.)

NASA-Langley, 1970 — 33 CR-1462